THESIS

FABRICATION AND CHARACTERIZATION OF ELECTRICALLY PUMPED VCSEL BASED INTRACAVITY FLUIDIC BIOSENSOR

Submitted by

Tao Yu

Electrical and Computer Engineering

In partial fulfillment of the requirements

For the Degree of Master of Science

Colorado State University

Fort Collins, Colorado

Fall 2002

COLORADO STATE UNIVERSITY

Fall 2002

WE HEREBY RECOMMEND THAT THE THESIS PREPAIRED UNDER OUR SUPERVISION BY TAO YU ENTITLED FABRICATION AND CHARACTERIZATION OF ELECTRICALLY PUMPED VCSEL BASED INTRACAVITY FLUIDIC BIOSENSOR BE ACCEPTED AS FULFILLING IN PART REQUIREMEMTS FOR THE DEGREE OF MASTER OF SCIENCE.

Committee on Graduate Work

Advisor

Department Head

ABSTRACT OF THESIS

FABRICATION AND CHARACTERIZATION OF ELECTRICALLY PUMPED VCSEL BASED INTRACAVITY FLUIDIC BIOSENSOR

There is an increasing need to quickly and cheaply detect the presence of biological agents introduced into the atmosphere by terrorists or on the battlefield. In order to accomplish this requires a biosensor and a method of integrating it with electronics and an alarm or display. The overall device must be small, easily manufactured and simple to use in order that it be sufficiently portable to allow being carried in many different types of situations. This thesis reports the fabrication and characterization of such a sensor based on an electrically pumped vertical-cavity surface-emitting laser (VCSEL).

The prototype biosensor structure reported here is composed of a "half VCSEL" separated from a glass top plate coated with a dielectric distributed bragg reflector (DBR) mirror by a ~ 5 μm thick photoresist spacer. Simulations indicate that the emission wavelength for the sensor is shifted quasi-continuously with respect to the change of the cell refractive index and/or the fluidic cavity thickness.

Fabrication of the VCSEL biosensor required the development of suitable techniques for forming the fluidic cavity, a fluid delivery system, proper sealing and forming the

VCSEL. All of these were accomplished. The fluidic cavity, which provides suitable spacing and fluid seal, was formed by heating patterned photoresist at 90 °C with external force applied. The fluid was introduced into the VCSEL cavity from a capillary tube butted up against the side of the cavity. The tube/cavity connection was successfully sealed with a deposited epoxy gasket. Forming a suitable n-ohmic contact was the most difficult step in VCSEL fabrication because the n mirror is very thin.

The assembled structure was shown to emit light but apparently does not lase. The functionality of the biosensor was demonstrated by the presence of a 3.2 nm wavelength shift of the ~840 nm peak when DI water was injected into the empty fluidic cavity. The emission spectra are complex and the further study and analysis are required to interpret the measurements.

Tao Yu
Department of Electrical and Computer Engineering
Colorado State University
Fort Collins, CO 80523
Fall 2002

ACKNOWLEDGEMENTS

My thanks first go to my advisor Professor Carl Wilmsen. His knowledge in the area of optoelectronics and semiconductors has always been a good resource for me when problems come up during my research. Without his patience, understanding and leadership, I would not be able to successfully complete the research of my thesis. I express my sincere thanks to him for giving me the opportunity to work in his research group and motivating me throughout my research. I would also like to thank Dr. Kevin Lear and Dr. Stuart Field for serving on my committee.

I am very thankful to current members of the group, Tao Ao and Klaus Hartinger, for their supports and suggestions. Their ideas and comments are always helpful to me. A heartfelt thanks is also extended to the former members, Preetam Alluri, Chris Wacinski, Tae-ping Lee and Dr. Rui Pu, for providing working experience for my research.

I thank Kent Geib from Sandia National Laboratories for providing me an 850 nm half VCSEL wafer, Dr. Stewart Feld from Cielo Communications, Inc for fabricating the dielectric mirror and DARPA contract # MDA 9720010020 for providing RA and research support.

I am grateful to Dr. Dinesh Patel. His wise and experience help me lot in the cleanroom work. I enjoyed those complain and laugh with him when repairing the evaporator.

Also I would like to thank Hua Shao and Ahmad Nasser Al-Omari for their help in testing the biosensor.

Finally, I want to thank my wife Yun Xu. Her love motives me all the time. We've together overcome all the difficulties in the past two years.

Tao Yu
Department of Electrical and Computer Engineering
Colorado State University
Fort Collins, CO 80523
Fall 2002

TABLE OF CONTENTS

LIST OF FIGURES AND TABLES

Figures

Tables

CHAPTER 1

INTRODUCTION

1.1 Background

1.1.1 Biosensor Definition, Composition and Classification

In the past two decades, the biological and medical fields have seen great advances in the development of biosensors. Biosensors are used for such diverse applications as DNA matching, pharmaceutical process control, automatic sweetness monitoring, detection of bio-threats, glucose sensing and environmental monitoring. [1-5] As a result, the literature on biosensors has grown significantly. A good overview of the latest sensing techniques and advances is given in the proceeding of the Seventh World Congress on Biosensors, Kyoto, Japan, May 2002. [6]. Devices more related to the one presented in this thesis can be found in the proceeding of the SPIE conferences entitled "Micro-and Nanofabricated Structures and Devices for Biomedical Environmental Applications".[7] The paper written by P.L. Gourley *et al.* is particularly useful and will be reviewed in depth in Chapter 2. [8] Generally, the term biosensor has been used to define a compact analytical device which can detect biological systems or directly monitor a bioprocess and provide either qualitative or quantitative results about the analyte. [9] There are two general types of biosensors: those that utilize a biorecognition system (or bioreceptor) and those that do not. The first type of biosensor consists of two major parts as shown in

Figure 1.1. The first part is the biorecognition system, which typically includes antibodies, enzymes, nucleic acids, bacteria, single cell organisms or even whole tissues of higher organisms. The second part is a physicochemical transducer or transducing micro-system, which can be optical, electrochemical, thermometric, piezoelectric or magnetic.[10] Special biochemical interaction between the target analyte and the complementary biorecognition layer predeposited on the surface of the transducer produces a physicochemical change, which is detected and possibly measured by the transducer. Either discrete or continuous measurable signals will be generated to indicate characteristics of the target analyte. The working principle of bioreceptor type biosensors is described by Figure 1.1. [10]

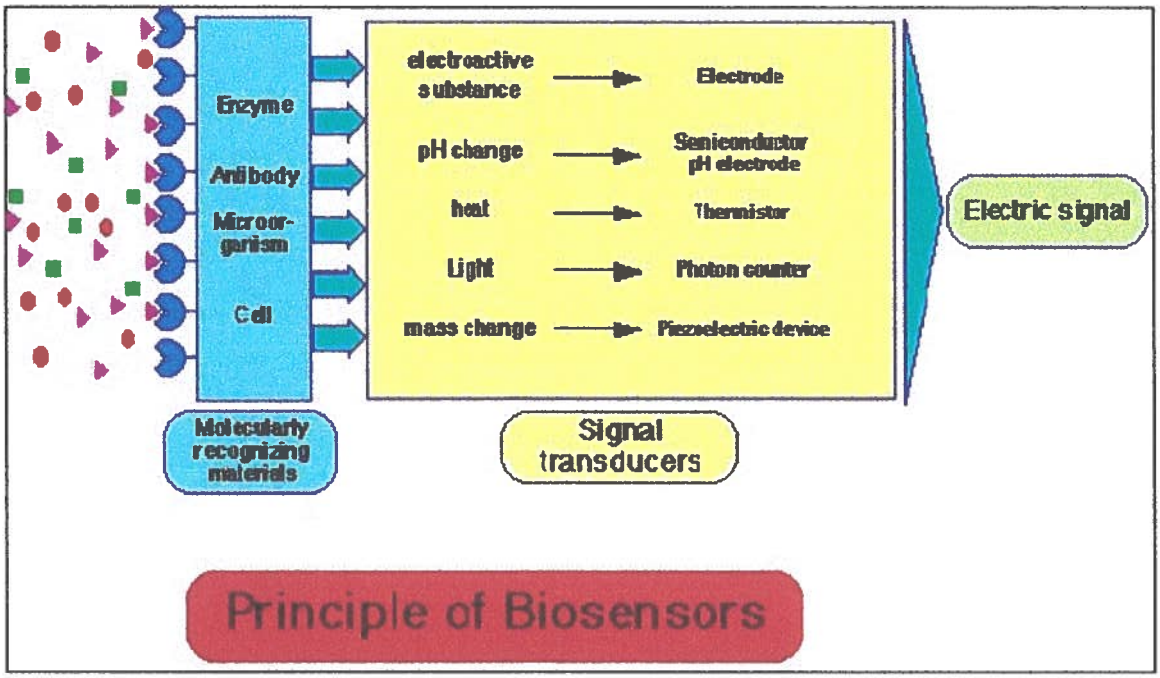

Biosensors are analytical devices which use biological interactions to provide either qualitative or quantitative results.

Figure 1.1 General composition and working principle of the bioreceptor type biosensors. (Copied from website http://userpages.umbc.edu/~jshull1/ench772/construction [10])

The second type of biosensor is simply manufactured and usually contains the bioselectivity in the transducer. A vertical-cavity surface-emitting laser (VCSEL) based intracavity fluidic biosensor is a typical representative of this type. Biosensors can be classified either by their bioreceptor or by their transducer type as shown in both Figure 1.1 and Table A.1 & A.2 of Appendix A. [10] Currently, photonic biosensors using an optical transducer, such as a fluorescence tag, waveguide, optical fiber or VCSEL, are used or are being investigated, because optical signals are easily generated and their corresponding spectra are sufficient for sensing the target. [8, 11-14, 25-27] These biosensors can be either active or passive devices. Waveguide or optical fiber based biosensors are passive devices, which often use an external laser as an excitation light source and deliver the light with waveguides or optical fibers. On the other hand, active devices, like electrically pumped VCSEL based biosensors, can form a laser resonant cavity together with the target analyte and generate light internally. The biosensor designed and fabricated at CSU belongs to the later.

1.1.2 Biosensor Applications

The current success and variety of biosensors are attributed to the extraordinary demands of increasingly broader application fields, including 1) clinical diagnosis and biomedicine, for example, blood glucose monitoring at home, 2) farm, garden and veterinary analysis, for example, pesticides usage control, 3) bioprocess monitor and control, like fermentation in situ monitoring, 4) food and drink production and analysis, like fish freshness assay, 5) research & development, for example, bacterial and viral analysis in microbiology, 6) pharmaceutical and drug analysis, namely drug screening, 7)

environmental monitoring, such as pollution control and monitoring. [2, 4-5, 15-18] In addition, there is an increasing need to quickly and cheaply detect the presence of biological agents introduced into the atmosphere by terrorists or on the battlefield, which greatly impels biosensors to be small, compact, easily manufactured and simple to use in order that it be sufficiently portable to allow being carried in many different types of situations.

1.1.3 Electrically Pumped VCSEL Based Biosensor Vs. Waveguide or Optical Fiber Based Biosensor

Since an optical transducer can be either an extrinsic or intrinsic optical method as shown in Table A.2 in Appendix A, photonic biosensors can have not only a wider range of device implementations but also different types of spectroscopies, including absorption, fluorescence, phosphorescence, Raman, SERS, refraction or dispersion spectrometry, etc. [19] Two implementations of optical biosensors are illustrated in this section. They are waveguide or optical fiber based biosensors (see Figure 1.2) and electrically pumped VCSEL based intracavity fluidic biosensors (see Figure 1.3). These two implementations represent almost all of the advantages of the optical transducing mechanism.

Waveguide or Optical Fiber Based Biosensors are passive devices since they basically collect light from an external excitation laser source and deliver the light via a waveguide or optical fiber by means of totally internal reflection. The key driving force in choosing this technology is their ability to be simply fabricated and highly selective if bioreceptors are used. This biosensor implementation can be subdivided into three categories according to their optical readout principles: Mach-Zehnder interferometry

(MZI), surface plasmon resonance, and luminescence quenching. [20] When an optical wave is confined in a dielectric guide, the field is not totally confined to the core layer of

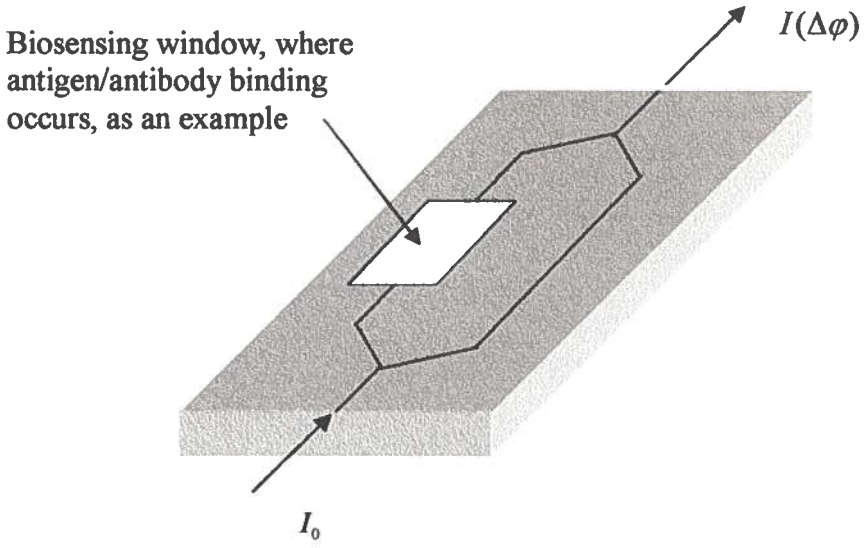

Figure 1.2 Schematic diagram of a Mach-Zehnder interferometer (or waveguide) based biosensor. [21]

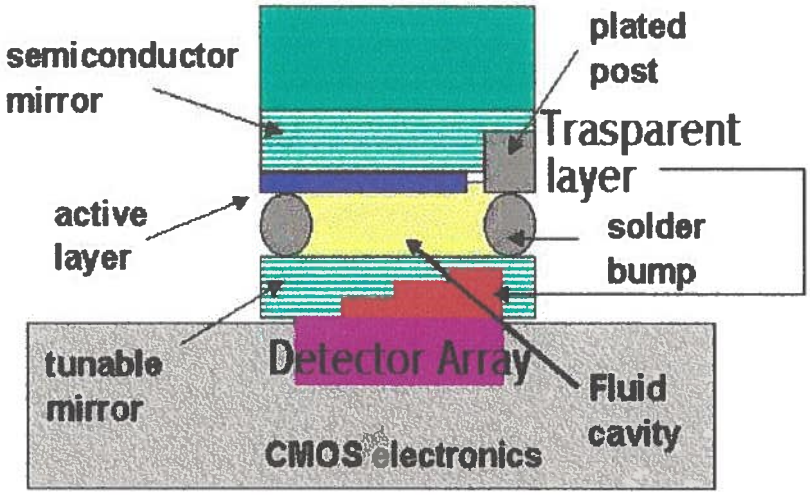

Figure 1.3 Schematic diagram of an electrically pumped VCSEL based intracavity fluidic biosensor.(Copied from reference [24])

the waveguide, but shows exponentially decaying tails in the surrounding materials via evanescent fields. Different kinds of biomaterials will partially replace the upper cladding layer of the waveguide or outer cladding layer of the optical fiber, form different boundary conditions imposed on the waveguide propagation mode, consequently, changing the effective refractive index of the dielectric guide through evanescent fields, resulting in a phase or intensity change of the guided wave. By this means, the measurement of concentration and refractive index of the biofluid sample on the top of the waveguide's core layer is possible. For example, Boiarski *et al.* reported an optical immunosensor using a Mach-Zehnder interferometer. [21] The antigen/antibody binding mechanism is used for the biochemical selection. In this sensor, a thin sensitive film containing an antibody is deposited onto the surface of MZI's sensing arm, which selectively binds antigens from the fluid sample. The interaction influences the effective refractive index of the sensitive window, which then results in an intensity change of the output light. The output light intensity $I(\Delta\varphi)$ as a function of the incident light I_0 is given by

$$\frac{I(\Delta\varphi)}{I_0} = \frac{1}{2}\left[1 + \cos\left(\frac{2\pi}{\lambda} L\Delta n_{eff}\right)\right] \approx \cos^2\left(\frac{\Delta\varphi}{2}\right) \qquad (1.1)$$

with $\Delta\varphi = (2\pi\ L/\lambda)\,\Delta n_{eff}$ where L is the length of the sensing coating and Δn_{eff} is the change in the effective refractive index of waveguides introduced by binding antigens onto the layer of antibodies. [22] An improved MZI biosensor was reported by Ch.Stamm *et al.* [23], where dual wavelength operation is used for biosensing in order to overcome the time-dependent refractive index and temperature variations of the sample with a signal differentiation method.

Electrically Pumped VCSEL Based Intracavity Fluidic Biosensors are classified as active devices because they can form a laser resonant cavity and convert electrical energy into light. This kind of biosensors offers more benefits compared to passive devices. They are:

1) *Much more compact size, microns, with a comparable dimension to living cells.* This biosensor implementation can integrate a laser source, detector, fluid delivery system as well as amplifier and logic circuitry in one chip. [19] "On chip" bioanalyte detection, analysis and control are possible. Passive biosensors usually depend on an external excitation laser source and other comparatively large optical components to create the required optical path. [19] Both types of systems require a method of wavelength shift detection which can be large. This part of the project is being developed by another participator in the DARPA BOSS university center.
2) *Very high operating frequencies,* because the light is generated in a stimulated emission process. [8]
3) *Simple construction and more accurate results.* In VCSEL based biosensors, a bioreceptor is not required. The bioanalyte occupies the resonant cavity of the VCSEL and aids or degrades the light generating process. Laser lights can amplify the subtle refractive, absorptive or diffractive effects in the analyte since the photons sample the analyte bouncing between opposing mirrors many times. The emission spectra provide information about the analyte. [8]
4) *Simple and efficient light collection process,* because the stimulated emission occurs in a narrow beam that can be directed toward a small area, high speed detector, [8] or

well coupled with an optical fiber. This makes a detector array integrated with an electronic circuitry in a tiny chip possible.

5) *High signal to noise ratio and enhanced signal sensitivity,* since the light signal is very intense, usually in the range of milliwatts. [8] The cell within the aperture of the VCSEL will absorb some of this light. [28] If the absorption is large, then VCSEL will probably turn off. It could also change the structure of the cell. At same point, biologist should investigate the effect of intense light on the structure of the cells.
6) *No chemical damage to cells*. Conventional passive biosensors use dye or tag method to make cell visible, which cause serious damage to living cells. The optical damage caused by the intense laser beam could occur in the VCSEL based biosensors.
7) *Sensor reusable capability.* Unlike passive devices, which usually use bioreceptors to select the analyte from the sample, resulting in an unreusable sensor due to the damage or contamination of the sensing layer, VCSEL based intracavity fluidic biosensors can flush and clean the fluidic cavity with DI water or nitrogen as long as the device surface layer is passive to bioanalytes.
8) *Compact data indications.* Emission spectrum is the only optical result wanted. From the spectrum, we can obtain information such as refractive index, structure, size, number and dynamic change of the bioanalyte, based on the wavelength shift, mode linewidth change, mode spacing change, mode intensity change and beam shape change. Such a study will be carried out by other students funded by this project.
9) *Compatible to bioreceptor type biosensors.* Sensitive layers containing bioreceptors can be deposited to further enhance device bioselectivity.

Therefore, an electrically pumped VCSEL based intracavity fluidic biosensor is so attractive that it is investigated in our project.

1.2 Overview of This Project

The purpose of our project is to provide a first generation electrically pumped VCSEL based intracavity fluidic biosensor used for biological or chemical sample analysis by introducing an analytic biofluid into the high finesse cavity of the VCSEL. The basic device geometry in our proposal is illustrated in Figure 1.3. [24] As Dr. Lear and Dr. Wilmsen wrote in their proposal, "The optical properties of the fluids as modified by the biological cells they contain are sensed by monitoring the output optical intensity and wavelength of the laser. A monolithic VCSEL base consisting of the lower mirror and active region are grown on the primary substrate, for example, GaAs. The optical beam generated in this section passes through the fluidic cavity and is reflected by an external mirror placed tens of microns from the surface of the active region. The fluidic cavity can be formed by either flip chip bonding the VCSEL onto the external mirror chip using the flip chip process previously developed at Colorado State University or placed on a gasket material such as polyimide or photoresist. Since the cells are approximately the same lateral dimensions as the optical aperture of the laser, the index of refraction of the cells modify the wavelength of the laser. Given that VCSEL output have a linwidth of ~100MHz, resolvable wavelength shifting can occur with index changes as small as 10^{-6}. Absolute references for such small shifts will be difficult to implement, but differential signal detection using laser heterodyning may be possible. The cells also introduce loss into the cavity. And since the output power of the VCSEL is highly sensitive to the loss,

the VCSEL can detect low concentration of cells in the fluid. Also, cell specificity may be obtained by coating different VCSELs in an array with specialized receptors." [24]

Chapter 2 reviews a biosensor structure presented by P.L.Gourley *et al.* from Sandia National Laboratories, which provides a starting point for our biosensor design. So a detailed description of the Gourley biosensor is discussed in this chapter, including the biosensor structure, its working principle and experimental results.

Chapter 3 describes the design details and simulation results of an electrically pumped VCSEL based intracavity fluidic biosensor. Since it is the first time for us to design a biosensor, general considerations of design are first presented. Several issues expected from a real device fabrication are investigated, including those in a laser source, a dielectric mirror, fluid transportation and sealing methods, etc. Then, the prototype structure of our first generation biosensor is given. Finally, simulation results show how sensitive our biosensor responds to bioagents in the fluid sample.

Chapter 4 discusses the detailed fabrication steps of an electrically pumped VCSEL based intracavity fluidic biosensor. Great efforts have been made to solve the problems arising from the practical device fabrication in order to achieve a high performance biosensor. New fabrication technologies such as edge extension, "magnetic bonding" and epoxy reservoir tubes are developed. Top view of the biosensor system without the drain reservoir and the corresponding fluidic interconnections is shown in Figure 4.9.

Chapter 5 presents the measurement results for our biosensor. The VCSEL has produced a strong emission. The emission spectra are used to extract useful information of the bioanalyte in the fluid sample.

Conclusions and suggestions for the future work are given in Chapter 6. Some adjustments and improvements on design and process concluded from current work experience are proposed here, which will be applied to our second generation electrically pumped VCSEL based intracavity fluidic biosensor. The details of the biosensor classification, half VCSEL data sheets, the proton implantation simulation and the fabrication recipes are described in Appendix A, B, C and D, respectively.

1.3 Summary of Chapter 1

In this chapter, general definition and constitution of biosensors are given at the beginning. According to their bioreceptor, transducer type and light generation capability, biosensors are classified into different subcategories as shown in Figure 1.1 and Table A.1 & A.2 of Appendix A. An overview of biosensor applications is given in the following part of this chapter and the example corresponding to each filed is also given. In the latter half of the chapter, a comparison of an electrically pumped VCSEL based intracavity fluidic biosensor to waveguide or optical fiber based biosensor is elaborated and the advantages of the former are evident. Finally, the proposal of this project is quoted to specify the objectives and the results expected to this research. In a word, an electrically pumped VCSEL based intracavity fluidic biosensor is so attractive and it is investigated in this thesis research.

References:

[1]. Meng Wu, *et al.*, "Detection of DNA hybridization with surface plasmon resonance biosensor: comparison of immobilization of oligonucleotides by ssDNA and dsDNA", *Proc. SPIE* 4414, pp.23-26 (2001).

[2]. Yanli Zhang, *et al.*, "Salt-bridge-supported bilayer lipid membrane biosensor for determination of anticancer drug cyclophosphamide", *Proc. SPIE* 4414, pp.145-148 (2001).

[3]. Jie Hu, *et al.*, "New taste sensor system combined with chaotic recognition", *Proc. SPIE* 4414, pp.406-463 (2001).

[4]. Maurice V. Cattaneo and J.H. Luong, "Novel FIA chemiluminescence fiber optic biosensor for urinary and blood glucose", *Proc. SPIE* 1886, pp.186-192 (1993).

[5]. M. Trojanowicz and P.W. Alexander, "Biosensors for direct monitoring of environmental pollutants in field", *Kluwer Academic Press,* pp.173-184, (1998).

[6]. *Proceeding of the Seventh World Congress on Biosensors*, Kyoto, Japan, May 2002. (*www.biosnesors2002.com*)

[7]. "Micro-and Nanofabricated Structures and Devices for Biomedical Environmental Applications", *Proc. SPIE* 3258 (1998), 3606(1999), and 3912(2000).

[8]. P.L. Gourley and A. E. McDonald, "Semiconductor microlasers with intracavity microfluidics for biomedical application", *Proc. SPIE* 2978, pp.186-196 (1997).

[9]. "Introduction", *http://userpages.umbc.edu/~jshull1/ench772/intro*.

[10]."Biosensor construction", *http://userpages.umbc.edu/~jshull1/ench772/construction*.

[11]. James O. Spiker, and Kyung A. Kang, "Preliminary study of real-time fiber optic based protein C biosensor", *Biotechnology and Bioengineering* 66(3), pp.158-163 (1999).

[12]. Daniel P. Campbell, *et al.*, "Optical system-on-a-chip for chemical and biochemical sensing: the chemistry", *SPIE* 3540, pp.153-161 (1999).

[13]. Nile F. Hartman, *et al.*, "Optical system-on-a-chip for chemical and biochemical sensing: the platform", *SPIE* 3537, pp.302-309 (1999).

[14]. Daniel P. Campbell, *et al.*, "Integrated optic sensor for pH and ammonia", *SPIE* 3537, pp.327-335 (1999).

[15]. Ursula Bilitewski, *et al.*, "Biosensor systems for pesticide determination in water", *Proc. SPIE* 1716, pp.176-185 (1993).

[16]. M.-A. Carsol and M. Mascini, "Development of a system with enzyme reactors for the determination of fish freshness", *Talanta*, 47, pp.335-342 (1998).

[17]. Petr Slakdal, M. Mascini, Claudio Salvadori and Gianfranco Zannoni, "Detection of Bacterial contamination in sterile UHT milk using an L-lactate biosensor", *Enzyme and Microbial Technol.* 15, pp.508-512 (1993).

[18]. Kim R. Rogers and Clare L. Gerlach, "Environmental biosensors: a status report", *Environmental Science & Technology* (1996).

[19]. Tuan Vo-Dinh and Brian Cullum, "Biosensors and biochips: advances in biological and medical diagnostics", *Fresenius J Anal Chem* 366, pp.540-551 (2000).

[20]. P. Rai-Choudhury, "MEMS and MOEMS technology and applications", *SPIE Press* (2000).

[21]. A. A. Boiarski, J. R. Bush, B.S. Bhullar, R. W. Ridgway, and V. E. Wood, *Proc. SPIE* 1793, p.199 (1992).

[22]. N. Fabricius, G. Gauglitz and J. Ingenhoff, *Sensor Actuators* B 7, p.672 (1992).

[23]. Ch. Stamm, R, Dangel, and W. Lukosz, "Biosensing with the integrated-optical difference interferometer: dual-wavelength operation", *Optics Communications*, pp.347-359 (1998).

[24]. Tao Yu, Kevin Lear and Carl W Wilmsen, "Biological cell sensing with a fluidic cavity vertical cavity surface emitting laser", *CAB Day at Fitzsimons Poster Session* (2000).

[25]. P.L. Gourley, T.French, A. E. McDonald, E.A. Shields, and M. F. Gourley, "Ultrasensitive detection of red blood cell lysing in a microfabricated semiconductor laser cavity", *Proc. SPIE* 2978, pp.195-206 (1998).

[26]. P. L. Gourley, *et al.*, "Detecting cancer quickly and accurately", *Proc. SPIE* 3912, pp.2-10 (2000).

[27]. P. L. Gourley, *et al.*, "Semiconductor microcavity laser spectroscopy of intracellular protein in human cancer cells", *Proc. SPIE* 4265, pp.113-124 (2001).

[28]. "Optical properties spectra", *http://omlc.ogi.edu/spectra/index.html*

CHAPTER 2

LITERATURE REVIEW AND THEORETICAL BACKGROUND

2.1 VCSEL Based Biosensor from Sandia National Laboratories

In the year 1997, P. L. Gourley *et al.* from Sandia National Laboratories published a paper on a VCSEL based biosensor. [1] Their biosensor has a simple structure without bioreceptor, which is illustrated in Figure 2.1. Optically pumping is used to excite lasing and emission spectra are utilized to extract information of the bioanalyte in the fluid sample. This biosensor is comprised of a half VCSEL chip containing only a bottom semiconductor mirror and a multiple-quantum-well (MQW) active region grown on a GaAs substrate, a fluidic cavity with a dimension about the size of the biological cell, usually a few microns, and a highly reflective dielectric mirror deposited on the top glass substrate. The basic idea of this design is that the cell, as a component of a laser resonant cavity, aids the light-generation process and the dielectric properties of various cell components and their surrounding fluids will modify the effective optical pathlength, consequently, changing the output wavelength, power and even transverse modes of the VCSEL. Therefore, the presence of a cell and its characteristics can be detected. The spacing and intensity distributions of the spectral peaks of the VCSEL output yield a unique spectra signature for each type of the cell that cannot be confused with other cells

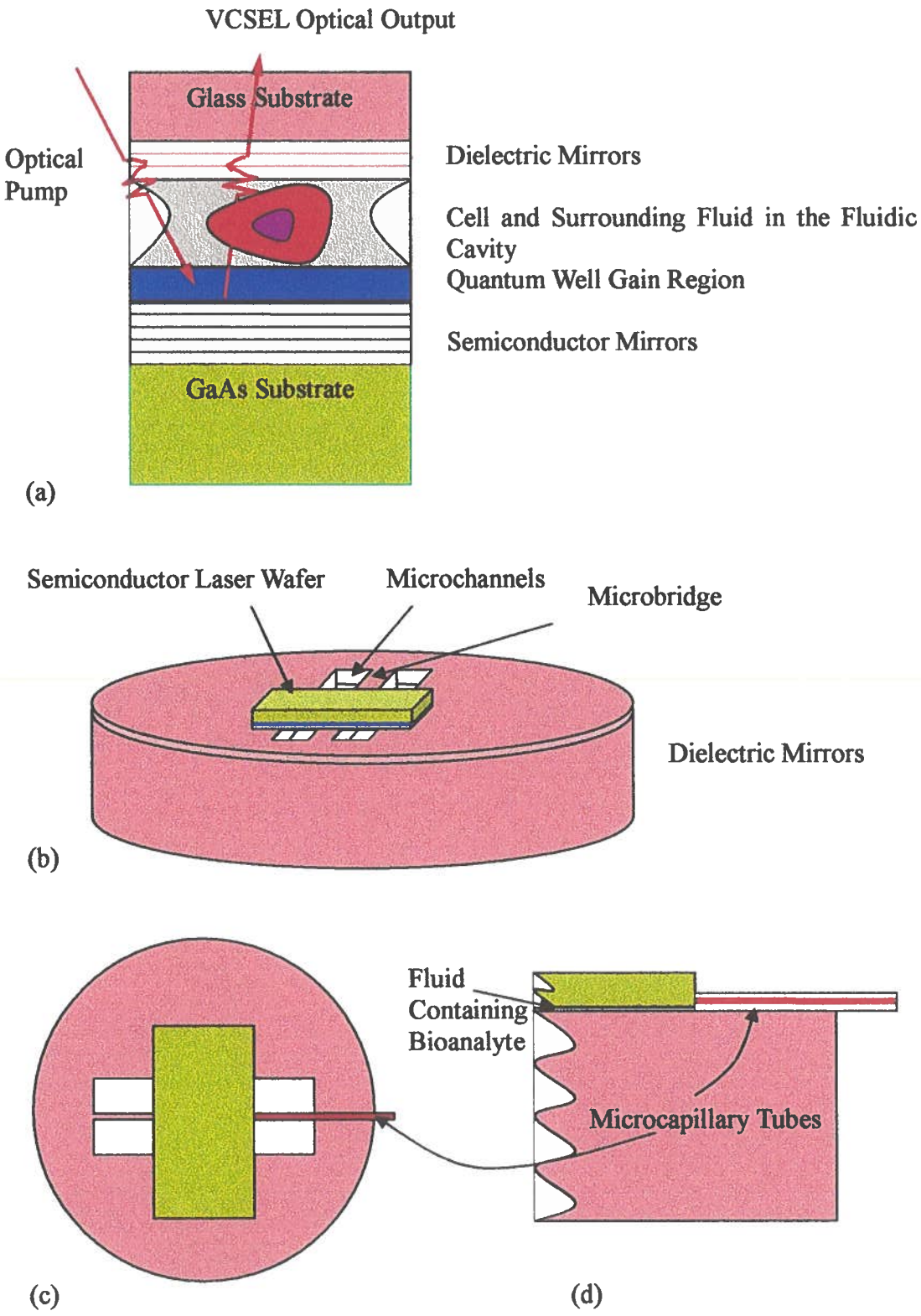

Figure 2.1 Schematic diagram of a P. L. Gourley's VCSEL based biosensor (a) crossing section view, (b) perspective view, (c) top view and (d) side view. (Copied from reference [1])

(at least for the cells tested) illustrated in Figure 2.2.[1, 2]

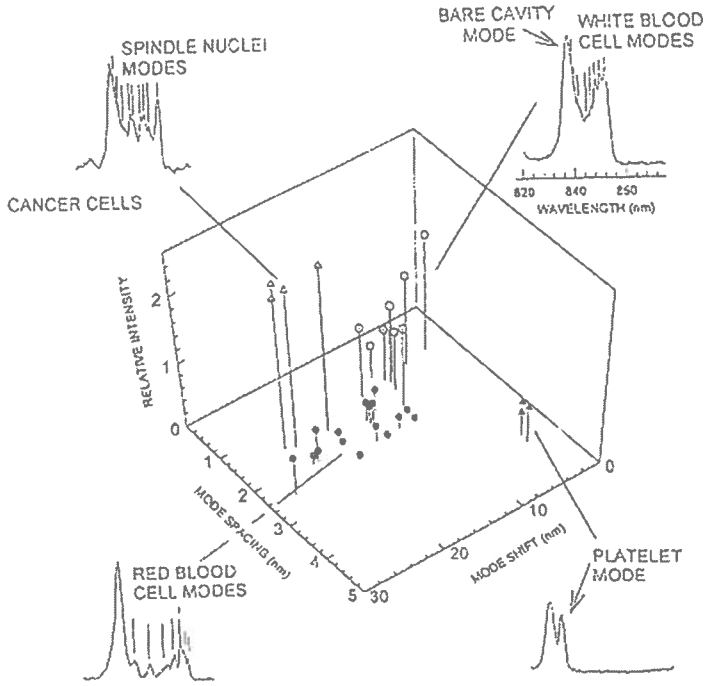

Figure 2.2 Representative spectra for 4 different cell types and cluster plot for identifying cell types. (Copied from reference [1])

2.2 Physics of P.L. Gourley's VCSEL

2.2.1 Longitudinal Optical Modes in the VCSEL Microcavity

The VCSEL of Gourley *et al.* is formed by bonding a semiconductor and a dielectric mirror together separated by a fluidic cavity. Their analysis of the longitudinal mode wavelengths emitted from the VCSEL microcavity (shown in Figure 2.1(a), typically comprised of a fluid cavity and a semiconductor gain region) in the biosensor is as follows:

The emitted wavelength determined by total roundtrip optical pathlength in the cavity $\xi = 2\sum_i l_i n_i$ is given by

$$\lambda_l = \frac{\xi}{l - \phi/2\pi}, \tag{2.1}$$

where l is the longitudinal mode index, ϕ is the sum of the mirror phases, $l_1 n_1$ and $l_2 n_2$ are referred to the products of the thickness and refractive index of the fluid region and semiconductor gain region, respectively. The longitudinal mode separations are given by

$$\frac{\Delta\lambda_l}{\lambda_l} = -\frac{\lambda_l}{\xi}(1 + \lambda_l \xi' / \xi + \lambda_l^2 \phi' / 2\pi\xi), \tag{2.2}$$

The primes denote derivatives with respect to wavelength.[2] From Eq (2.1), the longitudinal mode wavelength shift for the biosensor can be derived to a linear function

$$\left(\frac{1}{\lambda_l}\right)\left(\frac{d\lambda_l}{dn_1}\right) = \frac{l_1}{l_1 n_1 + l_2 n_2} \quad . \tag{2.3}$$

As an example, when an effective optical pathlength of the fluid region is $l_1 n_1 = (3\mu m)(1.33) = 4$ μm and that of the semiconductor region is $l_2 n_2 = (0.4\mu m)(3.5) = 1.4$ μm, the smallest detectable change in wavelength is about 0.01 nm corresponding to an index change of about 10^{-5}.[1] The working principle of the VCSEL based biosensor originally comes from this idea, since different cells show different index values, leading to a different shift in resonant wavelength. For a fluid of index n_1 without a cell inside, Eq (2.1) can be rewritten as a "bare-fluid" (i.e., a uniform index fluid) mode wavelength of

$$\lambda_l = 2L^* n_1 / l, \tag{2.4}$$

where $L^* = l_1 + l_2(n_2 / n_1)$ is a nominal effective length of the microcavity with respect to a normalized index value of n_1.[2] In addition, the longitudinal mode linewidth can be approximated by

$$\Delta\lambda_l = -\frac{\lambda_l^{\,2}\gamma}{2\pi c}, \tag{2.5}$$

where

$$\gamma = \gamma_m + \gamma_s + \gamma_d + \gamma_f \tag{2.6}$$

and the terms on the right denote mirror leakage and scattering, semiconductor absorption, cavity diffraction, and fluid absorption and scattering, respectively. For details, refer to [5]. The linewidth is also affected by the resolution of the measuring instruments. Typical value is a few nanometers.[1] Among all longitudinal mode characteristics mentioned above, wavelength shifting is the basis for the bioagent detection.

2.2.2 Transverse Optical Modes in the VCSEL Microcavity

As discussed in reference [2], a cell inside the microcavity has the same waveguiding effect as an optical fiber due to the slight difference in the dielectric constant between various cell components and the surrounding fluids. For a first order approximation, the cell in the cavity can be modeled by a disk of index n_2 surrounded by a fluid of index n_1. As a result, the cell will perturb each bare-fluid mode of Eq (2.1) (or Eq (2.4)) by adding a series of modes at longer wavelengths λ_{lmn} where the indices l, m and n correspond to the axial, redial, and azimuthal solutions to the wave equation for light confined by the cell in the cavity. In theory, the fundamental transverse mode has the greatest wavelength shift from the bare-fluid mode λ_l and is approximately given by

$$\Delta\lambda_{l00} = \Delta\lambda_l - \lambda_l^3 X_{00}^2 / 2\pi^2 n_2^2 d^2, \tag{2.7}$$

where d is the cell diameter. In detail, the first term arises from the dielectric shift $\Delta\lambda_l = \Delta\xi/(l - \phi/2\pi)$, where $\Delta\xi = 2\sum_i l_i \Delta n_i$, due to the change in refractive index from a low index value fluid (for example, blood plasma in the blood sample, i.e., $n_1 = 1.3420$ at 850 nm) to a cell with a high index value (for example, a normal red blood cell, i.e., $n_2 = 1.4076$ at 850 nm). The second term comes from the lateral waveguiding effect because of the presence of the cell, and its calculated value for red blood cells is 1.8 nm. [2] Experimentally, it is observed that $\Delta\lambda_{l00} \approx 20$ nm shifting for red blood cells, so the primary cause of the wavelength shift is the refractive index change.[2] Considering all solutions for transverse modes, the free space spectral wavelengths are expressed by

$$\lambda_{lmn} = \frac{2\pi n_1}{[(X_{mn}/d)^2 + (l\pi/L^*)^2]^{1/2}}, \tag{2.8}$$

where X_{mn} is the nth root of the characteristic equations. At the limit condition of $l\pi/L^* >> X_{mn}/d$, i.e., a bare-fluid limit, Eq (2.8) can be simplified to Eq (2.4).[2]

2.3 Fluid Delivery Method Used in the Gourley Biosensor

Since the microcavity is just a few microns long in the direction of the light output, the method to deliver the fluid into this tiny cavity should be carefully considered. Many factors such as surface conditions of the device, dimensions of the channel and etching and bonding techniques will greatly influence the fluid transportation velocity. In the Gourley biosensor, a wicking bridge using microcapillary feeding is created as illustrated

in Figure 2.1(b)(c). As described in reference [1]: "Two large channels are micromachined into the glass surface which is usually a multilayer dielectric mirror on a glass substrate. The channels are large, 500 microns and are separated by a few hundred microns to form a bridge structure. The semiconductor wafer is placed over the bridge and bonded, covering the width of the both channels but leaving the ends of the both channels exposed. The portion of the bridge in contact with the wafer forms an intracavity space that can be fed by microcapillary action. The action occurs when a microdrop of fluid is placed onto the exposed bridge next to the wafer. The microdrop can be applied with a fused silica microcapillary tube abutting the wafer edge on the bridged as shown in Figure 2.1(c) and Figure 2.1(d). The fluid can be delivered through a syringe or micropump off the chip (not shown in Figure 2.1)." The microchannels in this design could enhance the capability of the fluid delivery as long as the surface of the channels is sufficiently smooth. Actually, roughness may occur after chemical etching, which will have a negative effect on the fluid velocity. In our original design, the etched reservoir performs the same function as the microchannels. However, experiments showed that the reservoir was not required.

2.4 Preliminary Studies of the Gourley Biosensor

As a preliminary study, an infrared laser dye in ethylene glycol (n=1.425) was fed into the fluidic cavity (initially, air is inside and n=1), where n is the refractive index. The emission spectra of this experiment are presented in Figure 2.3. The peak positions in the bottom dye spectrum are shifted with respect to the air spectrum due to the cavity resonant condition change when the cavity is filled with fluid. The peaks occur at

different wavelengths with a much smaller spacing.[1] To further prove the capability of this sensor to detect dynamic cavity change, an experiment of natural water evaporation from the fluidic cavity was performed. As illustrated in Figure 2.4, the wavelength is shifted from 855 nm to 848 nm, when the cavity changes from wet to dry condition. The whole process lasts 12 minutes, according to the data provided by the reference [1].

2.5 Red Blood Cell Lysing Detection with the Gourley Biosensor

In 1998, P. L. Gourley *et al.* published a new paper about red blood cell detection using their biosensor. In this paper, a blood sample is wicked into the microcavity following by DI water injection. Typical dynamical emission spectra from the microcavity are given in Figure 2.5.[2] Before cell lysing, the spectrum is static (shown in Figure 2.5 at t=0 sec) and indicates a peak arising from the bare-fluid (blood plasma) mode and series of cell modes at longer wavelength, which is also shown in Figure 2.6.[2] Three cell features related to the cell composition, size and shape can be concluded based on this static spectrum, described in reference [2]. First, the wavelength shift of the longest wavelength mode from the bare fluid mode represents the index difference between the cell (hemoglobin as the major component) and the bare fluid (principally blood plasma). (In here, the wavelength shift caused by transverse modes is neglected, which is elaborated at the end of the section 2.2.2.) This difference increases with hemoglobin concentration. From the literature [2], a normal red blood cell has a biconcave disk shape which is about 7 μm in diameter and 2 μm in thickness. The protein hemoglobin is the major component of a normal hydrated cell with a concentration in the range 32 to 36 g/dL, while the level decreases in the body of an anemic patient. The second feature of the cell is determined

by the relative spacing of the modes, i.e., large mode spacings corresponding to a small cell diameter. Finally, the envelope of modal intensities is representative of the cell shape. As said in reference [2], cells with high biconcavity have spectra with significant intensity in the first and higher overtones, while spherical cells have spectra with a dominant fundamental modal intensity.

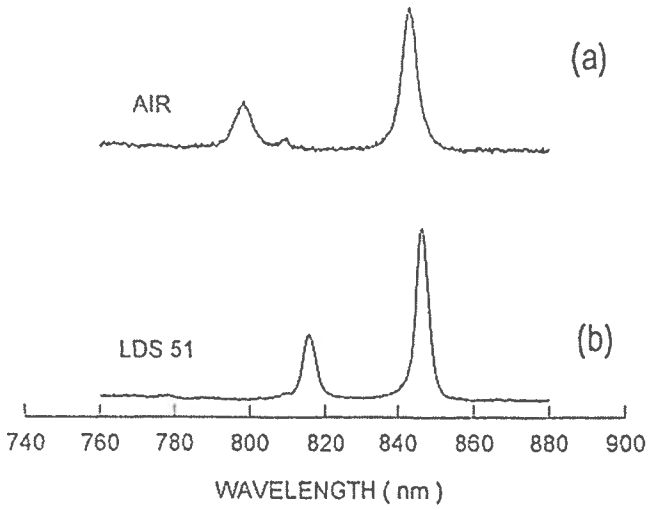

Figure 2.3 Typical emission spectra from P.L. Gourley's biosensor filled with (a) air, and (b) laser dye LDS751 in ethylene glycol. (Copied from reference [1])

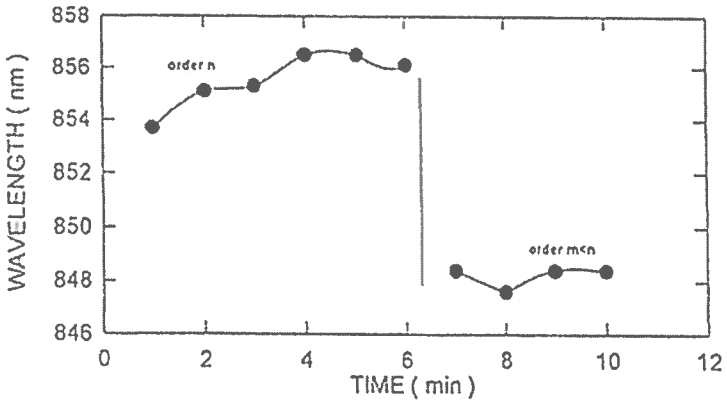

Figure 2.4 Dynamics of cavity modes showing the time change of a longitudinal mode during natural evaporation of water. (Copied from reference [1])

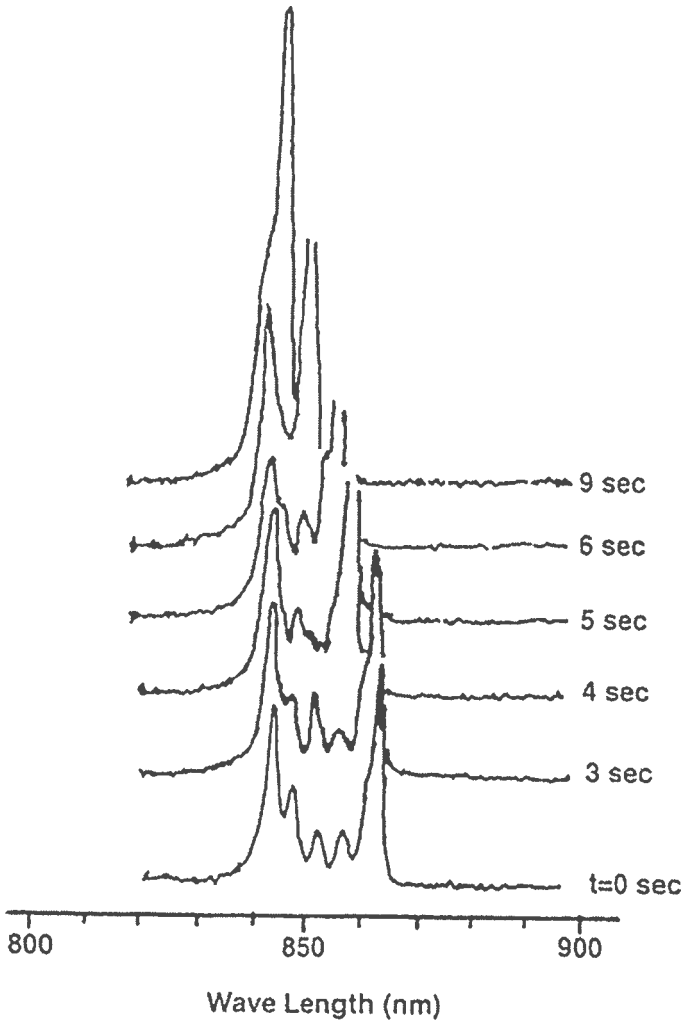

Figure 2.5 Dynamic emission spectra of the microcavity with a red blood cell in the microbridge after injection of water. The time after injection is indicated to the right of each spectrum. (Copied from reference [2])

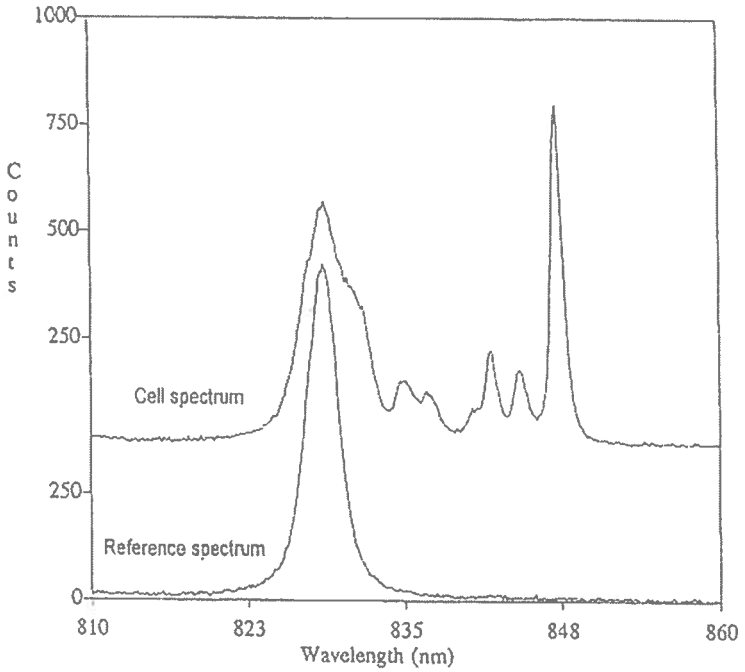

Figure 2.6 Static spectrum of the microcavity emission containing only blood plasma (low trace) and a red blood cell in plasma (upper trace) at room temperature. The dominant peak at 848 nm is shifted 19.3 nm from the bare fluid mode at 829 nm. This shift is linearly proportional to the hemoglobin concentration in the cell. (Copied from reference [2]

2.6 Summary of Chapter 2

In this chapter, several technical papers written by P.L.Gourley *et al.* from Sandia National Laboratories are reviewed, providing the concept and general working principle for the VCSEL based biosensor and setting the starting-point for developing our biosensor system. For more information about the Gourley biosensor, please read references [1-4]. More details about our VCSEL based intracavity fluidic biosensor will be presented in the following several chapters. Compared to the Gourley biosensor, our biosensor utilizes an electrically pumping technology with an advantage of a compact size which offers sufficiently portable to allow it being carried in many different kinds of situations.

References:

[1]. P.L. Gourley and A. E. McDonald, "Semiconductor microlasers with intracavity microfluidics for biomedical application", *Proc. SPIE* 2978, pp.186-196 (1997).

[2] P.L. Gourley, T.French, A. E. McDonald, E.A. Shields, and M. F. Gourley, "Ultrasensitive detection of red blood cell lysing in a microfabricated semiconductor laser cavity", *Proc. SPIE* 2978, pp.195-206 (1998).

[3]. P. L. Gourley, *et al*., "Detecting cancer quickly and accurately", *Proc. SPIE* 3912, pp.2-10 (2000).

[4]. P. L. Gourley, *et al*., "Semiconductor microcavity laser spectroscopy of intracellular protein in human cancer cells", *Proc. SPIE* 4265, pp.113-124 (2001).

[5]. *http://www.stanford.edu/class/ee231/Lecture14-InhomogBroadening.pdf*

CHAPTER 3

DESIGN AND SIMULATIONS OF ELECTRICALLY PUMPED VCSEL BASED INTRACAVITY FLUIDIC BIOSENSOR

3.1 General Considerations of Design

3.1.1 Overview of Design

Our electrically pumped VCSEL based intracavity fluidic biosensor allows the biological fluid to flow into the VCSEL fluidic cavity with a dimension about the size of the biological cell, where the cell detection is executed. The design of such a device requires considerations of the:

Optics--------	Laser cavity length, mirror reflectance, material and the longitudinal & transverse modes.
Fluidics------	Flow of water from an external reservoir to and through the fluidic cavity.
Spacers-------	Control & uniformity of the thickness, adhesion, leak tight sealing and fine scale patterning.
Electrical-----	Current confinement in the VCSEL, ohmic contacts and wire contacts to the device.

The choice of materials and type of processing used in the biosensor is further constrained by 1) the temperature required by the contact anneals and 2) the order in which the parts are assembled. All of the above issues are discussed in the following sections.

The biosensor presented in this chapter has similarities to the biosensor from Sandia National Laboratories described in the last chapter. The notable differences between the two structures are given in Table 3.1. The changes introduced into the CSU design improve the overall device, e.g. an external laser is no longer required and the unetched fluid channel enhances the water flow. In addition using an electrically pumped VCSEL greatly simplifies the optics of the biosensor by eliminating the external laser, the two beam splitters, the two mirrors and at least one of the lenses. [1] On the other hand, the basic concept of detecting biological cells by flowing water containing the cells through the fluidic cavity of a VCSEL and modifying the output spectrum remain the same.

Table 3.1 The notable differences between two biosensor structures

Structure	CSU Design	Sandia Design
VCSEL	Electrically pumped	Optically pumped
Spacer	~5 μm thick photoresist spacers	Didn't mention spacers only the presence of microchannels
Fluid sealant	Photoresist spacers and epoxy which do not affect the flow	Fusion or gluing which affects the flow
Mirror	5 mirror pairs on the top of the active layer	No mirror pairs on the top of the active layer
Reservoir/ Microchannels	None	Etched into the dielectric mirror/glass plate

3.1.2 The VCSEL

Normally, a VCSEL wafer consists of a quantum well active region with highly reflective semiconductor DBR (distributed bragg reflector) mirrors on each side with all layers grown on a semiconductor substrate by MBE or MOVPE. In some cases, deposited

dielectric layers are used as the top DBR. Thus, the optical cavity is contained within the semiconductor. Our VCSEL based intracavity fluidic biosensor requires a ~5 μm long fluidic cavity to allow the flow of the biofluid. That means the normal technologies such as MBE or MOVPE are impractical to fabricate the entire VCSEL stack. Although micromachined sacrificial layer is promising, it greatly increases the process complexity. Therefore, the biosensor structure and the corresponding growth methods should be carefully considered. For a first generation of our biosensor, a simple construction which has a half VCSEL and a dielectric mirror made separately and then bonded together with a ~5 μm thick spacer to form a fluidic cavity is used. The combination of a fluidic cavity and a semiconductor optical cavity allows for two possible cavity configurations. The first one is a fluid-coupled cavity (FCC) design, where the fluidic cavity is adjacent to the laser active region used in the Gourley biosensor as shown in Figure 2.1(a). Directly modulating the laser microcavity is possible with this strategy, resulting in a linear wavelength shift with the change in cell index, as represented by Eq (2.3). However, the optical loss is expected to be large since all of the light must pass through the biofluid. The absorption coefficient of hemoglobin, which is the major component of the red blood cell, is ~ 4 cm^{-1} for the wavelength around 850 nm. [16] Therefore, the threshold for lasing should be high in a FCC design. The second configuration is called a semiconductor-coupled cavity (SCC) design, where the fluidic cavity is a part of the top mirrors which are comprised of a low reflective (for example, 60%) semiconductor DBR mirror, a highly reflective (for example, 99.5%) dielectric mirror and a fluidic cavity between them as illustrated in Figure 3.11. The advantage of this approach is a lower optical loss compared to the SCC device since 60% light in the example is reflected back

by the semiconductor mirror, which should result in a lower threshold current and improve the VCSEL performance. The disadvantage of this approach is that wavelength does not shift linearly with index change but changes approximately periodically with index. This could increase the difficulty of sensing. The detailed equation to illustrate this is given in Section 3.3. Our biosensor utilizes the SCC structure. Kent Geib of Sandia National Laboratories provided us an 850 nm half VCSEL wafer (number: EMC5978), which has the following structural features [2]:

Bottom mirror: p-type, 36 pairs, >99.9% intensity reflectivity at 850 nm

Top mirror: n-type, 5 pairs, <60% intensity reflectivity at 850 nm

Quantum wells: undoped AlGaAs/GaAs, 5 wells, lasing at 850 nm

The EMC5978 MOVPE growth data sheet is given in Table B.1 of Appendix B and the calculated band diagram at equilibrium condition and semiconductor DBR mirror properties are shown in Figure 3.1 and 3.2, respectively.

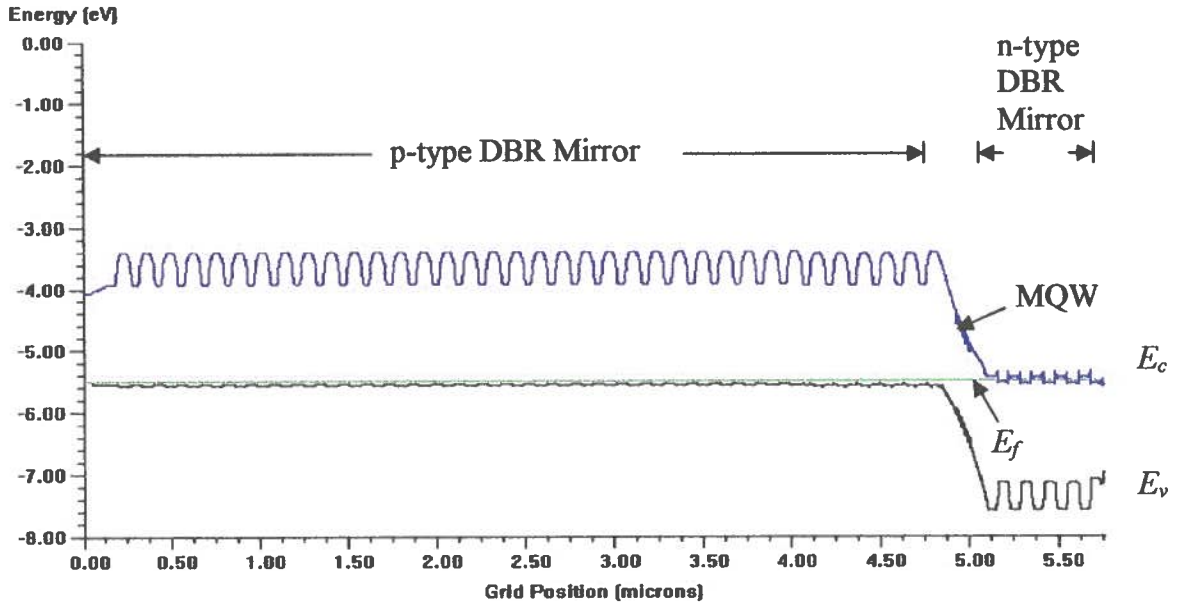

Figure 3.1 Band diagram for half VCSEL EMC5978 at equilibrium condition simulated by Simwindows. The vacuum energy level acts as an energy reference.

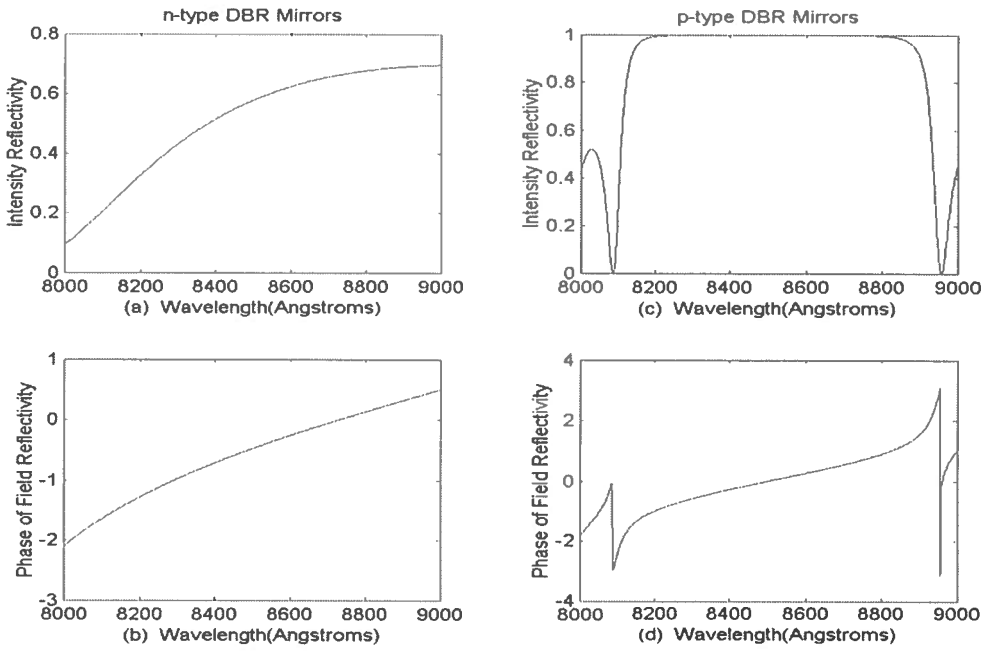

Figure 3.2 Semiconductor DBR mirror properties of the half VCSEL EMC5978: (a) intensity reflectivity ($R < 60\%$), and (b) phase for n-type DBR mirrors ($\phi \approx 30°$) at 850 nm, (c) intensity reflectivity ($R > 99.9\%$) and (d) phase for p-type DBR mirrors ($\phi = 0°$) at 850 nm, simulated by Matlab.

3.1.3 Biosensor Issues

3.1.3.1 VCSEL Current Confinement

One critical issue for an electrically pumped VCSEL design is the current confinement, which defines the current lateral extent without introducing unwanted losses. Four general structures, i.e., etched mesa, ion implanted, selectively oxidized and buried heterostructure VCSELs, are illustrated in Figure 3.3. [3] Combining two or more of these general structures has also been used. Among all these possible structures, the ion implanted current confinement is a promising candidate for the biosensor since it produces a planar surface, which is compatible with the fluidic cavity and is easy to

electrically contact. Commercial ion implanted infrared VCSELs have exhibited submilliamp threshold currents, high efficiency and up to 15GHz modulation bandwidth. [3] Most important of all, implanted VCSELs have shown reliability characteristics that are superior to any other semiconductor laser technology. [3] Therefore, proton implantation is used for the current confinement in our biosensor. Implantation of protons into the top semiconductor DBR mirror renders the material around the laser cavity nonconductive and thus concentrating the injected current into the center of the active medium as depicted in Figure 3.3 (b). Damage, primarily crystal vacancies created by the implanted ions, traps the free carriers leading to regions of high resistivity. The peak implant damage is usually designed to occur somewhat above the quantum wells to avoid the creation of non-radiative recombination center in the active region, which causes a large decrease in VCSEL quantum efficiency. [3] Figure 3.4 shows the ion and vacancy distributions in the top AlGaAs DBR mirror of EMC5978 as calculated by SRIM2000 with an implant energy of 56 keV and an implant dose of $5x10^{14}/cm^2$. [4, 5] A photoresist layer with a thickness of ~1.3 μm is enough to block all protons with an average energy of 70 keV as illustrated in Figure 3.6 (a). Therefore, photoresist is usually used as the implant mask at CSU. Alternatively, a thin layer of metals can be also used as the implant mask. As a comparison, the VCSEL with 500 Å AuGe alloy (88%:12% weight percent)/ 400 Å Ni /1000 Å Au contact layers covered on the top is implanted as shown in Figure 3.5. The energy for an effective current confinement is required ~ 95 keV. Blocking all protons with such a large energy needs a photoresist layer as thick as ~1.8 μm shown in Figure 3.6 (b).To get a fairly sharp edge profile of photoresist at this thickness requires more fabrication steps, which are discussed in detail in Chapter 4.

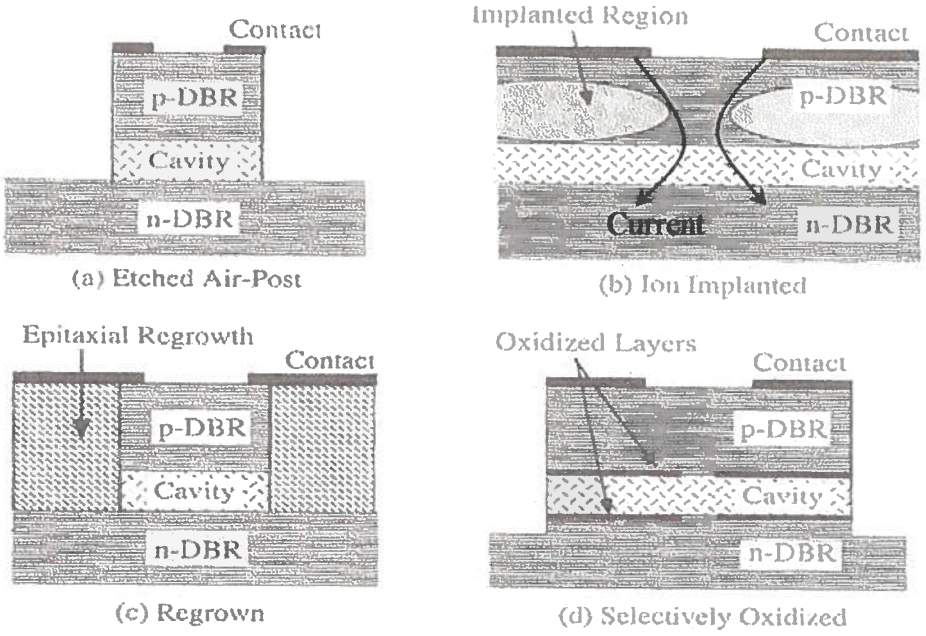

Figure 3.3 Four general current confinement structures for VCSELs: (a) etched mesa, (b) ion implanted, (c) buried heterostructure, (d) selectively oxidized. (Copied from reference [3])

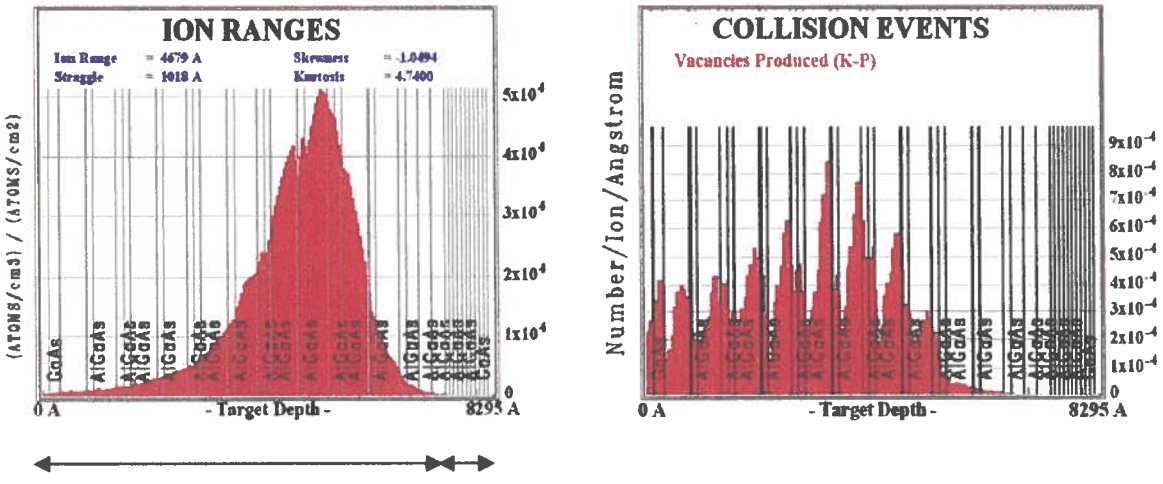

Figure 3.4 Proton implant simulated by SRIM2000: (a) ion distribution, (b) vacancy distribution in the top n-type AlGaAs DBR mirrors of the half VCSEL EMC5978. The implant parameters are 56 keV for implant energy, $5x10^{14}/cm^2$ for implant dose and 7 degrees for implant direction. Photoresist is used as an implant mask.

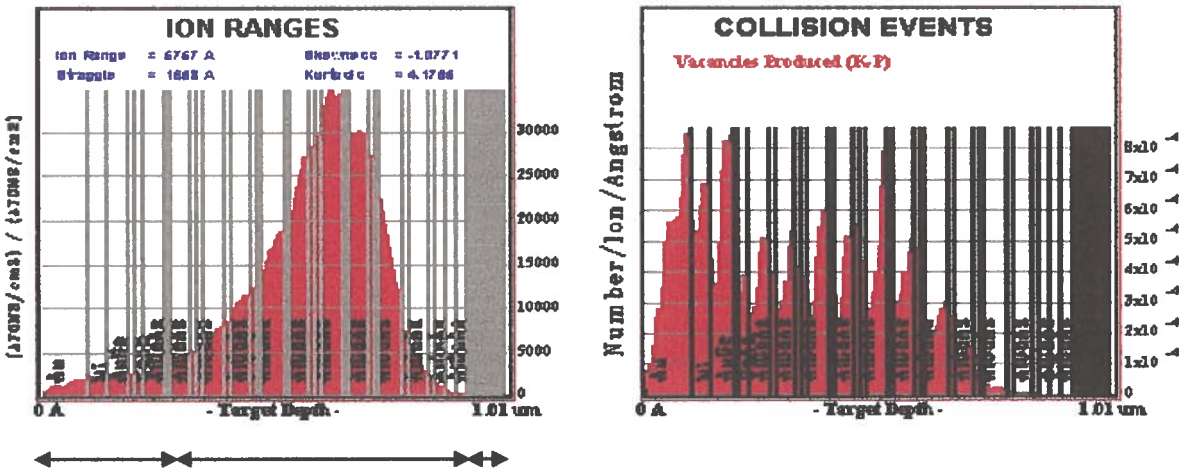

(Au/Ni/AuGe)/n-type DBR mirror/ MQW active region/

(a) (b)

Figure 3.5 Proton implant simulated by SRIM2000: (a) ion distribution, (b) vacancy distribution in the top n-type AlGaAs DBR mirrors of the half VCSEL EMC5978. The implant parameters are 95 keV for implant energy, $1x10^{15}/cm^2$ for implant dose and 7 degrees for implant direction. VCSEL top surface is covered by 500Å AuGe alloy (88%:12% weight percent)/ 400 Å Ni /1000 Å Au contact layers. And photoresist is used as an implant mask.

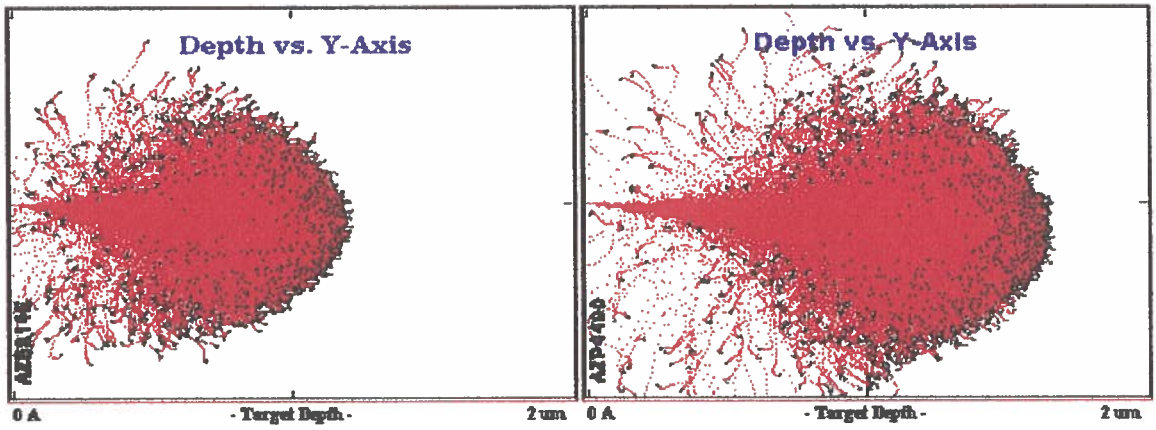

(a) (b)

Figure 3.6 Pictures showing the proton is blocked by the photoresist implant masks: (a) ~1.3 μm thick resist layer is required to block proton with an average energy of 70keV, (b) ~1.8 μm thick resist layer is required to block proton with an average energy of 100 keV, as simulated by SRIM 2000.

3.1.3.2 Dielectric Mirror

A half VCSEL with a DBR mirror intensity reflectivity less than 60% cannot lase properly. Thus, a separate highly reflective dielectric mirror is required in our biosensor. In order to decrease mirror losses and threshold current of VCSELs, a typical reflectance value over 99.75% is required. The mirror used in our biosensor is comprised of 10 pairs SiO_2/ Si_3N_4 quarter-wavelength layers grown on a thin Pyrex cover glass with a passband center at 848.6 nm as illustrated in Figure 3.7 and 3.8. [6] Dr. Stewart A. Feld, a previous student in our lab, fabricated the mirror for us at Cielo Communications, Inc. The value of 99.75% intensity reflectivity was calculated by the equation

$$R(\lambda) = \Gamma_{i+1}^{*}(\lambda)\Gamma_{i+1}(\lambda),$$

$$\Gamma_{i+1}(\lambda) = \frac{r_{i+1}(\lambda) + \Gamma_i(\lambda)\exp[-j2\beta_i(\lambda)l_i^{eff}]}{1 + r_{i+1}(\lambda)\Gamma_i(\lambda)\exp[-j2\beta_i(\lambda)l_i^{eff}]},$$

$$\Gamma_1(\lambda) = r_1(\lambda),$$

$$r_i(\lambda) = \frac{n_i - n_{i-1}}{n_i + n_{i-1}},$$

$$\beta_i(\lambda) = \frac{2\pi n_i(\lambda)}{\lambda}, \qquad (3.1)$$

where $\Gamma_{i+1}(\lambda)$ is the field reflectivity at layer i, as shown in Figure 3.7, whereas the local reflectivity between layers i and $i-1$ is represented by r_i, and $\Gamma_{i+1}^{*}(\lambda)$ is complex conjugate of $\Gamma_{i+1}(\lambda)$.[7]

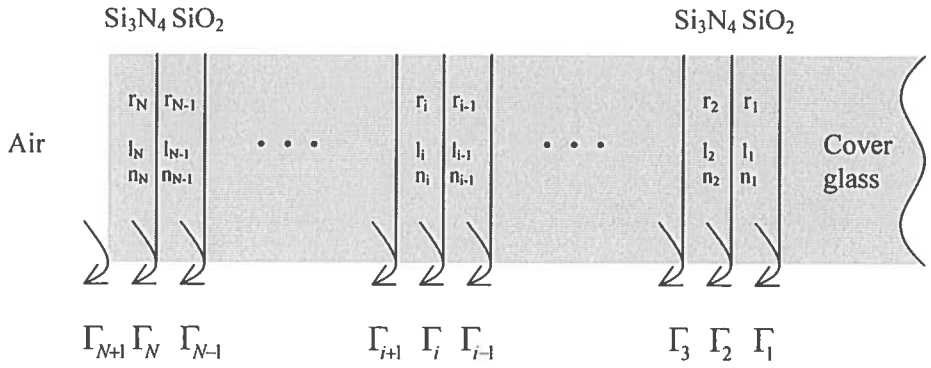

10 pairs SiO_2/ Si_3N_4 quarter-wavelength layers, $N = 20$,
where $n_{SiO_2} = 1.46$ and $n_{Si_3N_4} = 2.02$, respectively.

Figure 3.7 Schematic diagram for 10 pairs SiO_2/ Si_3N_4 quarter-wavelength layers dielectric mirror grown on a thin Pyrex cover glass with a thickness of ~229 μm. (Copied from reference [7])

Note another important issue for the dielectric mirror is mirror tilting when the dielectric mirror is bonded to the half VCSEL by the gasket/spacer. Although both the mirror and the half VCSEL can be assumed super flat, the gasket/spacer will either swell or shrink in response to the change of the process temperature, consequently, a surface variation may occur resulting in a tilt of the mirror. Fortunately, a flat photoresist surface can be obtained by spinning it at very high speed. Further uniformity improvement can be obtained by an edge extension technique discussed in the next chapter. To keep this flat situation during bonding, a force is applied to the structure during this step. More details are given in Chapter 4.

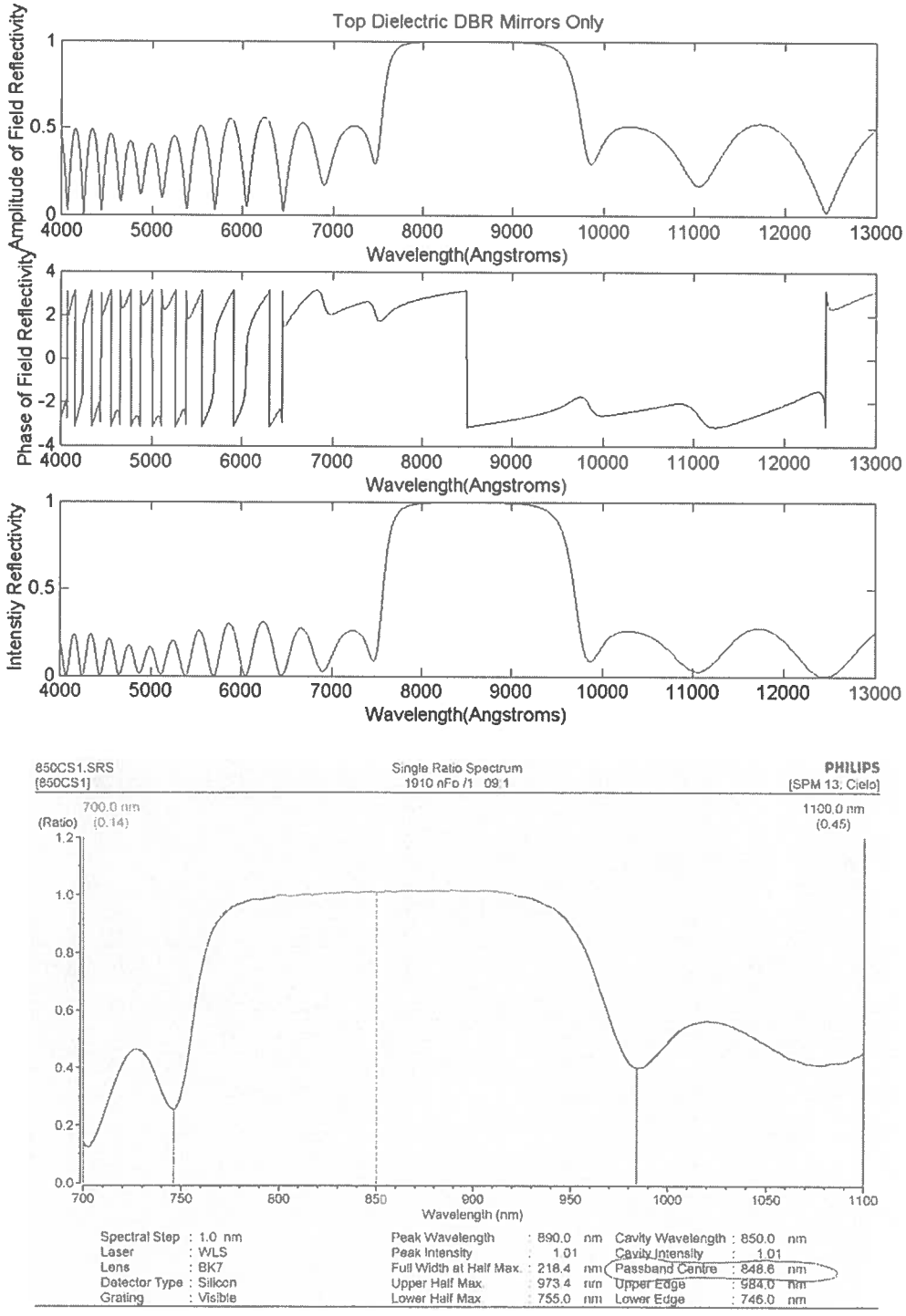

Figure 3.8 Mirror characteristics of 10 pairs SiO_2/ Si_3N_4 quarter-wavelength layers dielectric mirror grown on a thin Pyrex cover glass: (a) field reflectivity, (b) phase, (c) intensity reflectivity simulated by Matlab, and (d) experimental results of dielectric mirror intensity reflectivity provided by Dr. Stewart A. Feld (Copied from reference [6]).

3.1.3.3 Fluidic Cavity Dimensions and Fluid Transportation Methods

The thickness of the spacer/gasket is a critical parameter for operation of the laser. Large spacings introduce more diffraction loss, lower cavity Q, and higher pumping thresholds for lasing. Small spacings can cause difficulty in transporting fluids into the intracavity space. There is difficulty in wetting either the glass surface or the semiconductor surface after such fabrication steps as metal evaporation, wafer etching, bonding, gluing or sealing, which can modify the surface conditions. Considering the size of common biological cells and the performance optimization between laser and fluid transportation, a fluidic cavity spacer around 5 μm thick is seen as a good choice. It is slightly larger than the normal red blood cell which is about 7 μm in diameter and 2 μm in thickness. [17] Under this condition, the interference with signals from individual cells caused by cell layer overlapping in the direction of the light output will be alleviated and a method based on a capillary action can be applied to feed fluid into the cavity. An alternative method used by Sandia National Laboratories discussed in Chapter 2 places a wicking bridge inside the microcavity. Using Sandia's analysis [1] we estimate the filling time for our fluidic cavity to be less than 1 second. This was verified by experiments discussed in Chapter 5.

3.1.3.4 Fluid Interconnections and the Corresponding Sealing Methods

Since our biosensor is a fluidic device, fluid interconnections are required to connect the VCSEL fluidic cavity with the fluid source reservoir and with the fluid drain reservoir. Generally, the interconnections can be either microchannels or microtubes, formed by etching, deposition or gluing. A common issue for these fluidic cavities and fluid traces is

the fluid leakage, which will degrade the electrical performance of the device and cause a reliability problem. Therefore, designing good fluid traces and effective sealing methods for cavities and interconnections becomes one of the most challenging fields in biosensor design. We have elected to use a capillary tube to supply the fluid to the VCSEL fluidic cavity. The detailed dimensions of the capillary tube and fluidic cavity are shown in Figure 3.11 and 3.12, respectively. The capillary tubes have good fluid confinement, thus the leakages can only occur in the cavity and the places where cavity is connected to the capillary tubes. For the cavity, sealing with photoresist is effective because the resist has good sealing performance after a long cure at 90° C with an applied force. For the connections to the capillary tubes, epoxy is promising since it is adhesive and deformable. Chapter 4 provides the detailed process for sealing.

3.1.4.5 Surface Passivation and Fluidic Cavity Cleaning

Two processes that may lead to degradation of the biosensor are: 1) oxidation of the GaAs/AlGaAs by water and 2) the adhesion of the cells to the cavity walls. GaAs is not oxidized in water that is applied in an inert atmosphere. [8] However, when the water contains dissolved oxygen, then a thick layer of Ga_2O_3 will form [9, 10], especially in the presence of intense light such as found in the cavity of a VCSEL. [11] Applying a thin film of SiO_2, Si_3N_4 or ITO should prevent this oxidation. The interactions of biological materials with microfabricated structures will lead to a fluid suspension in the fluidic cavity after about a minute due to the adhesion of both proteins and cells to semiconductors, metals, polymers or glass surfaces. [12]. Proteins tend to absorb to the surface first, due to concentration and kinetic factors. The binding and proliferation of

cells can lead to biofilm formation. The adhesion depends on the material's surface free energy, topology and chemistry. Figure 3.9 shows the cell adhesion and aggregation in and around the microfluidic channels during the flow of cells. [12] In order to alleviate the numerous problems associated with the biofilm formation, the surface passivation becomes an important topic of research and many efforts have been devoted to this field. The best passivation material is the one that can not only resist cell and protein adhesion, but also be reusable. Self-assemble monolayer (SAM) was investigated by Darryl Y. Sasaki, *et al.* from Sandia National Laboratories. As an example, TESP effectively passivates the microfluidic structure to cell adhesion and biofouling.[12] Although currently the principle of passivation is not very clear, an alternative solution is very effective by cleaning the fluidic cavity after biosensing, including DI water/nitrogen purging or organic solvent cleaning. [1] As a simple case, no surface passivation layer is used in our biosensor prototype. Instead, AuGe/Ni/Au contact layers are used to protect the semiconductors. We have no idea whether the metals are passive to biological fluids.

3.2 Final Device Structure and Mask Design for Biosensor Prototype

The composite mask set and final structure for our first generation electrically pumped VCSEL based intracavity fluidic biosensor are presented in Figure 3.10 and Figure 3.11, respectively, after carefully considering the issues as mentioned in the previous sections of this chapter. Size matching between the VCSEL fluidic cavity and capillary tubes are provided by Figure 3.12. The device masks are drawn using LASI, one of professional CAD softwares for mask designing. The LASI manual can be found in reference [13].

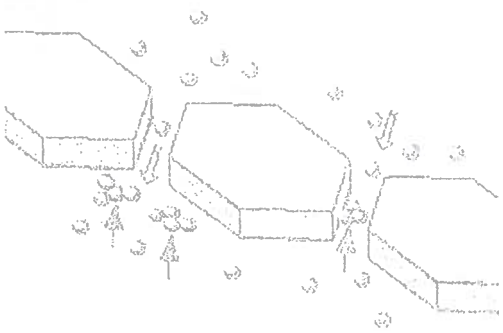

Figure 3.9 Schematic diagram of cell adhesion and aggregation (black arrows) in and around the microfluidic channels during flow of cell containing medium. (Copied from reference [12]).

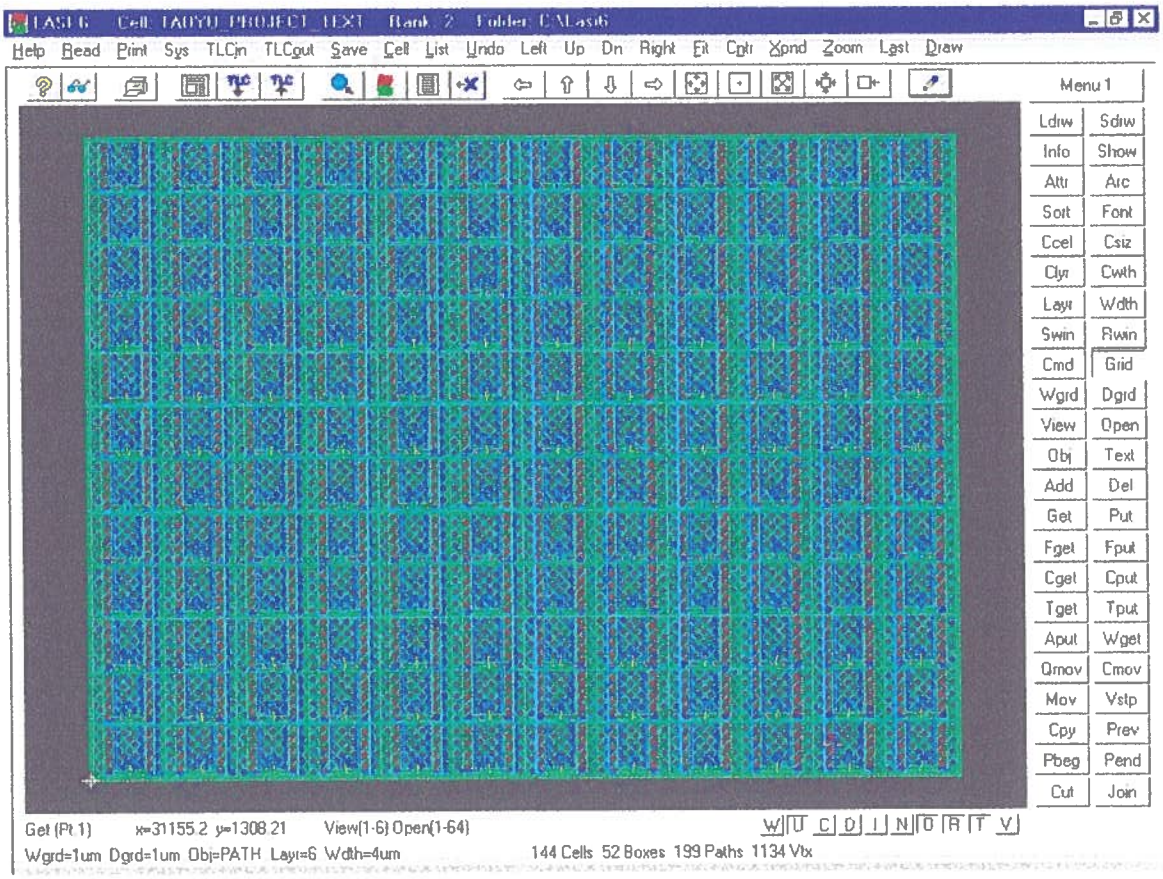

Figure 3.10 Composite drawing of the first generation VCSEL based intracavity fluidic biosensor mask set, designed with LASI.

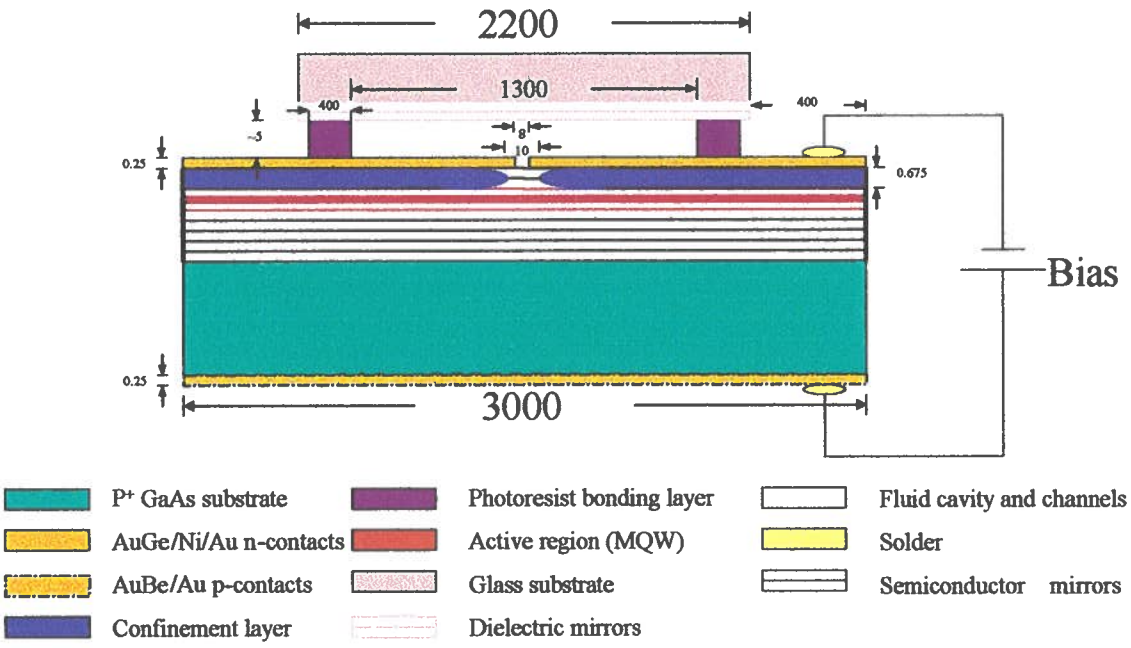

(a)

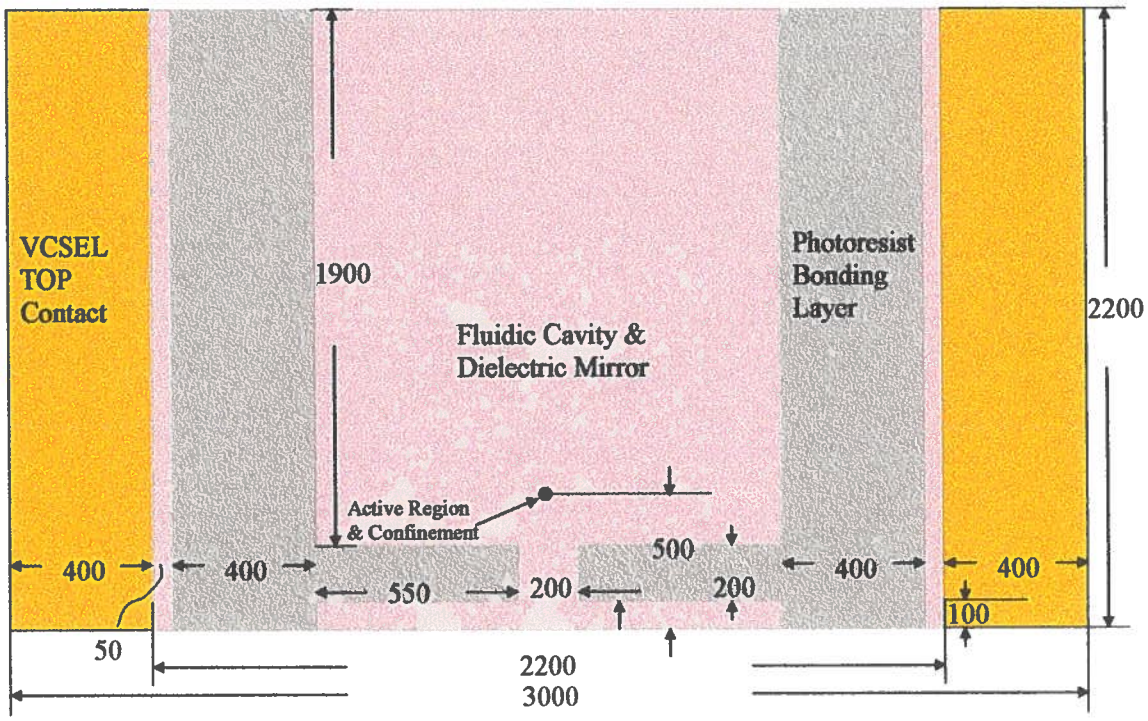

(b)

Figure 3.11 (a) Cross-section and (b) top view of the first generation electrically pumped VCSEL based intracavity fluidic biosensor, designed by PowerPoint. All dimensions are in microns. The size of the VCSEL aperture is not to scale.

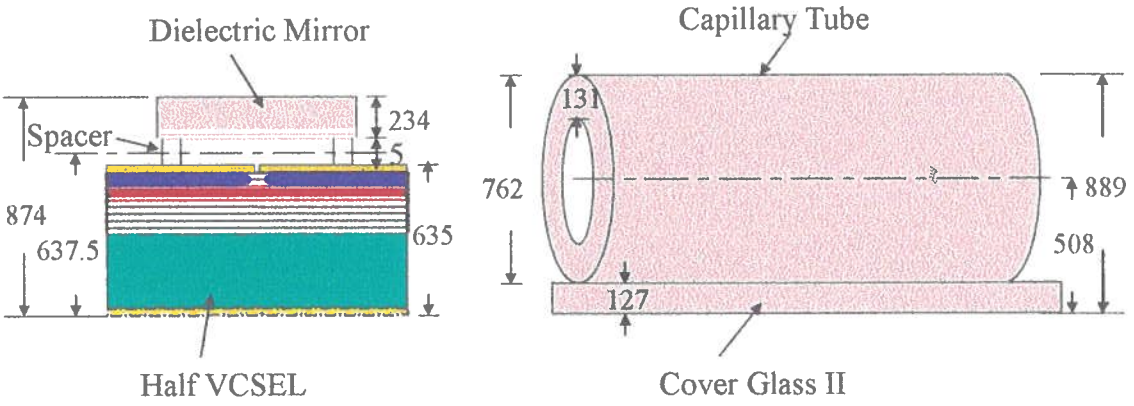

(a)

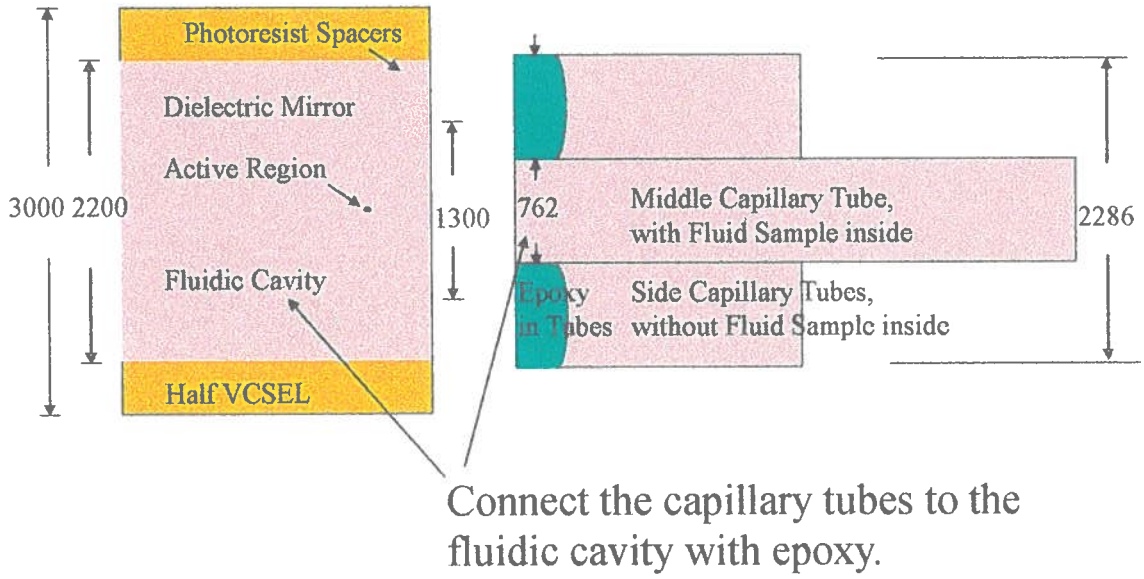

(b)

Figure 3.12 (a) Cross-section and (b) top view of the connection between capillary tubes and fluidic cavity of the VCSEL, designed by PowerPoint. All dimensions are in microns. The size of the VCSEL aperture is not to scale.

3.3 Simulations of Electrically Pumped VCSEL Based Intracavity Fluidic Biosensor

3.3.1 Simulations for Longitudinal Mode Shift Vs. Average Refractive Index Change

The relationship of the longitudinal mode wavelength shift with respect to refractive index change in our device is different from that in the Gourley biosensor, because our biosensor utilizes a SCC structure, while theirs has a FCC structure. As mentioned in Section 3.1.2, wavelength shifts linearly with a change of cell index for a FCC biosensor, as represented by Eq (2.3). For a SCC biosensor, the effect of the effective optical pathlength change in Eq (2.3) is replaced by that of the mirror phase change as expressed by

$$\frac{2\times 8500}{\lambda_l} = \frac{\phi_T + \phi_B}{2\pi} + l, \tag{3.2}$$

where 8500 is the effective optical pathlength of the laser optical cavity with units of angstroms calculated according to the EMC5978 data sheet. The parameter ϕ_T and ϕ_B represent the phases for the total top and bottom mirrors, respectively. In this case, ϕ_T changes periodically and l is a constant equal to 2. Consequently, the longitudinal mode wavelength shifts back and forth as shown in Figure 3.13. The resonant wavelength is tuned to 850 nm when the fluidic cavity has parameter values of $l_1 = 54643\,\text{Å}$ and $n_1 = 1.33$, i.e., water inside the fluidic cavity. The reasons for these setting are:

(1) The top contact metal layers are totally about 2000 Å and increase the total thickness of fluidic cavity.

(2) The phase of the total top mirrors is zero for this setting.

(3) Most cells live in a liquid environment with index values close to 1.33.

(4) This kind of setting optimizes the sensitivity of the device because 850 nm is currently in the middle part of the nominal wavelength range for gain which is set to 850 ± 10 nm considering the wavelength temperature dependence (red shift), the electrically pumping capability (blue shift) and several possible optical losses in the fluid cavity. [3, 14, 15]

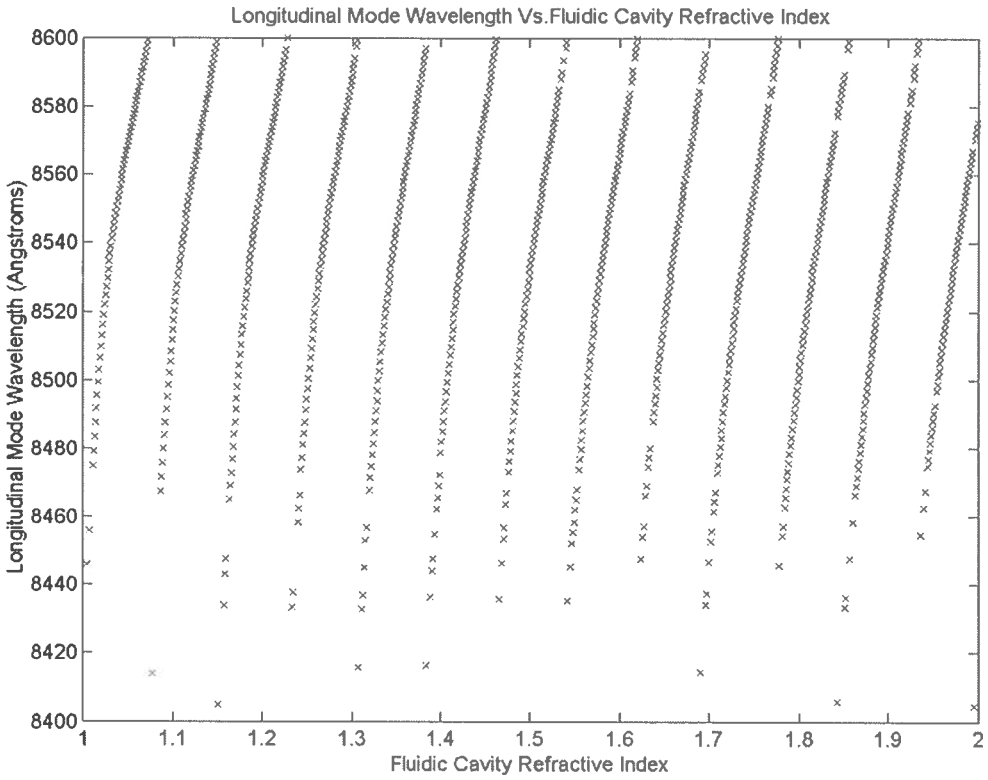

Figure 3.13 Longitudinal mode wavelength shifting vs. fluidic cavity average refractive index changing, simulated by Matlab. The resonant wavelength shifts back and forth in the wavelength range for gain from 840nm to 860 nm. The actual gain region may be wider. The mode shift is quasi-continuous with an incremental step of 0.001 in index change.

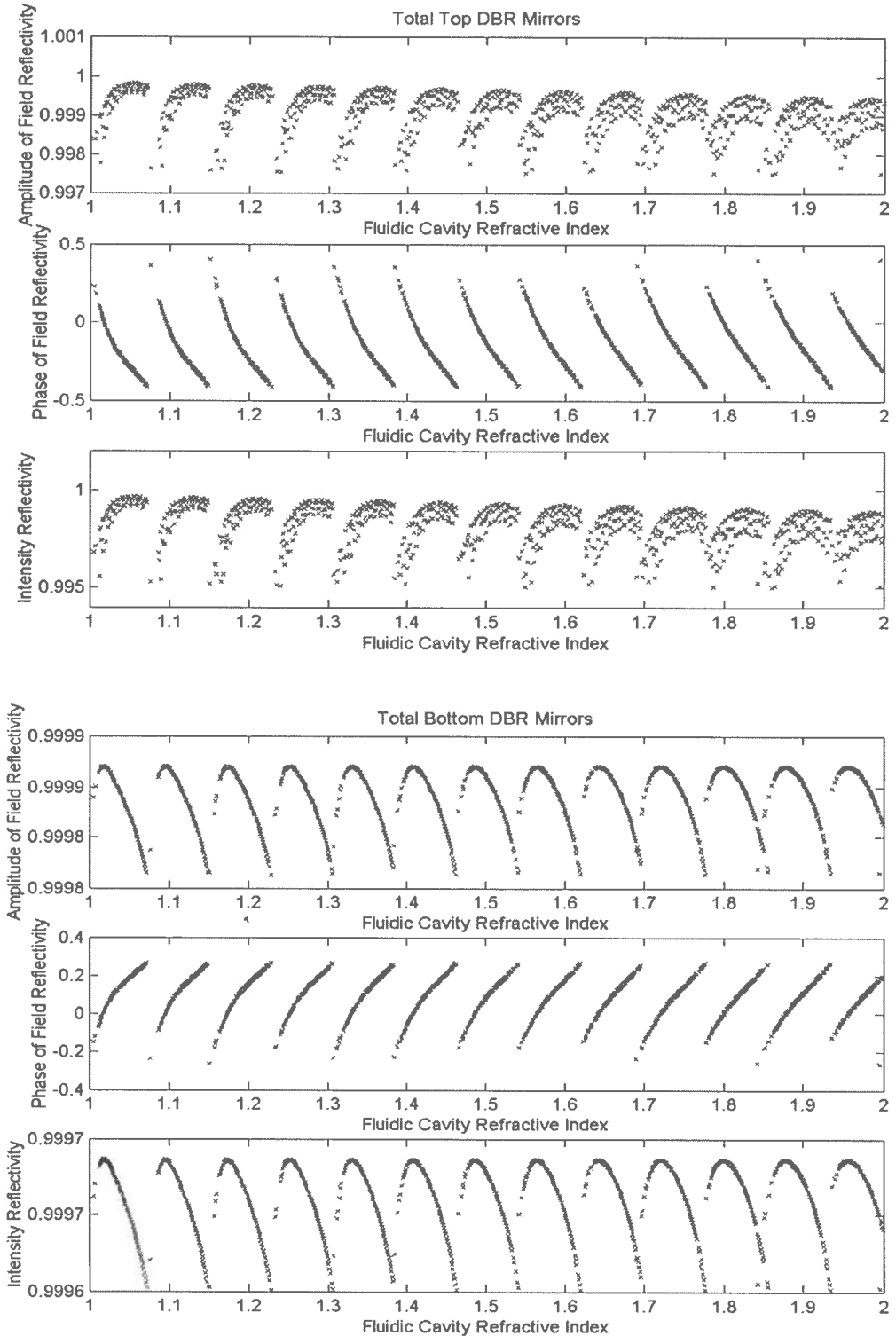

Figure 3.14 Matlab simulations showing that both (a) top mirrors and (b) bottom mirror have very high intensity reflectivities for each resonant wavelength shown in Figure 3.13.

The simulations indicate that our first generation electrically pumped VCSEL based intracavity fluidic biosensor has a minimum detectable wavelength change of about 0.01 nm corresponding to an index change of 10^{-5} comparable to that in the Gourley biosensor. Approximately 6 nm wavelength shifting is expected to occur when water naturally evaporates from the cavity according to the simulation results shown in Figure 3.13 (be aware that the experimental results could different from the simulations, since the cavity conditions may change), while a 7 nm shift was reported by Gourley, as shown in Figure 2.4. Therefore, our biosensor should have a similar sensitivity as the one from Sandia National Laboratories.

Some points should be clarified. First, not all values of fluid cavity refractive indice have a corresponding resonant mode during the simulations. That means there are some types of cells with special index values that may be undetectable by our biosensor. The lost modes arise not only from the numerical convergence problem of simulations but also from misalignment between laser gain region and resonant modes. In order to lower the threshold current for lasing, a high intensity reflectivity value of 99.5% for mirrors is basically required, which can lead to further mode loss. Therefore, the wavelength shift is quasi-continuous with an incremental step of 0.001 in index. Figure 3.14 shows the mirror reflectance for each wavelength shown in Figure 3.13. The minimum reflectance value for the total top DBR mirror is 99.5%. Secondly, the simulations assume the wavelength range for gain is 20 nm, i.e., 840~860 nm. The typical value for actual lasers is around 10 nm or more. [15] Thirdly, one wavelength probably corresponds to multiple index values. The wavelength values in Figure 3.13 are accurate to 0.1 Å. At this scale,

the wavelength is distinguished from others. Experimentally, it will be limited by the resolution of the spectrometer. Finally, as a simple case, the simulations do not consider the effect of optical absorption by the biofluid samples as well as the wavelength shift caused by the cell waveguiding effect as mentioned in Section 2.2.2. The actual relationship of wavelength shift versus index change is complex.

3.3.2 Simulations for Influence of the Fluidic Cavity Spacing on Mode Wavelengths

In our design, photoresist spacers are used to form the fluidic cavity. However, the thickness of photoresist is variable, depending on many factors such as surface conditions, spinning speed, temperature, development time or strength of magnetic forces. Figure 3.15 shows the simulation results for the influence of the fluidic cavity spacing on mode wavelengths. The results indicate only a few thicknesses with mode loss, mainly caused by the limitation of the mirror reflectance and numerical convergence problem of simulation as illustrated in Figure 3.16. The simulations have the same configuration to that in previous one, i.e., tuned at 850 nm for $l_1 = 54643\,\text{Å}$ and $n_1 = 1.33$.

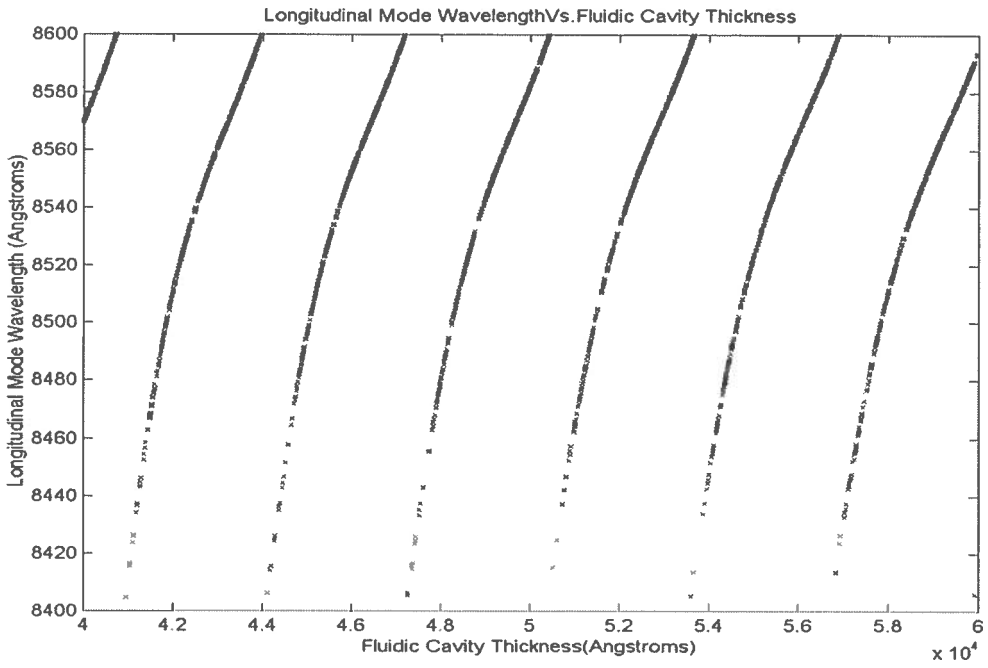

Figure 3.15 Simulations for influence of the fluidic cavity spacing on mode wavelengths. A quasi-continuous shift is indicated. The simulations are configured at 850 nm for a fluidic cavity with $l_1 = 54643\,\text{Å}$ and $n_1 = 1.33$.

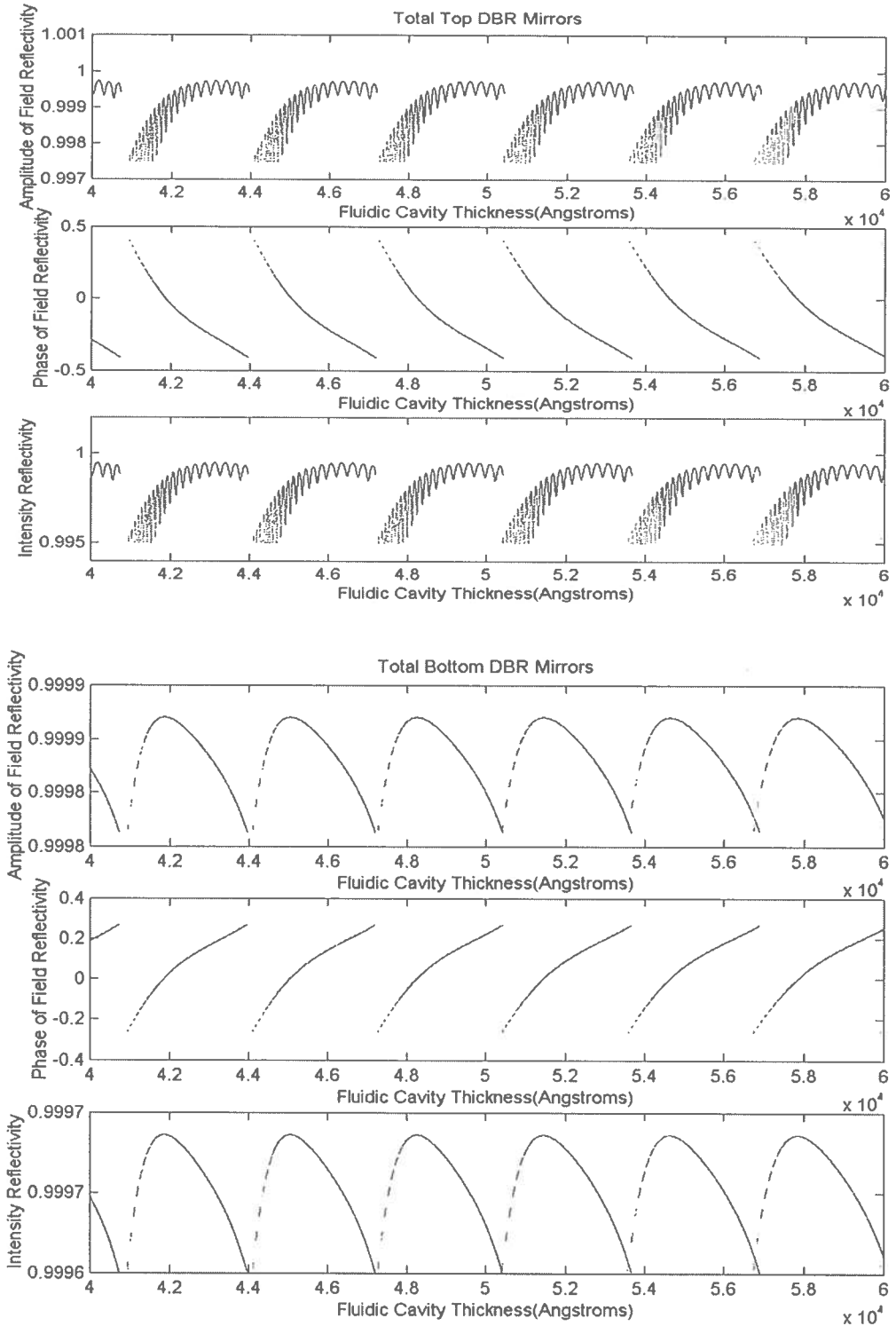

Figure 3.16 Matlab simulations showing that both (a) top mirrors and (b) bottom mirror have very high intensity reflectivities for each resonant wavelength shown in Figure 3.15.

3.4 Summary of Chapter 3

For a device to progress from concept to realization, it generally goes through five stages: design, simulation, fabrication, test and package. A good design will improve the device performance, save time as well as lower cost. Therefore, during this stage, most major issues that may arise in our electrically pumped VCSEL based intracavity fluidic biosensor design are listed in this chapter and the corresponding solutions are given. Finally, a SCC biosensor prototype is proposed. The results of simulations show the biosensor can work well as previously proposed with a quasi-continuous wavelength shift with respect to the change of the cell index. In addition, the fluidic cavity thickness really influences the mode wavelength seen from the simulations. Fortunately, the resonant mode still exists except only a few cavity spacings, which give us a flexibility to control the photoresist thickness in the device fabrication.

References:

[1]. P.L. Gourley and A. E. McDonald, "Semiconductor microlasers with intracavity microfluidics for biomedical application", *Proc. SPIE* 2978, pp.186-196 (1997).

[2]. Andy Allerman, Terry Hargett, and Rob Sieg, "EMC5978 MOVPE growth data sheet", *Sandia National Laboratories*, July, 2000.

[3]. Carl Wilmsen, Henryk Temkin, and Larry A. Coldren, "Vertical-cavity surface-emitting lasers", *Cambridge University Press*, p.200, p.224, 1999.

[4]. "Manual for SRIM2000", *http://www.srim.org/#SRIM*

[5]. Stewart A. Feld, "Ph.D. Dissertation", *Colorado State University*, pp.166-171 (1996).

[6]. Stewart A. Feld, "Intensity reflectivity data sheet for 20 pairs Si_3N_4/SiO_2 quarter-wavelength layers grown on a thin Pyrex cover glass with a passband center at 850 nm", (2002).

[7]. Govind P. Agrawal, "Semiconductor lasers: past, present, and future", *AIP Press*, p150 (1994).

[8]. D. E. Aspnes and A. A. Studna, "Chemical etching and cleaning procedures for Si, Ge, and some III-V compound semiconductors", *Appl. Phys. Lett.*, 39, pp.316-318 (1981).

[9]. B. Schwartz, S.E. Haszko and D.R. Wonsidler, "The influence of dopant concentration on the oxidation of GaAs in H_2O", *J. Electrochem. Soc.*,118, pp.1229-1231 (1971).

[10]. Z. Lillental-Weber, C.W. Wilmsen, K.M. Geib, P.D. Kirchner, J.M. Baker and J. M. Woodall, "Structure and chemical composition of water-grown oxides of GaAs", *J. Appl. Phys.*, 67, pp.1863-1867 (1990).

[11]. C.W. Wilmsen, P.D. Kirchner, J. M. Baker, D. T. Mcinturff, G. D. Pettit, and J. M. Woodall, "Characterization of photochemically unpinned GaAs", *J. Vac. Sci. Technol.*, B6, pp.1180-1183 (1988).

[12]. Darryl Y. Sasaki, *et al.*, "Glial cell adhesion and protein adsorption on SAM coated semiconductor and glass surfaces of a microfluidic structure", *Proc. SPIE* 4265, pp.152-163 (2001).

[13]. G.Y. Robinson, "LASI Manual", *www.engr.colostate.edu/EE534/lasi/lasi_list.html*

[14]. Shun Lien Chuang, "Physics of optoelectronic devices", *John Wiley & Sons, Inc*, (1995).

[15]. Kevin Lear, "Course slides for EE525 fiber optical communications", p.55 (2001)

[16]. *http://omlc.ogi.edu/spectra/hemoglobin/*

[17] P.L. Gourley, T.French, A. E. McDonald, E.A. Shields, and M. F. Gourley, "Ultrasensitive detection of red blood cell lysing in a microfabricated semiconductor laser cavity", *Proc. SPIE* 2978, pp.195-206 (1998).

CHAPTER 4

FABRICATION OF ELECTRICALLY PUMPED VCSEL BASED INTRACAVITY FLUIDIC BIOSENSOR

4.1 General Considerations and Methodologies for Processing

The fabrication of the electrically pumped VCSEL based intracavity fluidic biosensor requires the resolution of at least four issues:

1). How to fabricate the half VCSELs.
2). How to form a uniform and sealed fluidic cavity with ~5 μm thick photoresist.
3). How to connect the capillary tubes to the device and seal the connection.
4). How to place and assemble the whole biosensor system.

In this section, all fabrication questions are discussed and corresponding process methodologies to solve these problems are presented.

4.1.1 Methodologies for Half VCSEL Fabrication

As mentioned in the last chapter, a half VCSEL with a proton implanted current confinement structure is used in our first generation biosensor. There are four major processing steps in this kind of VCSEL fabrication. Given in the order in which they are performed, they are: bottom p-ohmic contact layer evaporation, alignment mark transfer, active area proton implantation and top n-ohmic contact layer formation. In addition, it is found that wafer cleaving which can produce several samples with the sizes suitable for

cover glass handling is executed before all of the above processing steps. Cutting this sample into individual VCSELs occurs after the sample fabrication. During the sample processing stages, the bottom p-ohmic contact layer formation is applied first since no pattern is required just an overall metal covering on the backside of the VCSEL sample. Most important of all is the need to minimize the effect associated with annealing AuBe/Au contacts at a high temperature of 440 °C. Although there are several sample heating steps latter, the change of the contact resistance is neglected as long as the temperature is below 200 °C. The next processing step is the alignment mark transfer, which provides a convenient way for pattern mask aligning. The third step is the active area proton implantation, where effective implantation masks are required to protect the areas in which the current confinement is unwanted. This step is time-consuming due to the difficulty in creating a good implant mask. Finally, the top n-ohmic contact layers are evaporated and then annealed if necessary. It should be noticed that the last two steps are most important since they determine the VCSEL yield of the whole fabrication as well as have great effects on the VCSEL performances such as VCSEL resistances, *V-I* characteristics and quantum efficiencies.

Two points should be clarified. Firstly, there is no difference when the alignment mark transfer is executed before the p-ohmic contact formation. Secondly, compared to the proton implantation, the n-ohmic contact formation has the lowest yield since the top contacts are only about 0.7 μm above the MQW active region in the half VCSEL wafer EMC5978, easily resulting in large current leakages and thus device failures during contact annealing. The diffusions of Au into the quantum wells possibly cause this

problem. Therefore, in principle, this step should be done before the implantation since less time and expense could be wasted on processing if the failures occur at this step. Another advantage of this arrangement is alleviating the problem of the high contact resistance to the VCSEL after it has been implanted with the protons. It is thought that the damage tail of the active area proton implantation (see Figure 3.4(b)) causes the surface of the VCSEL wafer to become less conductive, making formation of low resistance ohmic contacts more difficult. [1] Moreover, this processing order also prevents the ~380° C n-ohmic contact annealing from activating ions into the lattice sites again, resulting in current confinement failures if the implantation is first. However, the disadvantage is that a sufficient current confinement in such a way requires a proton implant energy as large as ~ 95 keV because the protons have to go through the AuGe/Ni/Au contact layers first before they reach to the VCSEL sample. That means a thicker well defined photoresist implant mask is required. This photolithographic step is the most difficult of the whole processing. From the points of the initial design, the process **Recipe I** where the implantation is executed before the n-ohmic contact formation is tried first, since 1.3 μm thick photoresist simulated by SRIM is sufficient to block all protons and to attain a fairly sharp edge profile of photoresist at this thickness is not very difficult. During the research, the process **Recipe II** in which the implantation is performed after the n-ohmic contacts is also investigated. In this strategy, the alignment mark etching step is not required, since the marks can be formed together with the contact patterns using a lift-off technology described in reference [1]. This arrangement also helps investigate whether the leakage currents occur at the positions where alignment marks are etched. The details of Recipe I and II are given in Appendix D.

4.1.2 Methodologies for Spacer Formation

The reasons to choose photoresist as fluidic cavity spacer are threefold. Firstly, the process is very simple compared to other approaches such as deposition, sacrificial technology and LIGA (German-language acronym of lithography (LI=lithogafie) electroplating (G=Galvanoformung) and molding (A=Abformung), which represent all these different processes required in microfabrication). [3-4] Photoresist can be easily coated onto the surface of the VCSEL wafer by a standard photoresist spinner. Secondly, the thickness of the photoresist can be changed by adjusting the spinning speed. The faster the speed, the thinner the layer. Thirdly, photoresist is an inert material that does not react with biofluids under normal conditions. To obtain a ~5 μm well-sealed fluidic cavity, four problems associated with photoresist spacers should be overcome. The first issue is the presence of the air bubbles in the resist, which stay suspended longer in the more viscous resist and form pin-holes in the final resist layer. The source of these bubbles is traced to the 0.2 μm filter and syringe arrangement typically used to manually deposit the resist. [1] The spacer material used in our biosensor is the photoresist SJR5440 with a medium viscosity, thus few bubbles are presented. Although filters with smaller size are preferred, they are more expensive. The second problem is the uniformity of the spacer thickness. Usually the photoresist coating is uniform across the wafer except the edges, where a thicker layer will exist. For example, ~5 μm uniform thickness of SJR5440 can be obtained at the center part of the sample through spinning at 4400 rpm, while it is about 10 μm thick at the edges as measured by Alpha Step. This build-up of resist at the edge of the sample is referred to as an "edge-bead". [1, 2] For a larger size VCSEL sample, the most effective way to remove these edge-beads is UV exposure

followed by development. A special glass mask is used to expose the resist at one edge of the sample to the UV light and then rotate the sample and repeat the same operation for the other edges. The exposure time for the edge-bead removal is longer than that of pattern formation, usually three or four times, so that the development time can be shorten to avoid over developing of the center part. Alternatively, edge-beads can be removed with a razor blade. However, extreme care must be taken in order to avoid scratching the sample. Unintended scars left on the sample are etched faster in chemical wet etching and cause unexpected current leakage paths if they penetrate deep into the active region. On the other hand, if the sample is small, an edge extension as illustrated in Figure 4.1 can be used to alleviate the edge-bead effect. The standard 3-inch GaAs wafer has a thickness of 635 μm, which is comparable to the EMC5978 half VCSEL wafer. In this method, each edge of the VCSEL sample is abutted to a bare GaAs piece. Since the merge doesn't introduce large steps at the interfaces, the edge-beads will move to the edge of the GaAs pieces from the sample, leaving behind a uniform resist. Photoresist spacers are spun onto the sample immediately after the step of slightly scoring the sample which leaves pixel boundaries on the sample but doesn't actually break it. By this means, more pixels with uniform spacers can be achieved even though the dimension of the sample is small. Scoring after the gasket fabrication could damage the resist patterns and the residues of resist remaining on the wafer surface are difficultly removed by DI water and Nitrogen. The third issue associated with the spacer formation is the shape change of the resist with respect to the processing temperature. When the temperature is above 120 °C, reflow occurs for most photoresist. Consequently, photoresist spikes formed at pattern edges as shown in Figure 4.2(b) cause an increased spacer thickness as well as a surface

variation, probably leading to a failure in cavity sealing. Experimentally, spacers cured at 90 °C together with an external force not only hold the shape of the resist but also achieve a good cavity sealing performance. The last problem is photoresist adhesion. After the process of baking, exposure, development and drying, the front surface of the photoresist becomes less adhesive and makes bonding more difficult. Fortunately, this issue also can be resolved by the method mentioned in the previous problem, i.e., spacer cure at 90 °C together with an external force.

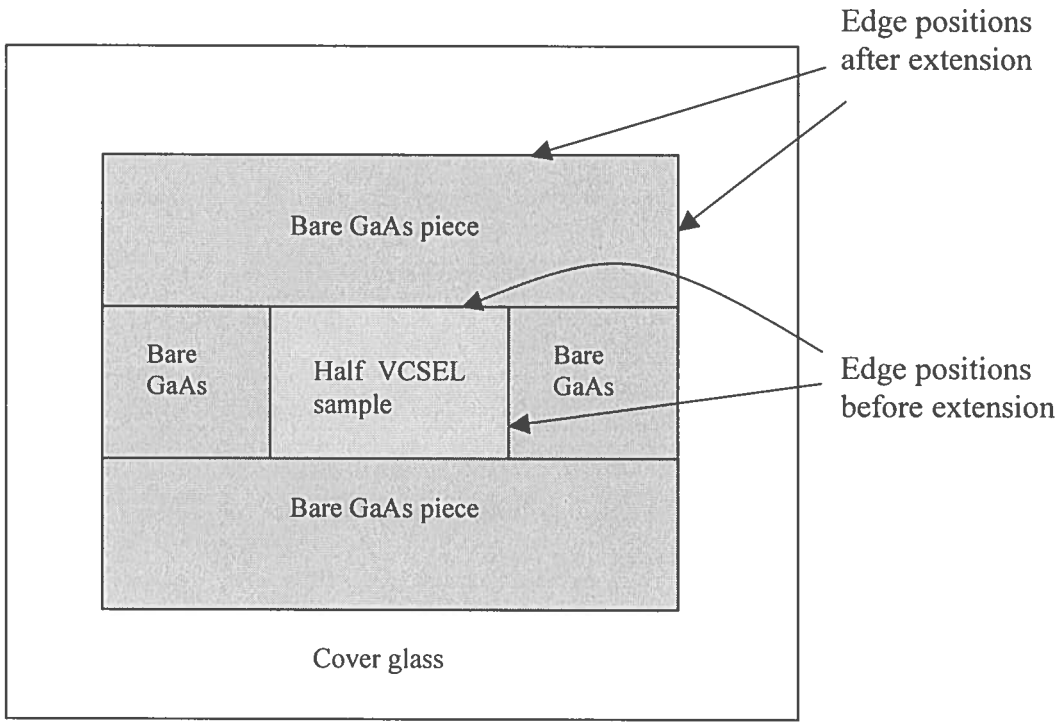

Figure 4.1 Schematic diagram showing an edge extension approach to alleviate the edge-bead effect. For a small rectangular half VCSEL EMC5978 sample, four bare GaAs pieces are adjacent to the sample. Consequently, the edges are extended to the bare GaAs.

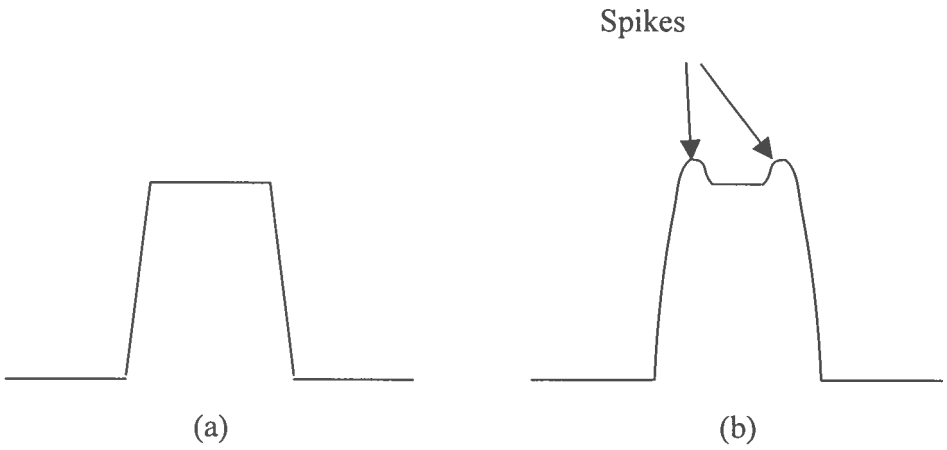

Figure 4.2 Schematic diagram showing photoresist reflow after a cure at a temperature of 120 °C: (a) before curing and (b) after curing.

4.1.3 Methodologies for Interconnection Assembly and Biosensor System Arrangement

As mentioned in Chapter 3, capillary tubes are used for the fluidic interconnections and epoxy seals the connections where the capillary tubes joint to the fluidic cavity. Although a single tube is used to contact the entrance of the cavity, it is difficult to attach epoxy to the connection face of this tiny tube, because epoxy can be sucked into the tube by capillary action and thus block the passage of the biofluids. A simple way to solve this problem in the fabrication is placing a capillary tube on each side of the main tube in which the biofluids flow as shown in Figure 3.12(b). This lets the epoxy flow into the side tubes and leaves the main tube untouched. The extra tubes increase the epoxy attachment area at the connection face compared to the single tube configuration, consequently, not only solving the fluid blocking problem but also enhancing the sealing performance. Finally, the whole biosensor system consisting of the fluidic VCSEL, fluidic interconnections and the bio-source reservoir is mounted on a microscope slide with epoxy or glass glue as illustrated in Figure 4.8(f) and 4.9. A multiple-layer cover

glass stripe is used to support the device, while the glass stripe itself is suspended over the microscope slide. In order to bond a Au wire to the bottom contacts of the biosensor, the cover glass strip on which the biosensor is attached must be slightly narrower than the device so that parts of the bottom Au layers can be exposed for wire bonding. Alternatively, an additional bonding pad can be formed by evaporating Au on a piece of cover glass. Then mount the device onto this glass with silver epoxy. By this means, the Au wire can directly connect to the cover glass instead of the bottom contacts.

4.2 Proton Implanted Half VCSEL Fabrication

4.2.1 Wafer Cleaving

The quarter size half VCSEL wafer is first cleaved into several small pieces as large as approximately 1.8 cm ×1.5 cm. Each piece contains about 5×6 (30) VCSEL pixels with enough handling area at the sample's edges. The wafer is cleaved simply by scoring the back side of the wafer with a diamond scribe parallel to crystal axis. Gentle pressure, as from a cotton swab, applied in the direction away from the score is sufficient to cleave the crystal along the scribe line (see Figure 4.3). [1] Successive cleaving steps produce a sample of the desired size. Once the sample is cleaved from the wafer, it is attached face down to a 22 mm×22 mm cover glass by crystal bond so that the tweezers can directly hold the glass and protect the sample from damage during handling. The sample and cover glass combination is cleaned thoroughly using acetone. Care must be taken to ensure that all of the crystal bond is removed from the perimeter of the sample, leaving the crystal bond only between the sample and the cover glass. Crystal bond is weakly soluble in photoresist and can leave residues on the sample during the lithographic steps

which is difficult to remove. [1] Once the sample has been cleaned in acetone, it is rinsed with methanol and de-ionized (DI) water, then dried by nitrogen. Now the sample is ready for processing.

4.2.2 Bottom p-Ohimc Contact Formation

The bottom ohmic contact formation is the easiest step in the VCSEL process. Since the sample is ready with the front side attached to the cover glass, it is then surface oxide etched in $NH_4OH:H_2O=1:10$ for 20 seconds followed by another 20 seconds etching in $HF:H_2O=1:10$. Then it is rinsed in DI water and dried with nitrogen. Finally the sample is loaded into the e-beam evaporator for deposition of the metal layers. The metal layers typically deposited are: 500 Å Gold-Beryllium alloy (1% Be weight percent) and 2000 Å Gold. After metal evaporation, the sample is annealed at 440° C for 45 seconds. Ohmic contact evaluation can be done if necessary.

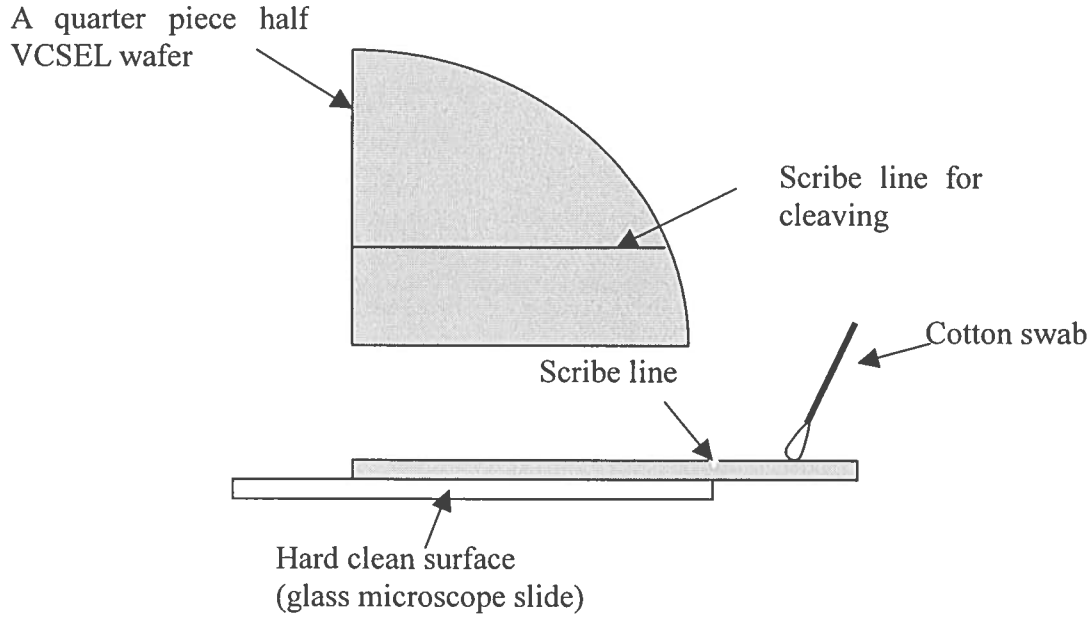

Figure 4.3 Illustration of the wafer cleaving technique. (Copied from reference [1])

4.2.3 Alignment Mark Transfer Etching

The sample is separated from the cover glass by low temperature heating to melt the crystal bond. Then the VCSEL sample is mounted on a new cover glass with the back-side attached to the glass. Since the front side is contaminated by crystal bond, a 5 minutes soak in acetone followed by acetone, methanol and DI water rinsing is sufficient to remove all contamination. Standard photolithographic procedure is executed. The sample is pre-baked at 120 °C on a hotplate for two minutes to remove water vapor, and is then placed on a photoresist spinner. Shipley PR 1818 is deposited on the sample to just cover it, and then the sample is spun at 5000 rpm for 30s. After spinning, the sample is soft-baked at 95 °C on a hotplate for two minutes to remove the resist solvent. The sample is then inserted into the mask aligner, along with the alignment mark transfer mask. The edge-beads are not obvious for PR 1818, so the edge resist removal step is neglected. The sample is exposed for 5.5s to UV light with an energy density of 15mW/cm^2 followed by developing in AZ400K:DI water=1:4 for 30 seconds. Then the sample is hard-baked at 120 °C for 2 minutes. The patterns are usually formed with a good resolution as shown by inspecting them with a high magnification microscope. Using these patterns as etching masks, the sample is etched in a fresh solution ($HCl:H_2O_2:H_2O$=1:1:9) for 1 minute with ultrasonic stirring and another 1 minute etching without stirring. Consequently, the alignment marks of about 0.5 μm deep are obtained as shown in Figure 4.4. It should be noticed that the total top semiconductor DBR mirror layers are only 0.7 μm thick. Therefore, leakage currents probably occur at the positions where the alignment marks are etched. In some cases, a Schottky contact appears to be formed at the interface.

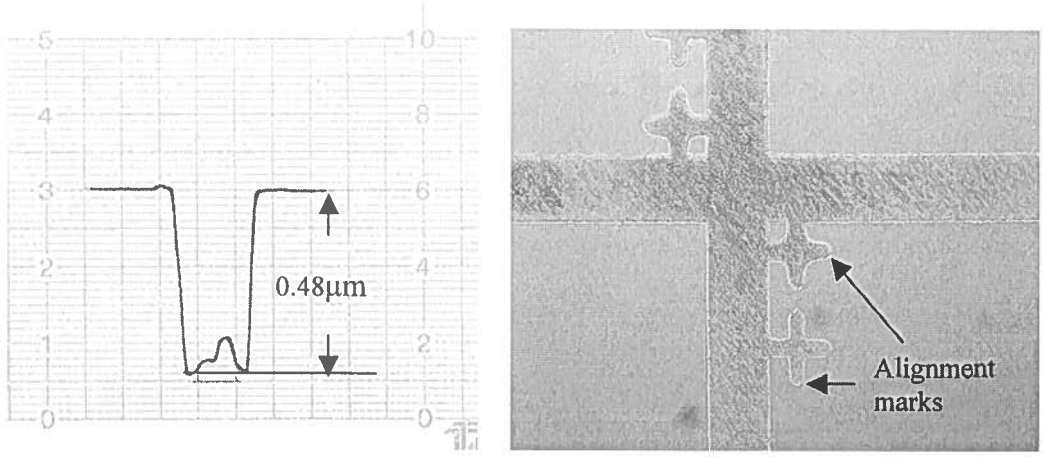

(a) (b)

Figure 4.4 Pictures showing the alignment mark transfer etching in $HCl:H_2O_2:H_2O$=1:1:9: (a) Alpha-Step measurement results (scale at 10kÅ=1μm), and (b) etched patterns.

4.2.4 Proton Implantation Mask Patterning

To block the proton ions with an average energy of 56keV, photoresist masks at least 1.3μm thick should be used as shown in Figure 3.6. Although such a value of thickness is not difficult to get, to obtain a pattern with a fairly sharp edge profile at this thickness requires more steps compared to the standard photolithographic procedure as described in Section 4.2.2. After pre-baking, photoresist AZ5214E is deposited onto the sample and spun at 2000 rpm for 30s, immediately followed by soft-baking. Next, edge-beads are removed by UV exposure for 1 minute at 15mW/cm^2 for each sample edge since 2000 rpm spinning has a very obvious edge effect. The developer is AZ400K:DI water = 1:3 and the development time is 1~2 minutes up to the thickness of edge beads. Then the sample is rinsed and dried. An additional soft bake at 95 °C for 1 minute is necessary to remove the remained water on the resist surface. Next, pattern exposure is applied on the resists. The mask should be pressed against the resist coated sample during exposure to

ensure a contact exposure mode, avoiding diffraction induced pattern distortion. [1] Small feature with a good resolution can be defined in this way. Before the resist development step, a 15 minutes chlorobenzene soak is used to sharpen the edge profile of the photoresist implantation mask since the use of chlorobenzene trends to form an overhung profile which compensates for the trapezoidal shape usually shown in a standard photolithographic process. Finally the sample is moved to the chemical hood for pattern development. This step consists of two development stages. During the first stage, the sample is placed into a glass disc containing a solution of AZ400K:DI water = 1:3 for developing for 50s. Most unwanted resist is removed. Then the sample is immediately immersed into the developer AZ400K:DI water = 1:4 for resist residues cleaning. The development time in this stage is ~ 40s. Microscope inspection determines whether the sample is clean. Develop again in AZ400K:DI water = 1:4 for a short time if necessary. Hard bake is not allowed in the implantation mask formation since it causes the resist reflow and degrades the edge profile. Consequently, a ~ 2.7 μm thick implant mask with a fairly sharp edge profile is obtained. When the masks are ready, the sample is sent to Kroko Implant Services at Tustin, CA for the proton implantation. The implant specifications are listed as

Substrate	.....AlGaAs/GaAs
Area	.....~1.8×1.5 cm^2
Ion	.....Proton
Energy	.....56 keV
Dose	.....$5x10^{14}/cm^2$
Angle	.....7 degrees off <100> axis

4.2.5 Top n-Ohmic Contact Formation

Three preparation steps should be done first before the sample is ready for metal evaporation. The first preparation removes the photoresist implantation mask. After high energy ion bombardment the photoresist becomes too hard to be removed with acetone. [1] So the sample has to be cleaned by the plasma asher in oxygen for 10 minutes. Consequently, a thick oxide layer is grown on the surface of the sample, which will increase the resistance of the top contacts. The second step defines the resist patterns with a standard photolithographic technique similar to that used for p-contacts. Photoresist AZP4400 is spun at 5000 rpm, exposed for 30s to 15 mW/cm^2 UV light, and then developed by AZ400K:DI water = 1:4 for as long as necessary. The edge-beads removal can be done if the edge effect is obvious. The third preparation step removes the thick oxide layer grown on the surface of the sample during the previous process. The etching solution is $HF:H_2O$=1:10. Finally, the sample is loaded into the e-beam evaporator. The metal layers 500Å AuGe alloy (88%:12% weight percent)/ 400 Å Ni /1000 Å Au are evaporated onto the front side of the sample in sequence. Lift-off technology [1] previously developed by Dr. Stewart A. Feld at CSU is applied for metal removal at the positions where light will come out. The resist patterns have an average thickness of ~ 2μm for spinning at 5000 rpm. They are much thicker compared to the metal layers, where the total thickness is approximately 0.2 μm. This large difference in thickness not only enhances the efficiency of metal removal but also simplifies the process, while chlorobenzene soaking is usually first used to form an overhung edge profile before lift-off in a small contrast case. [2] Figure 4.5 shows a 16 μm laser aperture before and after lift-off. After lift-off, the AuGe/ Ni /Au layers are annealed for 45s at 380 °C to

reduce contact resistance if necessary. Experimentally, a large leakage current may occur due to the fast diffusions of Au into the quantum wells during the annealing since the metal layers are only ~ 0.7 μm above the active region.

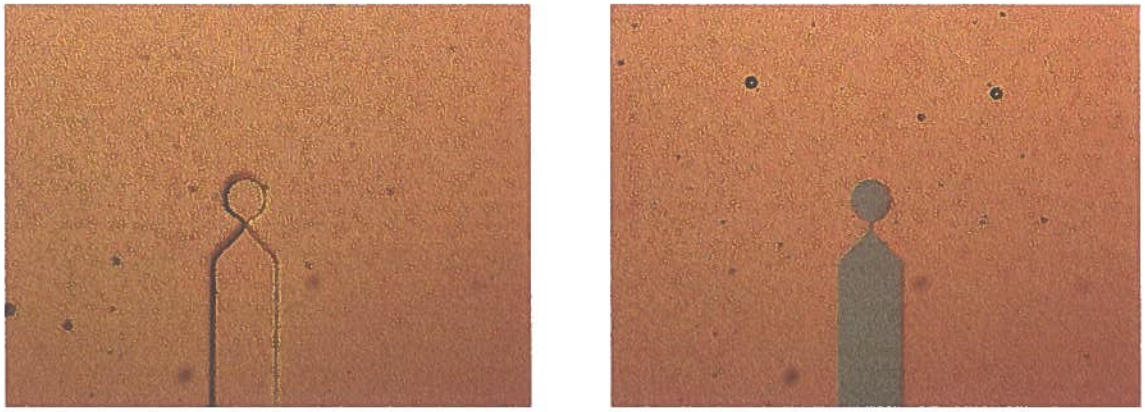

(a) (b)

Figure 4.5 Pictures showing a laser aperture of 16 μm (a) before and (b) after lift-off.

4.3 Dielectric Mirror Deposition

The dielectric mirror used for our biosensor was fabricated by Dr. Stewart A. Feld. Ten pairs of SiO_2/Si_3N_4 dielectric layers are deposited on a 22mm×22mm Pyrex cover glass. The mirror has a calculated reflectance of 99.75%. The mirror wafer is cut into pieces as large as 2.2mm×2.2mm by a diamond scriber. Since the deposited layers are uniform across the cover glass except at the edges, only the center part of the mirror is used for constructing the biosensors in the fabrication.

4.4 Fluidic Cavity Formation

In order to get more VCSEL pixels with uniform spacers, the sample is first scribed along pixel boundaries. Since the sample is attached to a cover glass, it is not really broken. As

a result, the photoresist spacers are very flat in most places when SJR5440 is used and spun at 4400 rpm for 30s. Standard photolithographic process is used. After 3 min exposure at 15 mW/cm^2 and ~ 3 min development in the developer 453, an average thickness of 5.2 μm is achieved for spacers. Then melt the crystal bond at 90 °C to remove the sample from the cover glass. Break the sample into pixels along the scribed lines and then attach each pixel to separate pieces of the cover glass. Do not contaminate the front side of the VCSEL with the crystal bond during attachment. Monolithically bonding technology is utilized in this step. Firstly, the VCSEL pixel is cleaned with DI water then dried with nitrogen blowing. Extreme care should be used to avoid using acetone since it dissolves the photoresist spacers. The 2.2mm×2.2mm dielectric mirror piece is cleaned by acetone, methanol and DI water and then dried with nitrogen. As shown in Figure 4.6, a cylindrical magnet is placed underneath the cover glass. Then put the small piece of dielectric mirror onto the spacers using tweezers. On the glass substrate, place a piece of cylindrical shaped iron. The mirror piece is contacted against the spacers because of presence of the magnetic force. Under the microscope, the alignment between the mirror and VCSEL is easily done with tweezers. Once the alignment is finished, this combined structure is carefully moved to a 90 °C hotplate, ensuring this moving procedure doesn't cause any movement of device parts. Then heat it as long as necessary (at least 40 min) to finish photoresist bonding. Make sure a piece of microscope slide has already been placed on the hotplate and the combined structure is put on this thick glass. The reason for this preparation is that the magnet can be strongly attracted by the metal panel of the hotplate, causing the spacer bond to break at the time the sample is taken away the hotplate. Adding a thick glass underneath the magnet greatly weakens this

attraction. Figure 4.7 shows a uniform thickness and well sealed fluidic cavity fabricated with this "magnetic bonding" technology.

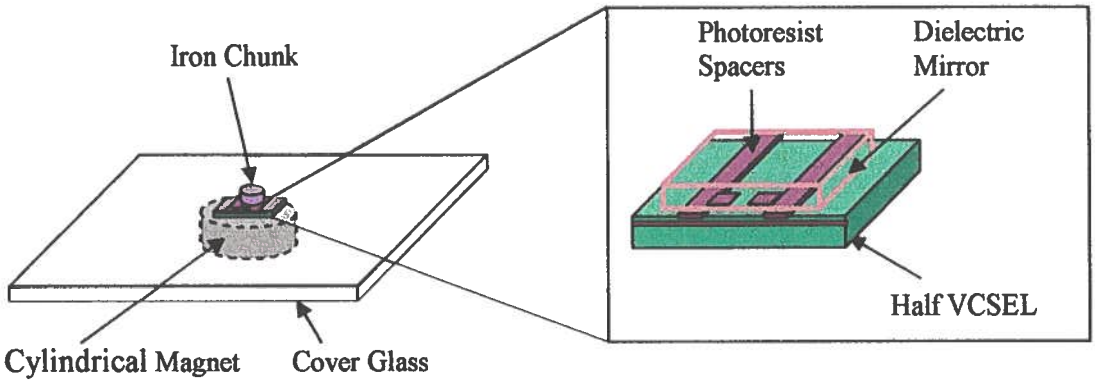

Figure 4.6 "Magnetic bonding" configuration. A chunk of cylindrical magnet is placed underneath the cover glass and a piece of iron chunk is put on the top of the mirror. The magnet will attract the iron and make a uniform and well-sealed fluid cavity possible.

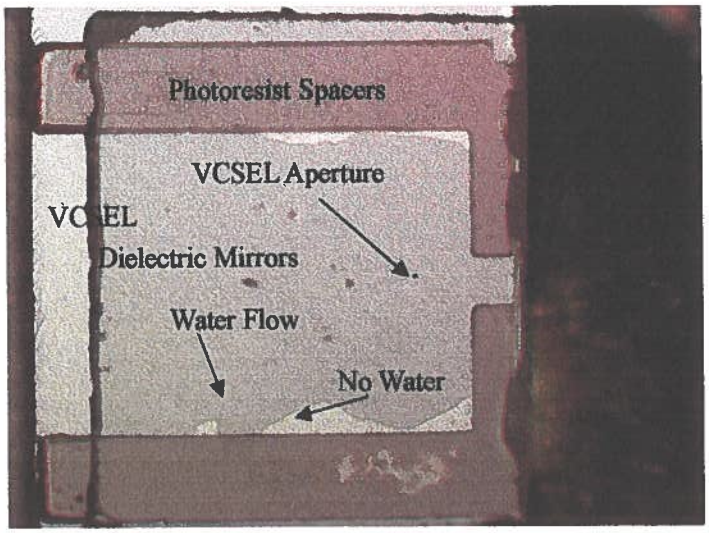

Figure 4.7 A uniform and well-sealed fluidic cavity is formed with a "magnetic bonding" technology. Water is fed into the cavity. The symmetric water distribution proves the uniformity of the cavity thickness and inexistence of water at the bonding interface and outside of cavity confirms that cavity is well-sealed.

4.5 Biosensor System Assembly

Fluidic interconnections are required to connect the source reservoir, fluidic cavity and drain reservoir together. Capillary tubes are utilized for this purpose. Size matching between tubes and the fluidic cavity and the assembly schematics are displayed in Figure 3.12. In order to avoid electrical short paths between bottom and top contacts of the VCSEL, additional device passivation process steps are necessary. All the materials used for the biosensor system assembly are given in Table 4.1 and the general process flow is illustrated in Figure 4.8.

Table 4.1 Materials used in the biosensor system assembly

Materials	Characteristics	Applications
Capillary Tube	Main Tube: ~ 42 mm long Side Tubes: ~ 20 mm long	Fluidic interconnections & epoxy reservoirs
Pyrex Cover Glass I	Thickness: ~ 229 μm	Sample handling
Pyrex Cover Glass II	Thickness: ~ 127 μm	Thickness matching
Microscope Slide	Length: ~ 75mm	Biosensor system substrate
Glass Glue	Instant adhesion	
Nonconductive Epoxy	Adhesive, nonconductive, viscous and deformable	Interconnections attachment & system sealing
Silver Epoxy	Adhesive, conductive, viscous and deformable	Device attachment
Photoresist SJR5440	Viscous and nonconductive	VCSEL edge passivation

The VCSEL is first stuck to a piece of cover glass I using crystal bond. Then photoresist is decanted from a pipet to the cover glass (see Figure 4.8 (a)). The drops of photoresist flow along the glass surface and surround the edges of the VCSEL. Once all edges are covered by the resist due to surface tension, the VCSEL is transferred to a 95 °C hotplate and heated for 30s to partially evaporate the solvents. Spin it at 1000 rpm for 1 minute then gradually elevate the speed to 8000 rpm. Existence of solvents in the resist

guarantees the resist can change thickness during spinning. Spinning at a low speed ensures that no resist strips away from the edges and elevated spinning achieves a uniform resist layer. This process forms a uniform overall passivation layer (see Figure 4.8 (b)) around the VCSEL edges, which protects the device from the electrical short caused by the presence of biofluids. Next the VCSEL with the passivation layer is disattached from the cover glass I, and mounted on a glass bar consisting of three layers of the cover glass II, which is used for weight supporting (see Figure 4.8 (c)). Cover glass II is also used to raise the fluidic cavity to the center of the capillary tube (see Figure 3.12). Silver epoxy is utilized. Make sure the crystal bond on the backside of the device is removed by acetone from a cotton swab before mounting to the bar. Since the device is small, extreme care should be taken not to damage the passivation layer around the edges. Then, three capillary tubes are glued onto a piece of cover glass II side by side using nonconductive epoxy (see Figure 4.8 (d)). Next, nonconductive epoxy is placed at the entrances of the side capillary tubes. Because of capillary actions, the epoxy is drawn into the tubes, where the epoxy reservoirs are formed (see Figures 4.8(e) and 3.12(b)). At the same time, the edge of the cover glass II toward to the VCSEL fluidic cavity is also covered by nonconductive epoxy, which is not only used for the connection but also to prevent the biofluid leaking from the bottom. Finally the capillary tubes are jointed to the biosensor. The reservoirs provide sufficient epoxy for the seal and attachment. This assembly is then glued to a microscope slide using glass glue (see Figure 4.8(f)). The final biosensor system including a sensor device, interconnections and a biofluid source reservoir is shown in the photography of Figure 4.9.

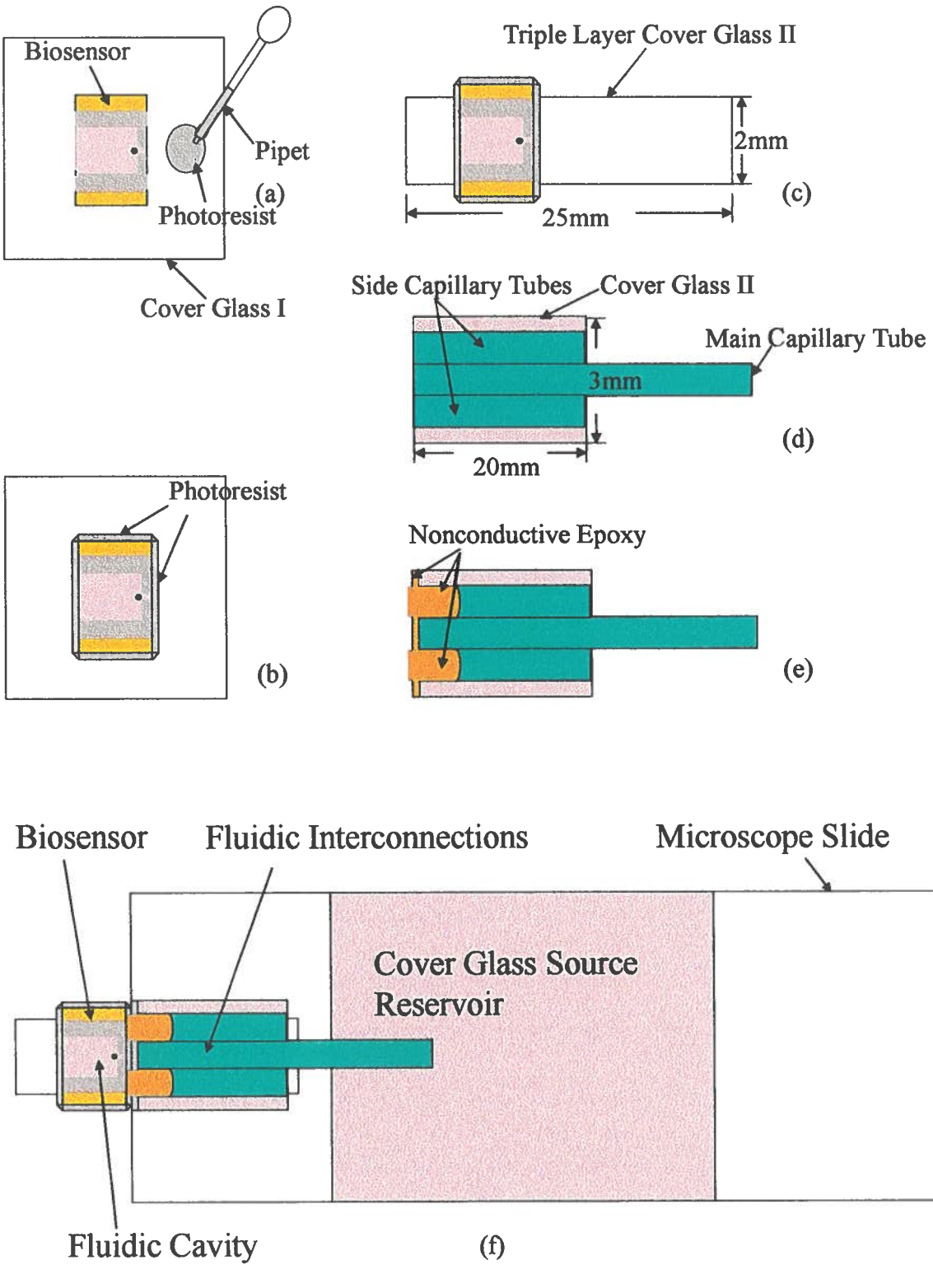

Figure 4.8 General process flow for the biosensor system assembly: (a) photoresist distribution, (b) edge photoresist passivation, (c) biosensor mount, (d) fluidic interconnections attachment, (e) epoxy distribution (f) system assembly.

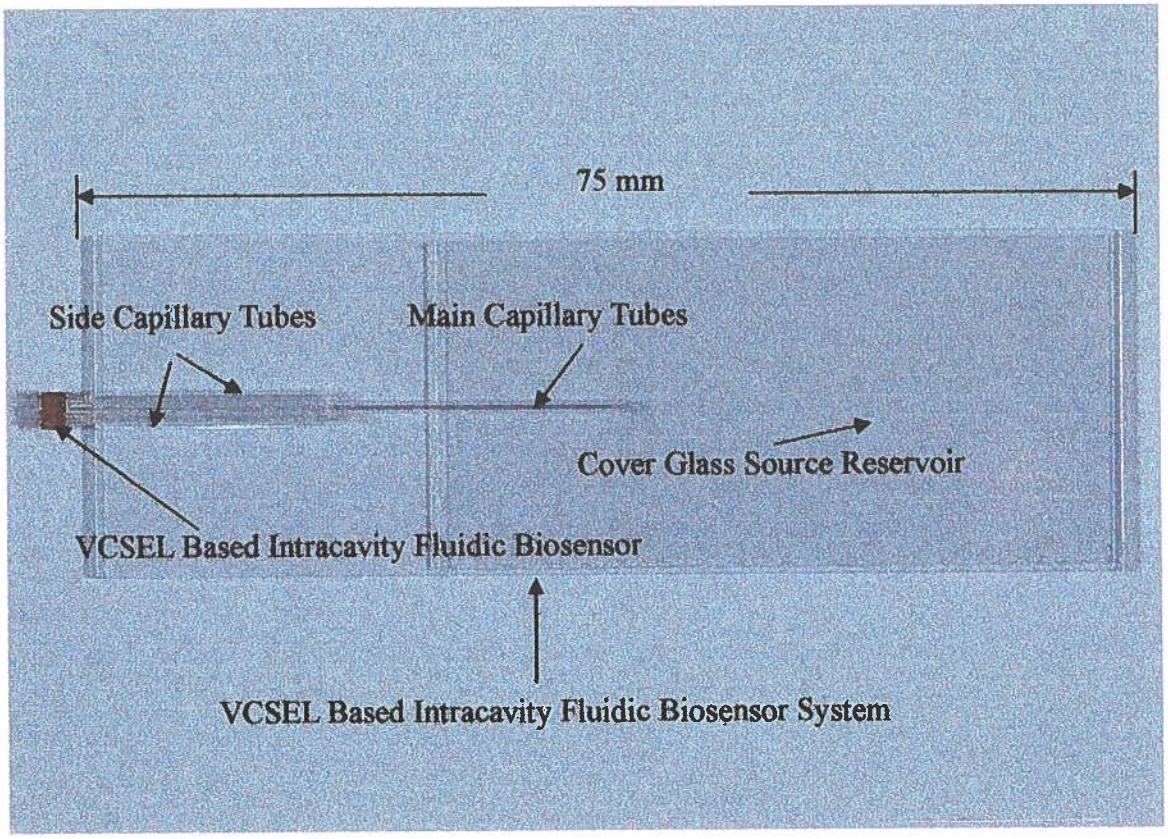

Figure 4.9 Top view of an electrically pumped VCSEL based intracavity fluidic biosensor system without the drain reservoir and the corresponding fluidic interconnections.

4.6 Summary of Chapter 4

The steps required to fabricate an electrically pumped VCSEL based intracavity fluidic biosensor are presented in this chapter. The process includes four major parts: half VCSEL fabrication, dielectric mirror deposition, fluidic cavity formation and system assembly. The VCSEL fabrication is time-consuming since there are many challenges. Many issues occur in the practical fabrication, such as the VCSEL contact failure, large leakage current, no lasing, and poorly sealing. Great efforts have been made to solve these problems in order to achieve a good performance biosensor. New fabrication technologies such as edge extension, "magnetic bonding" and epoxy reservoir tubes were developed.

References:

[1]. Stewart A. Feld, "Ph.D. Dissertation", *Colorado State University* (1996).

[2]. Ahmad Nasser Al-Omari, "MS Thesis", *Colorado State University* (2002).

[3]. Kevin Roberts, *et al.*, "The fabrication of an array of microcavities utilizing SU-8 photoresist as an alternative 'LIGA' technology", *University/Government/Industry Microelectronics Symposium, Proceedings of the Thirteenth Biennial,* pp.139–141 (1999).

[4]. Todd R. Christenson and Dave T. Schmale, "A batch wafer scale LIGA assembly and packaging technique via diffusion bonding", *Micro Electro Mechanical Systems, MEMS '99. Twelfth IEEE International Conference on*, pp. 476 –481(1999).

CHAPTER 5

TESTING AND CHARACTERIZATION OF ELECTRICALLY PUMPED VCSEL BASED INTRACAVITY FLUIDIC BIOSENSOR

5.1 Overview

In this chapter, testing and characterization of the electrically pumped VCSEL based intracavity fluidic biosensor are discussed. The half VCSEL and biosensor performance were evaluated separately. The results and the corresponding analysis are presented.

5.2 General Measurement Setups

Characterization of the electrically pumped VCSEL based intracavity fluidic biosensor requires measurements of following:

1) *V-I* curve in order to evaluate the ohmic contacts and observe the diode characteristics,
2) *L-I* curve in order to measure the output power of the VCSEL structure and the threshold current (assuming the structure lases),
3) Emission spectrum to determine if the structure is lasing, its modes and the effects of water in the cavity.

These measurements require two experiment setups. They are shown in the photographs of Figure 5.1. The *V-I* & *L-I* curves were obtained with a HP4145A semiconductor parameter analyzer (SPA) as shown in Figure 5.1 (a). The device to be tested was placed on a MICROMANIPULATOR probe station with a constant temperature chuck. A SPA provided the required voltage or current for the measurements and the corresponding results were displayed on the monitor of the SPA. To measure the output optical power of the VCSEL, a 10 mm×10 mm silicon photodiode with responsivity of ~0.6A/W at a wavelength of 850 nm was used. [1, 2] Since our biosensor senses the bioanalyte via wavelength shifting, a computer controlled Filmetrics F20 single-spot measurement system with the capability to detect a small wavelength change was used as shown in Figure 5.1 (b). An optical fiber was used to collect the optical signals from the output of the VCSEL to the Filmetrics F20 when an emission spectrum was measured.

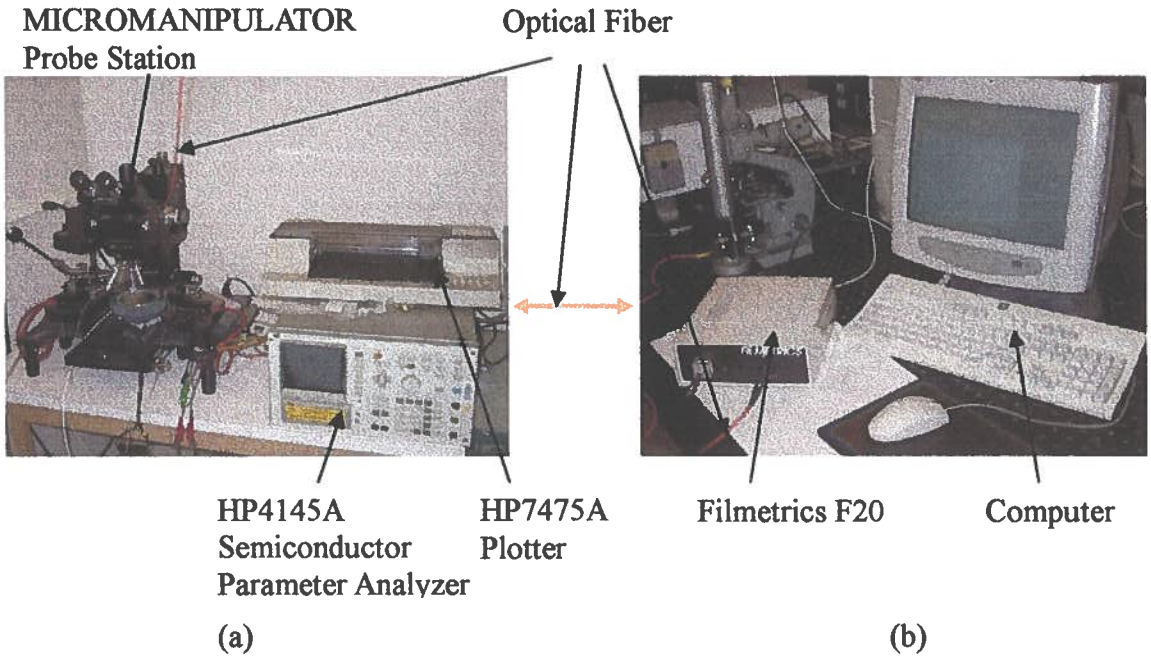

Figure 5.1 Photos showing the general overview of the measurement setups: (a) HP 4145A semiconductor parameter analyzer together with MICROMANIPULATOR probe station, (b) Filmetrics F20 controlled by a computer.

5.3 Half VCSEL Characteristics

5.3.1 Test Setup

The equipment for the half VCSEL test is shown in Figure 5.1 (a), consisting of a probe station, a HP 4145A SPA and a HP 7475A plotter. Channels 1 and 2 from the SPA were connected to VCSEL pads to provide a stimulus current swept from 0 to 30 mA. The compliance voltage was set to 5 volts. Channels 3 and 4 were placed onto the photodiode to provide a 10 volts DC reverse bias, thus the output optical power of the VCSEL could be obtained by measuring the current of the photodiode which was well-aligned on the top of the VCSEL to ensure that most of the photons from the VCSEL were incident on the photodiode surface. [2] The half VCSEL voltage and photocurrent were plotted as a function of the stimulus current, displayed on the monitor of the SPA. Care was taken in order to insure that the probe did not penetrate through the top contact layers during the measurement.

5.3.2 Influence of n-Ohmic Contact Annealing and Process Recipe on *V-I* Characteristics

All test samples have the same p-ohmic contacts at the backside. It is found that the *V-I* characteristics are degraded after annealing the top AuGe/Ni/Au contact layers, as shown in Figure 5.2 for before and after annealing. Without annealing (Figure 5.2 (a)), the "turn on" voltage at $I_1 = 3$ mA is around 1.3 volts and the dynamic resistance is about 11 ohms for a half VCSEL with an aperture size of 16 μm, which reflects good electrical performance. Annealing at a temperature above 400°C for 30 seconds induces a large junction leakage current (shown in Figure 5.2 (d)), probably due to the fast diffusion of Au through the ~ 0.7 μm mirror layers into the quantum wells. Meanwhile, both morphography and color of the top contact metals change greatly, leading to a rough

surface (shown in Figure 5.3). Another possible cause of the leakage is through the etched alignment marks. Since ~ 0.5 μm deep n-mirror layers are etched away during this process step, the possibility of the Au diffusion into the active region becomes even greater. In some cases, a Schottky barrier appears to be formed at the interface and the "turn on" voltage is pinned at ~ 0.5 volts at $I_1 = 3$ mA as shown in Figure 5.2 (c). The rate of the ohmic contact failure arising from both Schottky barrier and leakage current is as high as 70% in the VCSEL samples fabricated with Recipe I described in Appendix D, even though the annealing temperature is decreased to 380 °C. On the other hand, *V-I* characteristics of VCSELs fabricated with Recipe II annealing at 380 °C are much better (shown in Figure 5.2 (b)) with a contact failure rate of ~ 20% and close to zero without annealing (shown in Figure 5.2 (a)). Obviously, in our case, VCSELs without contact annealing have better electrical performance. Recipe II without n-ohmic contact annealing is preferred and was used for sample runs 4 and 5.

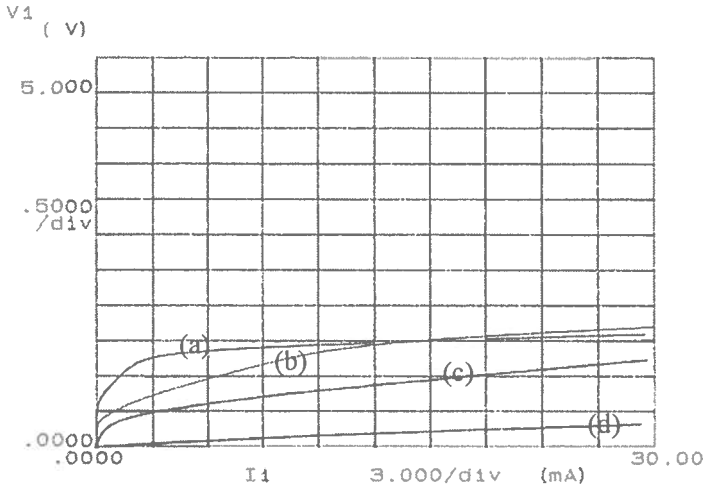

Figure 5.2 Plots showing the influence of n-ohmic contact annealing and process recipe on *V-I* characteristics: (a) ohmic *V-I* curve using Recipe II without annealing, (b) degraded *V-I* curve using Recipe II with annealing at 380 °C for 45s, (c) Schottky *V-I* curve using Recipe I without annealing, (d) leakage *V-I* curve using Recipe I with annealing at 440 °C for 30s. All samples have the same p-ohmic contacts at the backside.

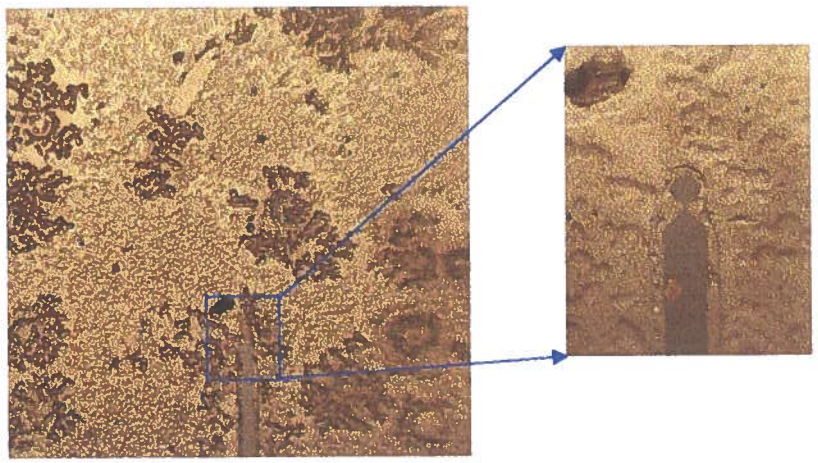

Figure 5.3 Optical photograph showing the surface of the n-ohmic contact after annealing at 440 ° C for 30s.

5.3.3 Influence of Dielectric Mirror on *L-I* Characteristics

It is found that the light power transmitted through the external dielectric mirror becomes weaker than that from the half VCSEL only, seen from Figure 5.4, where I_4 is the photocurrent generated by the output light. It shouldn't happen in the laser mode, just the LED mode.

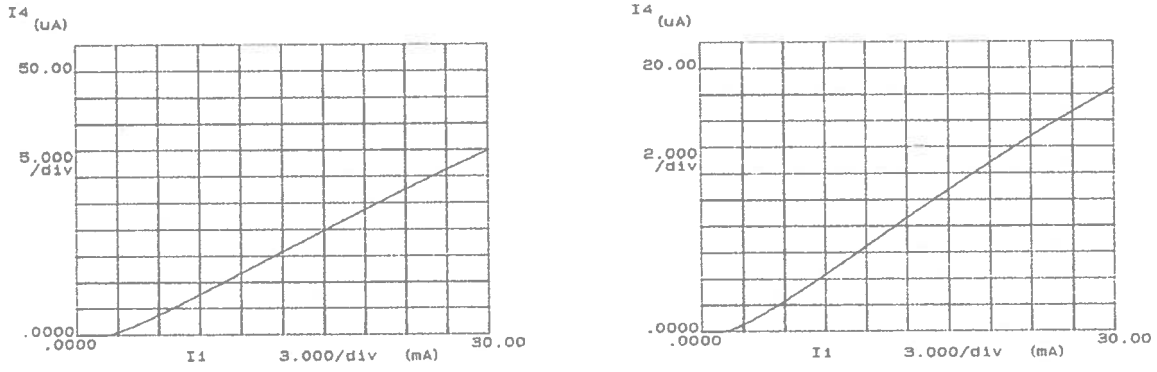

(a) (b)

Figure 5.4 Plots showing the influence of dielectric mirror on *L-I* characteristics: (a) *L-I* curve without the dielectric mirror, (b) *L-I* curve with the dielectric mirror. (From measured data of VCSEL chip #4-11)

The calculated values of the emission power of the half VCSEL with and without the external dielectric mirror for a stimulus current of $I_1 = 30\,\text{mA}$ are 31 μW and 58 μW, respectively, according to measurement plots shown in Figure 5.4. The equation for calculation is given by

$$P_0 = \frac{I_4}{\Re}, \tag{5.1}$$

where $\Re = 0.6$ A/W, responsivity of the silicon photodiode. [1, 2] Since the power is much lower than that of a commercial VCSEL chip, it is supposed that our VCSEL does not lase properly but performs like an LED. The power of a half VCSEL with an external dielectric mirror is almost half of that without a mirror.

5.3.4 Typical *V-I* and *L-I* Characteristics of a Half VCSEL with and without the Dielectric Mirror

The measurement results of the VCSEL chip #5-5 fabricated with Recipe II are shown in Figure 5.5. The electrical performance and output power are concluded on Table 5.1.

Table 5.1 Electrical and optical performance of the VCSEL chip #5-5

Metal aperture	14 μm
Implanted confinement aperture	22 μm
"Turn on" voltage at $I_1 = 3\,\text{mA}$	1.7 V
Dynamic resistance	22 Ω
Output optical power without dielectric mirror at $I_1 = 30\,\text{mA}$	66.7 μW
Output optical power with dielectric mirror at $I_1 = 30\,\text{mA}$	45.8 μW
Apparent current without dielectric mirror	2 mA
Apparent current with dielectric mirror	1.5 mA

It appears that the dielectric mirror enhances the radiation process since the apparent current for the VCSEL with the mirror becomes lower and the chip tends to lase but seems much more like a LED considering the spectrum shown later and the low output power. Red light can be seen emitted from the half VCSEL chip either with or without the external dielectric mirror. As shown later, most of the optical power is in the visible red region.

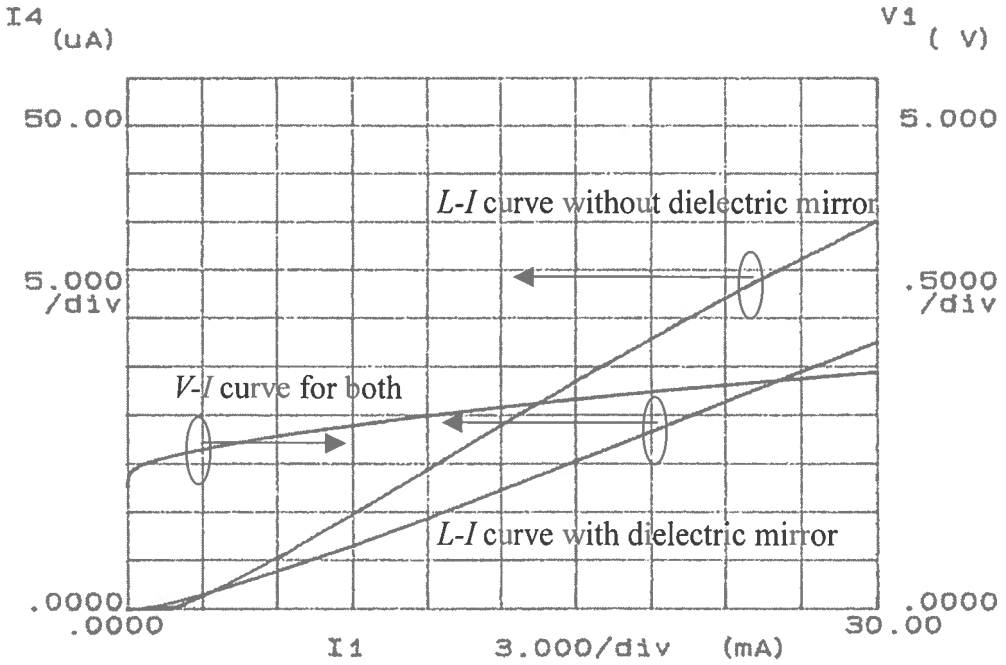

Figure 5.5 Plots showing typical *V-I* and *L-I* characteristics of a half VCSEL with and without the dielectric mirror. (From measured data of VCSEL #5-5)

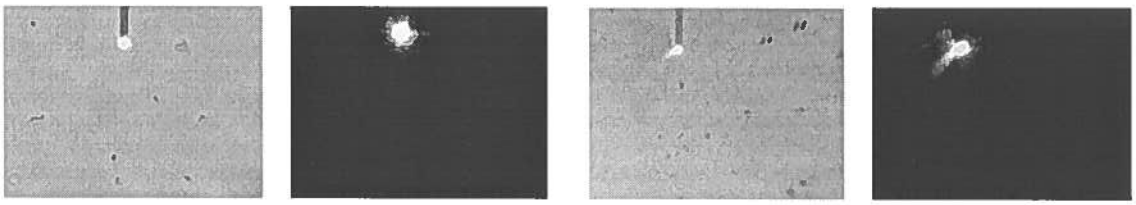

(a) (b) (c) (d)

Figure 5.6 CCD camera captured pictures showing light emitted from the half VCSEL chip #5-5: (a) light with a bright background and (b) with a dark background for the chip without dielectric mirror, (c) light at a bright background and (d) with a dark background for the chip with dielectric mirror.

A CCD camera has captured the light from the device of Figure 5.5 as illustrated in Figure 5.6, with and without the dielectric mirror. The unsymmetric beam shape of Figure (c) and (d) could arise from mirror tilting. The alpha-step measured results indicate that the two arms of the photoresist spacer are not in the same level. Pressing the mirror against the spacer is capable of slightly adjusting the cavity thickness after mirror bonding, which may result in wavelength shifting.

5.4 Biosensor Characteristics

5.4.1 Fluid Transport Inspection and Cavity Feeding Speed Measurement

Experimentally, D-I water is fed into the fluidic cavity of our biosensor by capillary action. The measured filling time is less than 1 second, which is very close to the value calculated from Sandia's analysis. [3] It is also found that water can evaporate quickly if the source reservoir is disconnected from the fluidic cavity. The evaporation is illustrated in the sequence of photos of Figure 5.7. Water begins evaporating at the entrance of the fluidic cavity.

5.4.2 Experimental Emission Spectrum Analysis

5.4.2.1 Test Setup

The equipment for the complete biosensor test is shown in Figure 5.1 (a)(b), consisting of a Filmetrics F20 and an optical fiber, besides all the instruments used in the half VCSEL test. Channels 1 and 2 from the SPA were connected to VCSEL pads. Considering the low power of the VCSEL, the drive current I_1 was set to 50 mA so that sufficient optical signals could be detected by the Filmetrics F20 considering the loss associated with the

optical fiber. The compliance voltage was set to 5 volts. Then static spectra of the microcavity emission were recorded.

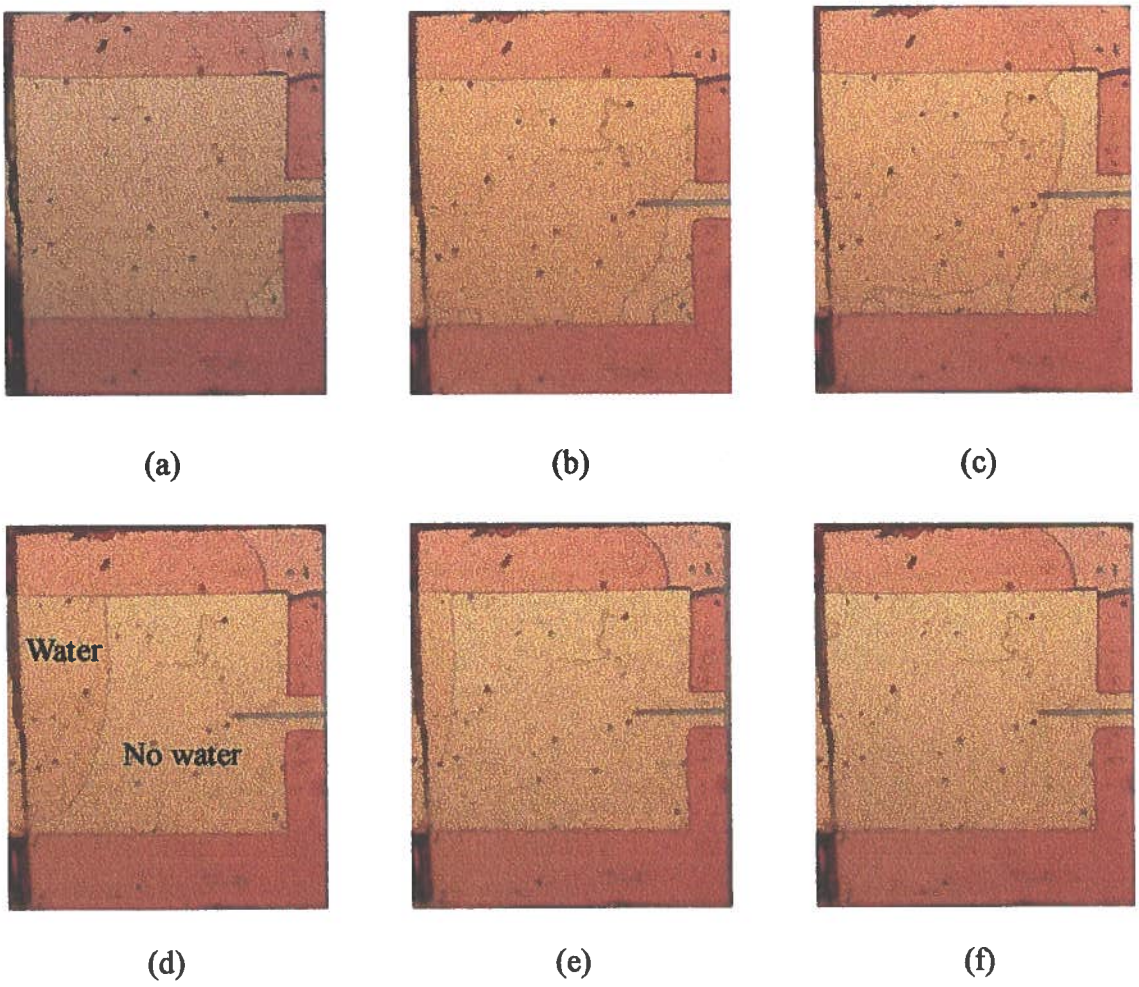

Figure 5.7 Pictures showing that water evaporates from the fluidic cavity: (a) fluidic cavity filled with D-I water, and (b)(c)(d)(e)(f) water evaporation. Be aware that the cavity at the left top corner is poorly sealed.

5.4.2.2 Effect of Fluidic Cavity Index Changing on Longitudinal Modes

The emission spectrum for the half VCSEL without the external dielectric mirror is shown in Figure 5.8. And the emission spectra for the biosensor without and with DI water in the fluidic cavity are shown in Figure 5.9. For all conditions, the dominant

optical power is in the 710 nm to 760 nm range. This appears to result form the carrier recombination and light generation in the $Al_{0.2}Ga_{0.8}As$ barrier layers of the active region. The bandgap of this composition is expected to yield emission at a wavelength of around 741 nm. Light generating in the top semiconductor DBR mirror is also possible. The VCSEL quantum wells were designed to produce laser at ~850 nm and a small peak at 844.3 nm appears when no water is in the cavity. The addition of water shifts this peak by 3.2 nm to 841.1 nm. Obviously, the light intensity becomes lower with water inside the fluidic cavity, due to the optical absorption by water. It may be also caused by the misalignment between optical fiber and output light beam. Similar effects would occur with the bioanalytes. [4] The emission in the biosensor VCSEL is complex and understanding the measured emission spectra will require further analysis.

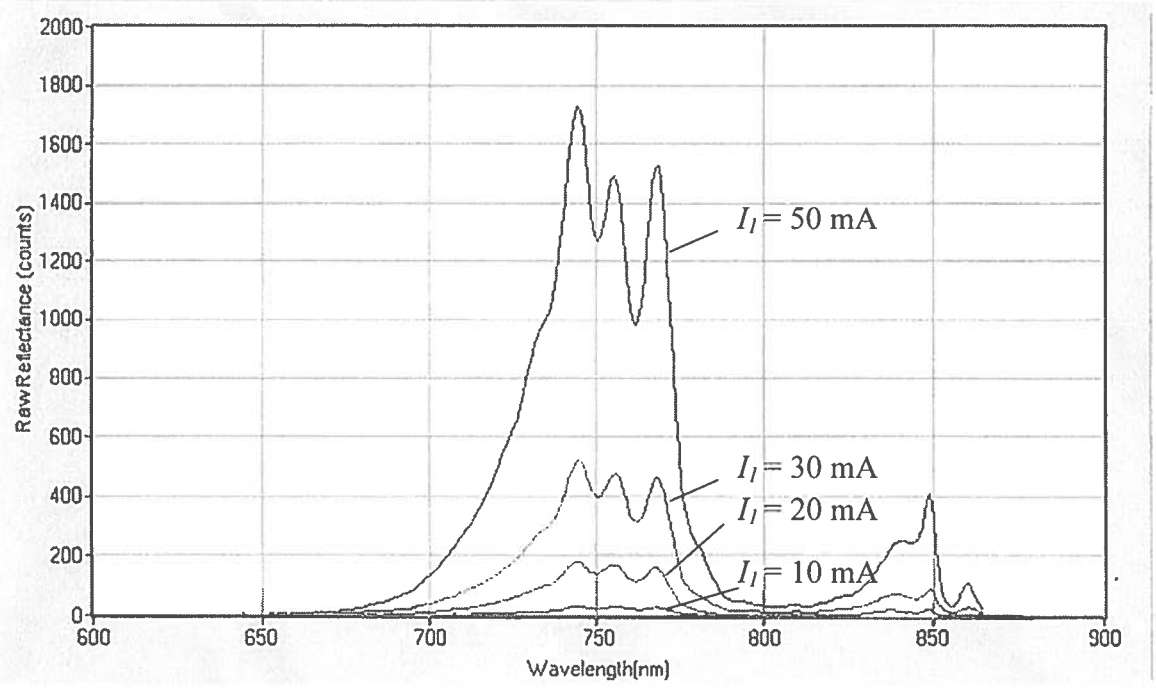

Figure 5.8 Static emission spectrum for the half VCSEL without the external dielectric mirror. The dominant optical power is in the 710 nm to 760 nm range. This appears to result form the carrier recombination and light generation in the $Al_{0.2}Ga_{0.8}As$ barrier layers of the active region. Light generating in the top semiconductor DBR mirror is also possible.

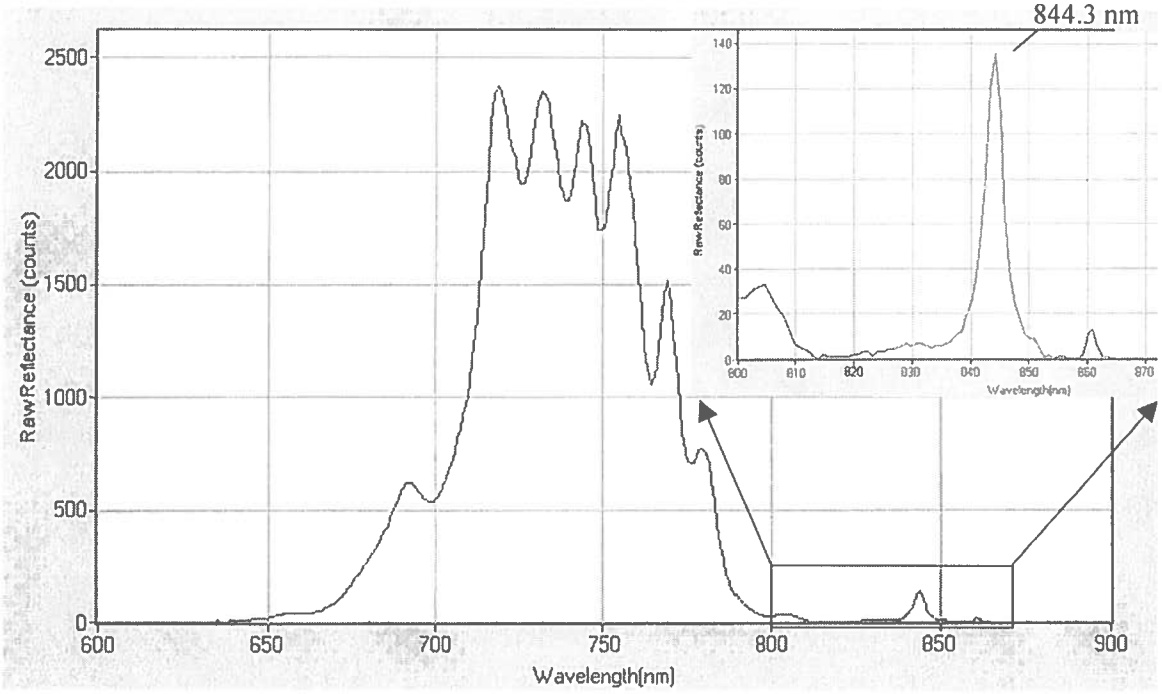

(a)

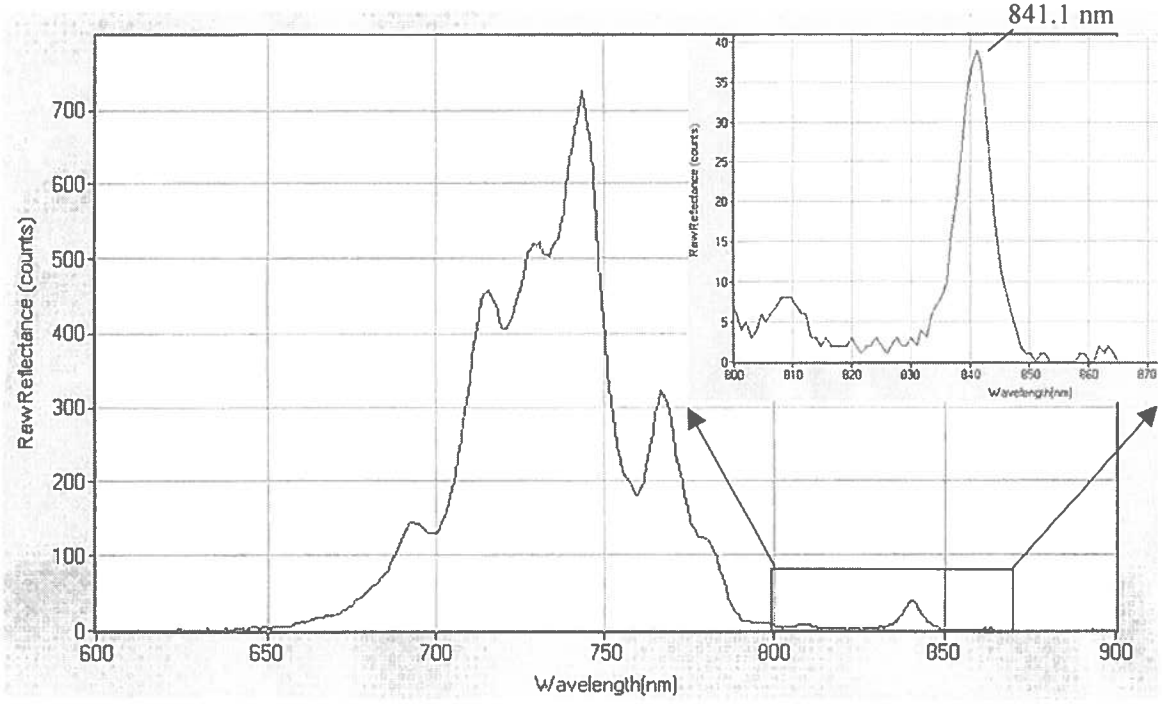

(b)

Figure 5.9 Static emission spectra for the electrically pumped VCSEL based intracavity fluidic biosensor: (a) spectrum for the empty cavity biosensor with air (n=1) inside the fluidic cavity, (b) spectrum for the biosensor with DI water (n=1.33) inside the fluidic cavity. Wavelength shifting is 3.2 nm.

5.5 Summary of Chapter 5

Testing and characterization of the electrically pumped VCSEL based intracavity fluidic biosensor are discussed in this chapter. The influence of n-ohmic contact annealing and process recipe on *V-I* curve as well as the influence of the dielectric mirror on *L-I* curve are evaluated in the half VCSEL test. It is concluded that the half VCSELs fabricated with Recipe II without n-ohmic contact annealing (i.e., sample runs 4 and 5) have good electrical performance. Table 5.2 summarizes the results. The external dielectric mirror bonded on the half VCSEL reduces the output optical power of the device which is displayed in Figure 5.4. Experimentally, the dominant mode in the infrared region is shifted 3.2 nm when DI water is capillarily fed into the empty fluidic cavity. Filling the cavity requires time less than 1 second. Further study and analysis are required to explain the emission spectra.

Table 5.2 Compared results of the VCSEL performance with different fabrications

Items	Recipe I		Recipe II	
	w/ annealing	w/o annealing	w/ annealing	w/o annealing
V-I performance	Schottky contact, or large junction leakage	Ohmic/ Schottky contact, or leakage	Degraded *V-I*, or leakage	Ohmic contact
L-I performance	Light, or no light	Light, or no light	Light,or no light	Light
Yield*	~ 5%	~ 35%	~ 85%	100%
Possible failure reasons	Alignment mark etching, or diffusion of Au into the quantum wells		Diffusion of Au into the quantum wells	

* Yield is defined as the ratio of VCSELs capable of generating light to the total VCSELs in the sample.

References:

[1]. "Thorlabs data sheet for item # FDS1010", *http://www.thorlabs.com*

[2]. Ahmad Nasser Al-Omari, "MS Thesis", *Colorado State University* (2002)

[3]. P.L. Gourley and A. E. McDonald, "Semiconductor microlasers with intracavity microfluidics for biomedical application", *Proc. SPIE* 2978, pp.186-196 (1997).

[4]. "Optical properties spectra", *http://omlc.ogi.edu/spectra/index.html*

CHAPTER 6

CONCLUSIONS AND SUGGESTIONS FOR FUTURE WORK

This chapter summarizes the achievements of the research work of this thesis. The conclusions and suggestions for the future work are given based on these achievements.

6.1 Accomplishments

The goal of this thesis research is to develop a first generation electrically pumped VCSEL based intracavity fluidic biosensor used for biological or chemical sample analysis by introducing an analytic biofluid into the high finesse cavity of VCSEL. The accomplishments include:

1) Analyzed the issues associated with the biosensor design and fabrication.
2) Designed a prototype structure and mask plates for the biosensor.
3) Simulated the wavelength shift as a function of the refractive index of bioagents in the VCSEL fluidic cavity.
4) Developed the fabrication technology for the biosensor.
5) Successfully bonded an external dielectric mirror to a half VCSEL chip with photoresist spacers.
6) Determined the critical processing steps which influence the device yield.

7) Detected and demonstrated the wavelength shift when DI water is capillarily fed into the fluidic cavity of the biosensor.

6.2 Conclusions

1) Alignment mark etching and n-ohmic contact annealing greatly degrade the half VCSEL *V-I* characteristics, thus influencing the *L-I* curve. VCSELs fabricated with Recipe II without n-ohmic contact annealing have low resistance, turn on voltage and leakage.
2) The half VCSEL performs like an LED and the output optical power is low.
3) Bonding an external dielectric mirror to a half VCSEL chip with photoresist spacers is viable. A well sealed and uniformly thick fluidic cavity can be obtained by heating the structure at 90 °C with external force applied on the substrate.
4) The external dielectric mirror decreases the output optical power of the VCSEL.
5) DI water can be capillarily fed into the ~ 5 μm thick VCSEL fluidic cavity and the filling time is less than 1 second.
6) DI water evaporates quickly from the fluidic cavity if the source reservoir is disconnected from the VCSEL.
7) The dominant optical power is in the range of 710 nm to 760 nm which corresponds to the barrier layer bandgap energy. A small peak at ~ 840 nm corresponding to the quantum well energy can be detected in the infrared

region for a complete biosensor. The reason why the dominant power is in the visible red region is not clear and requires further study.

8) A 3.2 nm mode shift of the ~840 nm peak occurs when DI water is injected into the empty fluidic cavity. This indicates that the biosensor does or can be made to function correctly.
9) The emission spectra of the biosensor are complex and further study and analysis are required to explain the spectra.
10) A compact size, easily manufactured and simply used electrically pumped VCSEL based intracavity fluidic biosensor was built and functionally demonstrated in this thesis research.

6.3 Suggestions for future work

1) Further study and analysis of the emission spectra of the first generation biosensor should be done first.
2) Edge emission spectra of the first generation biosensor could be investigated to find the emission wavelength of the half VCSELs.
3) Optical pumping could be used to find the emission wavelength of the half VCSELs.
4) Fluid containing bioagents should be applied to the biosensor to demonstrate the functionality of the device.
5) Database of the cell signature spectra should be built.
6) Design and fabricate a high power half VCSEL wafer.
7) Investigate other current confinement technologies in order to improve the

half VCSEL performance.

8) New ohmic contact technology should be developed to improve device performance since the unannealed metals may not be stable.
9) Electrical interconnections instead of large Au pads could be used to decrease the size of the biosensor and the possibility of the current leakage.
10) Design and integrate all components of a biosensor system, i.e., fluidic VCSEL chip, fluidic interconnections, fluid source and drain, in one chip.
11) Hybridly bond the biosensor to CMOS or MESFET circuits to totally realize systems on a chip.

APPENDIX A

BIOSENSOR CLASSIFICATIONS

Table A.1 Biosensor classification according to the bioreceptor type [1]

Category	Sensing Mechanism Description and Advantages	References
Antibodies	This type of biosensor (generally called immunosensor) works via an antigen-antibody reaction to generate a transducer signal and has an advantage of high selectivity.	[2]
Enzymes	Enzymes act as biological catalysts. In these sensors, the presence of analyte is typically detected by measuring the formation of a product of a reaction with the enzyme. Since the detectable signals are amplified by a catalytic reaction, the enzyme based biosensor allows for much lower limits of detection than the immunosensor.	[3]
Nucleic Acids	This kind of biosensor is often referred to a genosensor, since the complementarity of adenine: thymine (A:T) and cytosine: guanosine (C:G) pairing in DNA forms the basis for the specificity of bio-recognition in this device.	[4]
Cellular Structures Cells	These bioreceptors are either based on biorecognition by an entire cell/microorganism or a specific cellular component that is capable of specific binding to certain species. The advantage is low limits of detection due to signal amplification.	[5]
Biomimetic Receptors	A receptor fabricated and designed to mimic a bioreceptor by means of genetical engineering, artificial membrane fabrication and molecular imprinting is defined as a biomimetic receptor. All these technologies provide a large variety of binding sites for biosensors.	[6]
No Bioreceptors	This kind of biosensor only contains a transducer part and often depends on optical methods to sense target analyte. Without a complex bio-recognition part, the device becomes simply fabricated, cheap and reusable as well as bio-sensitive.	[7-10]

Table A.2 Biosensors classification according to the transducer type [1]

Category	Transducing Mechanism Description	References
Amperometric	Amperometric devices detect changes in current at a constant potential. Measures current generated by electron exchange between a biological system and an electrode	
Conductive	Conductimetric devices detect changes in conductivity between two electrodes.	
Capacitive	When the biorecognition reaction causes a change in the dielectric constant of the medium in the vicinity of the bioreceptor, capacitance measurement method can be used as a transducer.	
Piezoelectric	These devices detect changes in mass.	
Potentiometric	Electrodes detect changes in potential at constant current (usually zero).	
Thermal	These devices measure changes in temperature.	
Optical can be subdivided into two modes according to the optical configuration.	Optical biosensors correlate changes in concentration, mass, or number of molecules, even refractive index of cells to direct changes in the characteristics of light. For this method to work, one of the reactants or products of the biorecognition reaction has to link to colorimetric, fluorescent or luminescent indicator molecules. Usually, an optical fiber is used for guiding the light signals from the source to the detector.	
I. Extrinsic Optical	In the extrinsic mode, the incident wave is not directed through the bulk sample, but propagates along a wave guide and interacts with the sample at the surface within the evanescent field. Other surface methods of optical detection of biological recognition are based on modulation of the field excited at the interface between different materials due to incident light.	[11-14]
II. Intrinsic Optical	In the intrinsic mode, the incident light passes through the sample and interacts directly with the sample. Spectra analysis is used to detect target.	[7-10]

References:

[1] "Biosensor construction", *http://userpages.umbc.edu/~jshull1/ench772/construction.*

[2]. Vo-Dinh T, Griffin CD, and Sepaniak MJ, "Fiber Optic Chemical Sensors and Biosensors", *CRC Press*, pp. 217-257 (1991).

[3]. Polster J, Prestel G, Wollenweber M, Kraus G, and Gauglitz G, "Simultaneous Determination of Penicillin and Ampicillin by Spectral Fiber-Optical Enzyme Optodes and Multivariate Data Analysis based on transient signals obtained by flow injection analysis", *Talanta* 42, pp. 2065-2072 (1995).

[4]. Sawata S, Kai E, Ikebukuro K, Iida T, Honda T, and Karube I, "Application of peptide nucleic acid to the direct detection of deoxyribonucleic acid amplified by polymerase chain reaction", *Biosens Bioelectron* 14, pp. 397-404 (1999).

[5]. R. M. Pemberton, J. P. Hart, P. Stoddard, and J. A. Foulkes, "A comparison of 1-Naphthyl Phosphate and 4-Aminophenyl Phosphate as enzyme substrates for use with a screen-printed amperometric immunosensor for progesterone in cows' milk", *Biosens Bioelectron*, 14, pp.495-503 (1999).

[6]. K. Yano and I. Karube, "Molecularly imprinted polymers for biosensor applications", *Trac-Trend Anal Chem* 18, pp.199-204 (1999).

[7]. P.L. Gourley and A. E. McDonald, "Semiconductor microlasers with intracavity microfluidics for biomedical application", *Proc. SPIE* 2978, pp.186-196 (1997).

[8] P.L. Gourley, T.French, A. E. McDonald, E.A. Shields and M. F. Gourley, "Ultrasensitive detection of red blood cell lysing in a microfabricated semiconductor laser cavity", *Proc. SPIE* 2978, pp.195-206 (1998).

[9]. P. L. Gourley, *et al.*, "Detecting cancer quickly and accurately", *Proc. SPIE* 3912, pp.2-10 (2000).

[10]. P. L. Gourley, *et al.*, "Semiconductor microcavity laser spectroscopy of intracellular protein in human cancer cells", *Proc. SPIE* 4265, pp.113-124 (2001).

[11]. James O. Spiker and Kyung A. Kang, "Preliminary study of real-time fiber optic based protein C biosensor", *Biotechnology and Bioengineering* 66(3), pp.158-163 (1999).

[12]. Daniel P. Campbell, *et al.*, "Optical system-on-a-chip for chemical and biochemical sensing: the chemistry", *SPIE* 3540 (1999).

[13]. Nile F. Hartman, *et al.*, "Optical system-on-a-chip for chemical and biochemical sensing: the platform", *SPIE* 3537 (1999).

[14]. Daniel P. Campbell, *et al.*, "Integrated optic sensor for pH and ammonia", *SPIE* 3537 (1999).

APPENDIX B

DATA SHEETS FOR SANDIA EMC5978

Table B.1 MOVPE growth sheet for EMC5978 (Provided by Sandia National Labs [1])

Material	Al start	Al end	Å	n/p	c.c.	°C		Loops
GaAs			120.0	n	4.0E+18	750		
AlGaAs	0.05		197.7	n	4.0E+18	750		
AlGaAs	0.10		478.1	n	1.5E+18	750	Stop	1
AlGaAs	0.60		17.4	n	1.5E+18	750		1
AlGaAs	0.92	0.60	119.2	n	1.5E+18	750		1
AlGaAs	0.92		420.5	n	1.5E+18	750		1
AlGaAs	0.54	0.92	136.8	n	1.5E+18	750		1
AlGaAs	0.16		121.3	n	1.5E+18	750	Start	1
AlGaAs	0.16		485.1	n	1.5E+18	750	Stop	3
AlGaAs	0.60		17.4	n	1.5E+18	750		3
AlGaAs	0.92	0.60	119.2	n	1.5E+18	750		3
AlGaAs	0.92		420.5	n	1.5E+18	750		3
AlGaAs	0.54	0.92	136.8	n	1.5E+18	750		3
AlGaAs	0.16		121.3	n	1.5E+18	750	Start	3
AlGaAs	0.16		485.1	n	1.0E+18	750	Stop	1
AlGaAs	0.60		17.6	n	1.0E+18	750		1
AlGaAs	0.98	0.60	120.1	n	1.0E+18	750		1
AlGaAs	0.98		425.0	n	1.0E+18	750		1
AlGaAs	0.54	0.98	137.8	n	1.0E+18	750	Start	1
AlGaAs	0.40	0.54	232.4	uid		750		
AlGaAs	0.30	0.40	237.1	uid		750		
AlGaAs	0.20	0.30	247.8	uid		750		
AlGaAs	0.20		80.0	uid		750		
AlGaAs	0.20		80.0	uid		750	Stop	5
GaAs			80.0	uid		750	Start	5
AlGaAs	0.20		160.0	uid		750		
AlGaAs	0.30	0.20	247.8	uid		750		
AlGaAs	0.40	0.30	237.1	uid		750		
AlGaAs	0.54	0.40	232.4	uid		750		
AlGaAs	0.98	0.54	137.4	p	1.0E+18	750	Stop	1
AlGaAs	0.98		425.0	p	1.0E+18	750		1
AlGaAs	0.16	0.98	262.0	p	1.0E+18	750		1
AlGaAs	0.16		363.8	p	1.0E+18	750	Start	1
AlGaAs	0.92	0.16	261.4	p	1.0E+18	750	Stop	5
AlGaAs	0.92		420.5	p	1.0E+18	750		5
AlGaAs	0.16	0.92	261.4	p	2.0E+18	750		5
AlGaAs	0.16		363.8	p	1.0E+18	750	Start	5
AlGaAs	0.92	0.16	261.4	p	3.0E+18	750	Stop	30
AlGaAs	0.92		420.5	p	3.0E+18	750		30
AlGaAs	0.16	0.92	261.4	p	3.0E+18	750		30
AlGaAs	0.16		363.8	p	3.0E+18	750	Start	30
AlGaAs	0.06	0.16	994.0	p	3.0E+18	750		
GaAs			500.0	p	2.0E+19	600		
SUBSTRATE		3"	P+ GaAs			(100)2°>(110)		

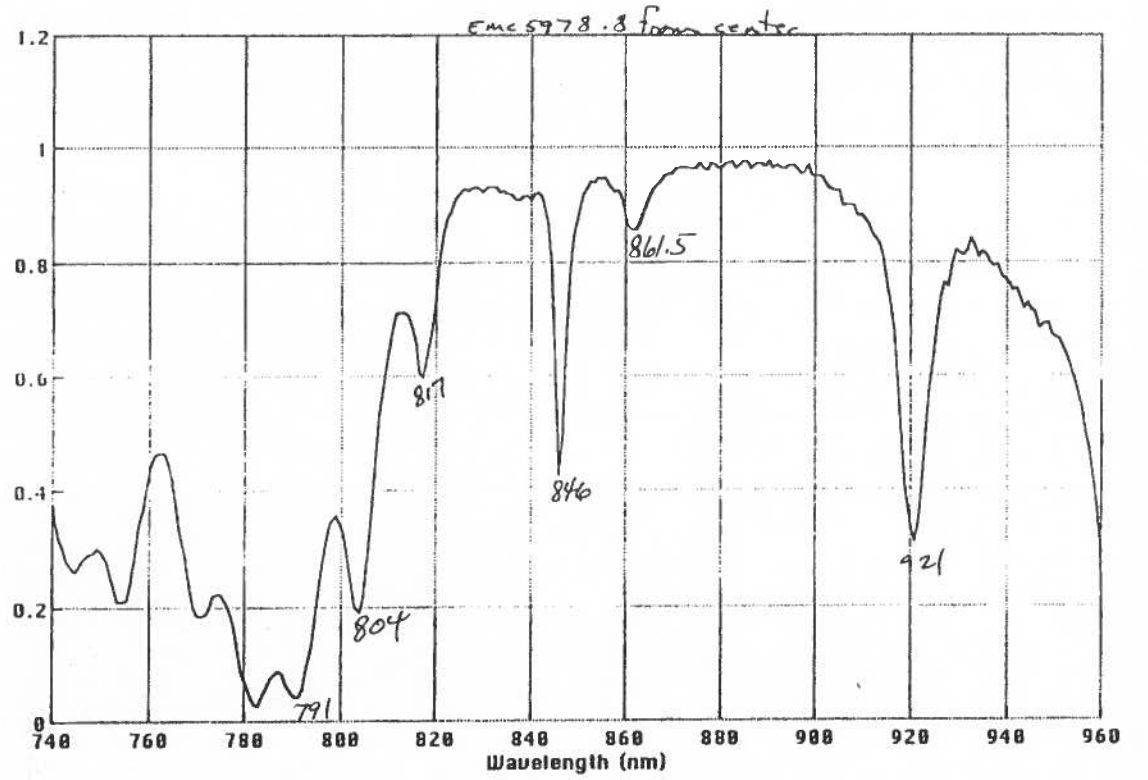

Figure B.1 Emission spectrum for EMC5978. (Provided by Sandia National Labs [1])

References:

[1]. Andy Allerman, Terry Hargett, and Rob Sieg, "EMC5978 MOVPE growth data sheet", *Sandia National Laboratories*, July, 2000.

APPENDIX C

SRIM/TRIM ION IMPLANT SIMULATIONS

As stated in reference [1], "SRIM is a group of programs which calculate the stopping and range of ions (up to 2 GeV/amu) into matter using a quantum mechanical treatment of ion-atom collisions (assuming a moving atom as an *"ion"*, and all target atoms as *"atoms"*). This calculation is made very efficient by the use of statistical algorithms which allow the ion to make jumps between calculated collisions and then averaging the collision results over the intervening gap. During the collisions, the ion and atom have a screened Coulomb collision, including exchange and correlation interactions between the overlapping electron shells. The ion has long range interactions creating electron excitations and plasmons within the target. These are described by including a description of the target's collective electronic structure and interatomic bond structure when the calculation is setup (tables of nominal values are supplied). The charge state of the ion within the target is described using the concept of effective charge, which includes a velocity dependent charge state and long range screening due to the collective electron sea of the target. TRIM (the Transport of Ions in Matter) is the most comprehensive program included. It will calculate both the final 3D distribution of the ions and also all kinetic phenomena associated with the ion's energy loss: target damage,

sputtering, ionization, and phonon production. All target atom cascades in the target are followed in detail. The programs are made so they can be interrupted at any time, and then resumed later. Plots of the calculation may be saved, and displayed when needed (it takes 5 seconds to begin viewing a saved calculation)."

SRIM/TRIM was used to simulate ion implantation into the half VCSEL wafer in our research. The simulation requires the following target parameters: composition, atom stoichiometric ratio, thickness and density for each target layer. The ion can be chosen from the ion data menu and corresponding implant energy and implant degree value are needed. In our case, the detailed target data are given in Table B.1. The density for each layer is calculated from the empirically formula

$$d(x) = 5.36 - 1.16x \quad (\mathrm{g/cm^3}), \qquad [C.1]$$

where x is the average Al atomic concentration for each layer.[2] The bandgap engineering techniques have been employed in the recent VCSELs in order to decrease the series voltage that develops across the mirrors due to the potential barriers at the numerous heterointerfaces. [3, 4] The grading of the alloy composition is not supported by the SRIM/TRIM simulator. Therefore, the average value of the Al atomic concentration was used.

Proton was used for implantation. The simulation results for the half VCSEL wafer with and without the n-ohmic contact layers are shown by Figure 3.4-3.6. The implant energy

of 56keV and 116keV are required, respectively. The results of the simulation were checked against the simulation of Dr. Feld [5] as shown in Figure C.1.

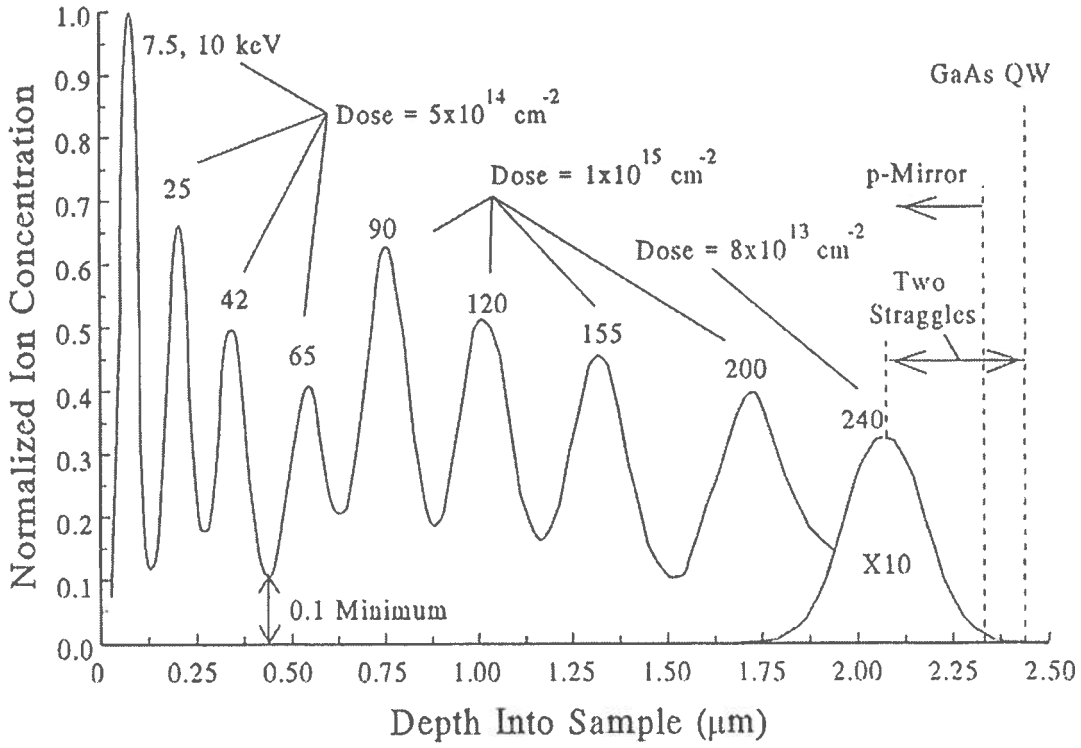

Figure C.1 Calculated ion concentration vs. depth for a typical proton implant schedule for both the active and isolation implants. (Copied from reference [5])

References:

[1]. "SRIM", *http://www.srim.org/SRIM/SRIMINTRO.htm*.

[2].S. Addachi, "GaAs, AlAs and $Al_xGa_{1-x}As$: material parameters for use in research and device application", *J. Appl. Phys.*, Vol. 58, No. 3, pp.R1-R29 (1985).

[3].R.S. Geels, S.W. Corzine, and L.A. Coldren, "InGaAs vertical-cavity surface-emitting lasers", *IEEE Journal of Quantum Electronics*, 27(6), pp.1359-1367 (1991).

[4].M.G. Peters, B.J. Thibeault, D. B. Young, J. W. Scott, F. H. Peters, A. C. Gossard, and L.A. Coldren, "Band-gap engineered digital alloy interfaces for lower resistance vertical-cavity surface-emitting lasers", *Applied Physics Letters*, 63(25), pp.170-171 (1993).

[5]. Stewart A. Feld, "Ph.D. Dissertation", *Colorado State University*, pp.166-171 (1996).

APPENDIX D

DETAILED PROCESSING RECIPES

The following is a summary of the processing recipes for fabrication of the electrically pumped VCSEL based intracavity fluidic biosensor. Details of the individual steps are covered in Chapter 4. Two different processing recipes are utilized for the half VCSEL fabrication. And the remained processing steps are same.

D.1 Process on the half VCSEL wafer

D.1.1 Recipe I

Bottom p-Ohimc Contact Formation

rinse			acetone, methanol and DI water
etch oxide	20 s		$NH_4OH:H_2O=1:10$
	20 s		$HF:H_2O=1:10$
rinse			DI water
evaporate	AuBe/Au	500 Å /2000 Å	Au:Be=99: 1 weight percent
anneal	45 s	440 ° C	

Alignment Mark Transfer Etching

soak & clean	5 min		acetone
rinse			acetone, methanol and DI water
pre-bake	2 min	120 ° C	
spin	30 s	5000 rpm	shipley PR 1818

soft-bake	2 min	95 ° C	
expose	5.5 s	15 mW/cm^2	UV light
develop	30 s		AZ400K:DI water=1:4
hard-bake	2 min	120 ° C	
etch	1 min	ultrasonic stirring	$HCl:H_2O_2:H_2O$=1:1:9
	1 min	w/o stirring	$HCl:H_2O_2:H_2O$=1:1:9
remove resist			acetone
rinse			DI water

Proton Implantation Mask Patterning

rinse			acetone, methanol and DI water
pre-bake	2 min	120 ° C	
spin	30 s	2000 rpm	AZ5214E
soft-bake	2 min	95 ° C	
expose edge-beads	1 min	15 mW/cm^2	UV light
develop edge-beads	as necessary (~1 min)		AZ400K:DI water = 1:3
rinse			DI water
soft-bake	1 min	95 ° C	
expose	8.5 s	15 mW/cm^2	UV light
soak	15 min		chlorobenzene
develop	50 s		AZ400K:DI water = 1:3
	40 s		AZ400K:DI water = 1:4
rinse			DI water
implant	proton	56 keV, 7 degrees off axis, 5x10^{14}/cm^2 dose	

Top n-Ohmic Contact Formation

soak	10 min		acetone
plasma asher	10 min		oxygen
rinse			acetone, methanol and DI water
pre-bake	2 min	120 ° C	
spin	30 s	5000 rpm	AZP4400
soft-bake	2 min	95 ° C	
expose edge-beads *	2 min	15 mW/cm^2	UV light
develop edge-beads*	as necessary (~30 s)		AZ400K:DI water = 1:4
rinse*			DI water
soft-bake*	1 min	95 ° C	
expose	30 s	15 mW/cm^2	UV light
develop	as necessary (~30 s)		AZ400K:DI water = 1:4
rinse			DI water
etch oxide	20 s		$HF:H_2O$=1:10

rinse			DI water
evaporate	AuGe/Ni/Au 500 Å /400 Å /1000 Å		Au:Ge=88:12 weight percent
lift-off	as necessary (~10min)		acetone air-brush & ultrasonic stirring
anneal*	45 s	380 °C	

D.1.2 Recipe II

Bottom p-Ohimc Contact Formation

rinse			acetone, methanol and DI water
oxide etch	20 s		$NH_4OH:H_2O$=1:10
	20 s		$HF:H_2O$=1:10
rinse			DI water
evaporate	AuBe/Au	500 Å /2000 Å	Au:Be=99: 1 weight percent
anneal	45 s	440 °C	

Top n-Ohmic Contact Formation & Alignment Mark Transfer

soak & clean	5 min		acetone
rinse			acetone, methanol and DI water
pre-bake	2 min	120 °C	
spin	30 s	5000 rpm	AZP4400
soft-bake	2 min	95 °C	
expose edge-beads *	2 min	15 mW/cm^2	UV light
develop edge-beads*	as necessary (~30 s)		AZ400K:DI water = 1:4
rinse*			DI water
soft-bake*	1 min	95 °C	
expose	30 s	15 mW/cm^2	UV light
develop	as necessary (~30 s)		AZ400K:DI water = 1:4
rinse			DI water
etch oxide	20 s		$HF:H_2O$=1:10
rinse			DI water
evaporate	AuGe/Ni/Au 500 Å /400 Å /1000 Å		Au:Ge=88:12 weight percent
lift-off	as necessary (~10min)		acetone air-brush & ultrasonic stirring
anneal*	45 s	380 °C	

Proton Implantation Mask Patterning

rinse			acetone, methanol and DI water
pre-bake	2 min	120 °C	
spin	30 s	4000 rpm	AZP4400
soft-bake	2 min	95 °C	

expose edge-beads *	2 min	15 mW/cm^2	UV light
develop edge-beads*	as necessary	(~30 s)	AZ400K:DI water = 1:4
rinse*			DI water
soft-bake*	1 min	95 ° C	
expose	30 s	15 mW/cm^2	UV light
develop	as necessary	(~30 s)	AZ400K:DI water = 1:4
rinse			DI water
implant	proton	95 keV, 7 degrees off axis, 1x10^{15}/cm^2 dose	

D.2 Dielectric Mirrors Deposition

deposit layers	10 pairs of Si_3N_4/SiO_2
cut mirrors	diamond scriber, ruler& cotton swab

D.3 Fluidic Cavity Formation

attach VCSEL	onto cover glass I	90 ° C	crystal bond
score sample			diamond scriber & ruler
rinse			acetone, methanol and DI water
pre-bake	2 min	120 ° C	
spin	30 s	4400 rpm	SJR5440
soft-bake	2 min	95 ° C	
expose edge-beads *	5 min	15 mW/cm^2	UV light
develop edge-beads*	as necessary	(~3 min)	developer 453
rinse*			DI water
soft-bake*	1 min	95 ° C	
expose	3 min	15 mW/cm^2	UV light
develop	as necessary	(~3 min)	developer 453
rinse			DI water
disattach VCSEL	away from cover glass I	90 ° C	crystal bond
break sample			cotton swab & diamond scriber
attach VCSEL	onto cover glass I	90 ° C	crystal bond
bond device	40 min	90 ° C	cylindrical magnet, iron chunk & microscope slide
disattach VCSEL	away from cover glass I	90 ° C	crystal bond

D.4 Biosensor System Assembly

attach device	onto cover glass I	90 ° C	crystal bond
decant resist			SJR5440, flow and surround the edges of the VCSEL
soft-bake	30 s	95 ° C	
spin	1 min	1000 rpm	SJR5440
gradually spin	as necessary	up to 8000 rpm	SJR5440
disattach device	away from cover glass I	90 ° C	crystal bond
cut and glue cover glass II			diamond scriber, rules & glass glue
mount device	onto the triple-layer cover glass II		silver epoxy
clean backside			acetone & cotton swab
glue tubes			nonconductive epoxy
attach tubes	onto the cover glass II		nonconductive epoxy
form epoxy reservoir			nonconductive epoxy, side capillary tubes & niddles
seal & connect	to the biosensor		nonconductive epoxy, side capillary tubes & niddles
assemble system	onto the microscope slide		glass glue

* These process step can be done if necessary.

Note: Some chemicals and metals used in the fabrication are dangerous, i.e., HF, photoresist, chlorobenzene and Be.

D.5 Process Flow For Recipe I

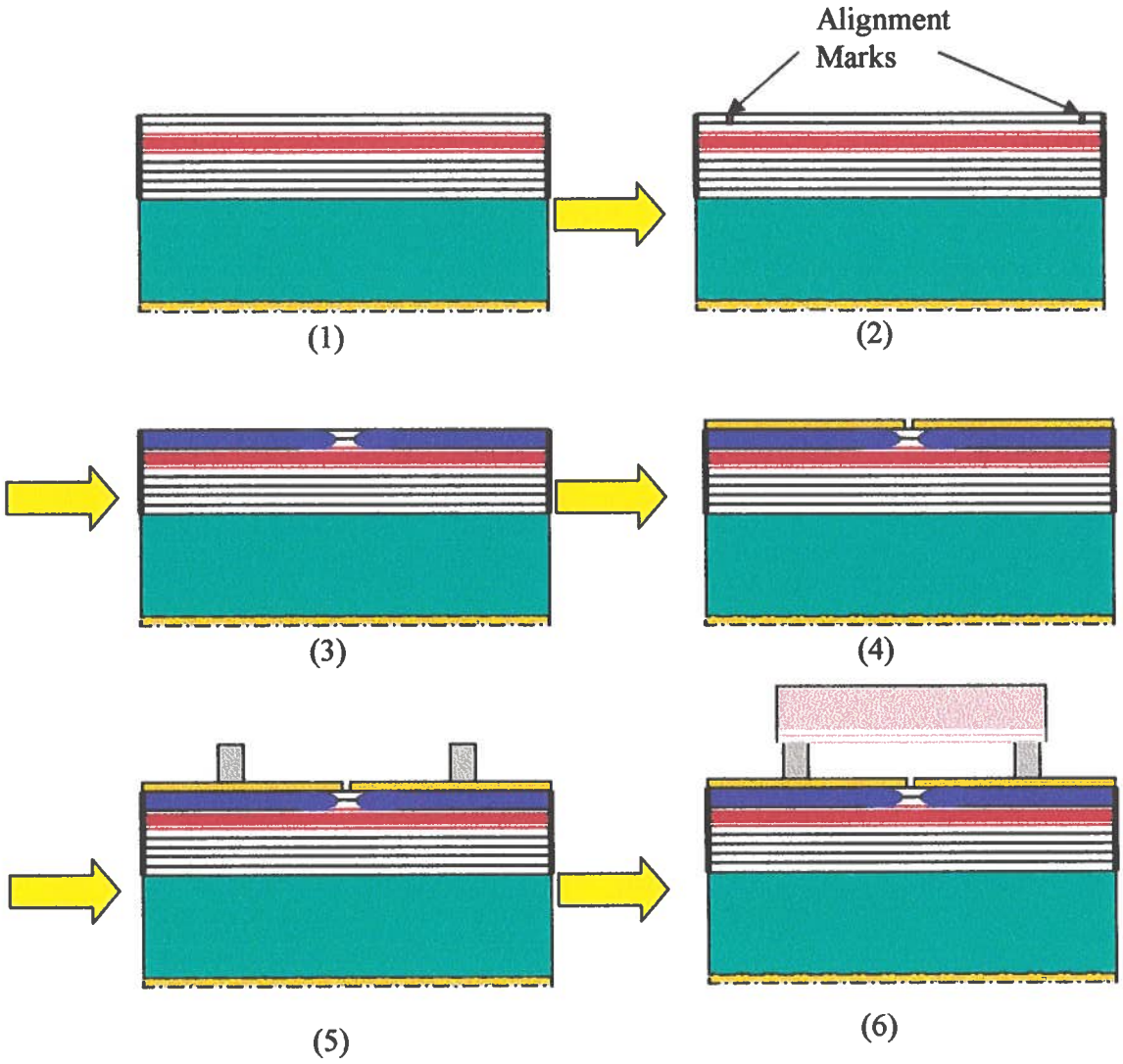

(1) Bottom p-Ohmic Contact Formation & Annealing
(2) Alignment Mark Transfer Etching
(3) Proton Implantation
(4) Top n-Ohmic Contact Formation
(5) Photoresist Spacer Formation
(6) Fluidic Cavity Bonding & Sealing
(7) Biosensor System Assembly

D.6 Process Flow For Recipe II

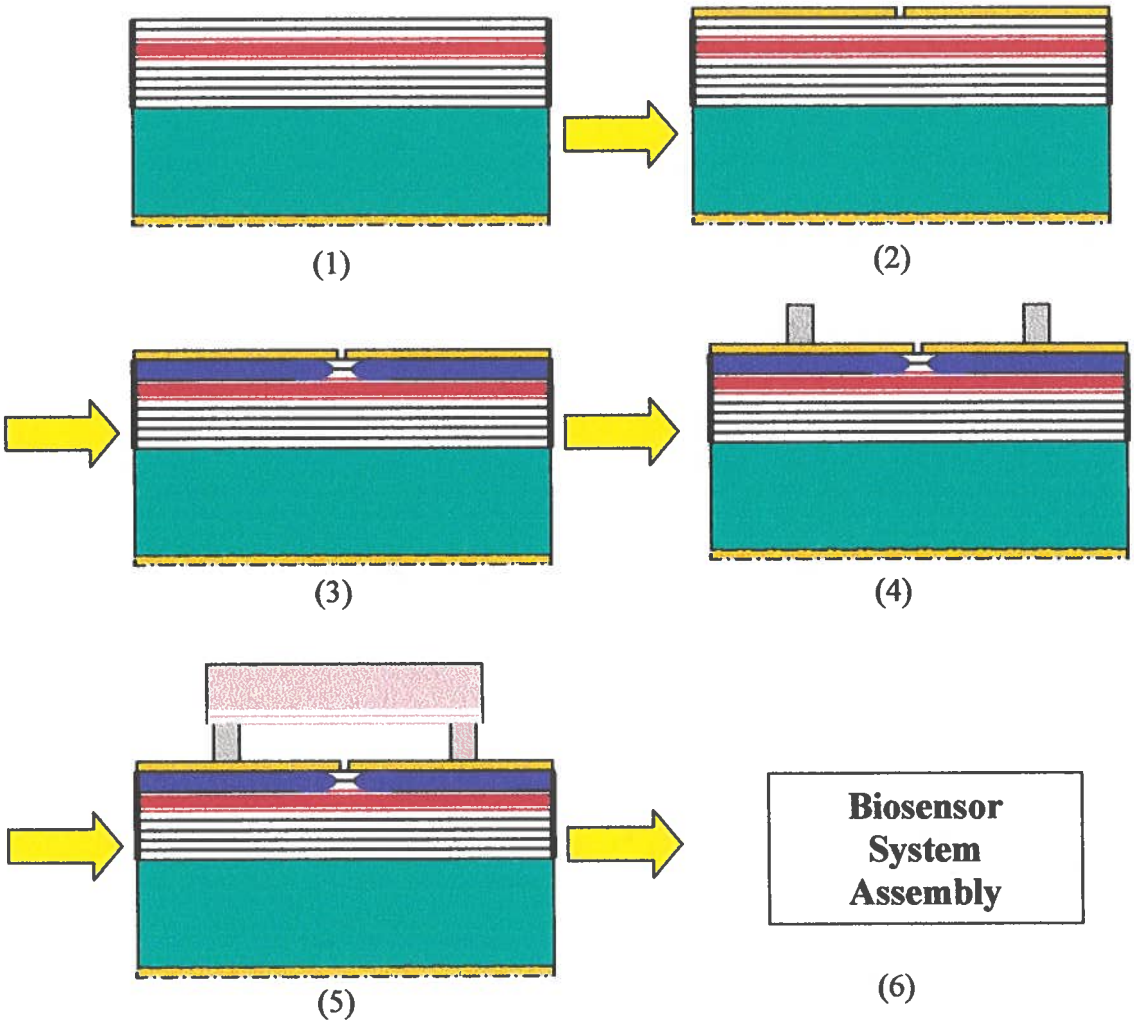

(1) Bottom p-Ohmic Contact Formation & Annealing
(2) Top n-Ohmic Contact Formation
(3) Proton Implantation
(4) Photoresist Spacer Formation
(5) Fluidic Cavity Bonding & Sealing
(6) Biosensor System Assembly